Bending and positioning of nanoparticles with light

Anastasia Babynina

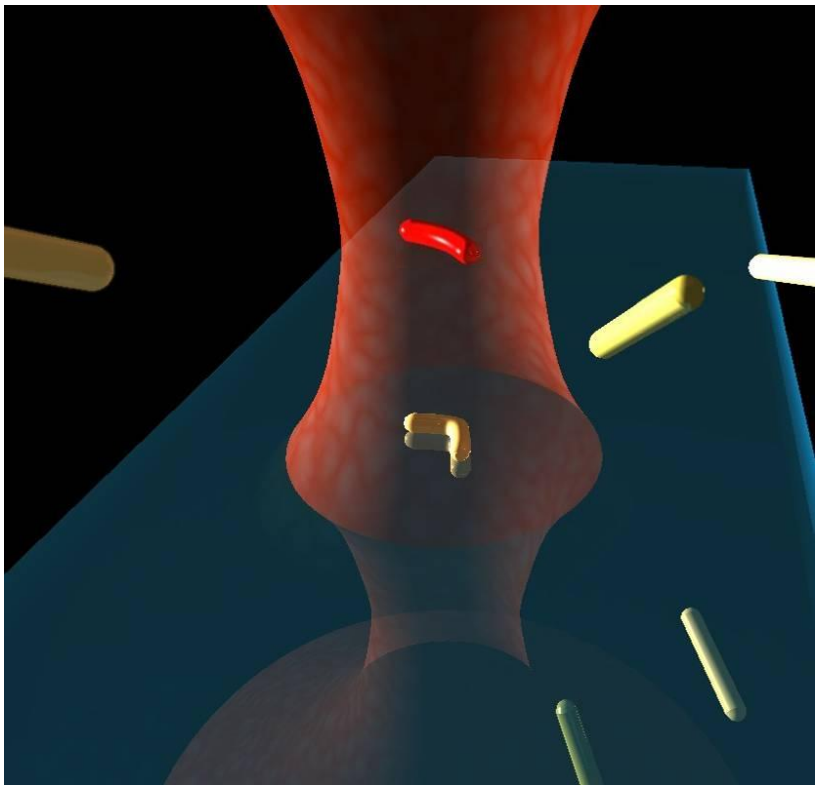

München

2017

Bending and positioning of nanoparticles with light

Anastasia Babynina

München, 2017

Bending and positioning of nanoparticles with light

Dissertation der Fakultät für Physik
der Ludwig-Maximilians-Universität München

vorgelegt von
Anastasia Babynina
aus Krasnokamensk, Russland (USSR)

München, 03.02.2017

Erstgutachter: Prof. Dr. Jochen Feldmann
Zweitgutachter: Dr. Bert Nickel
Datum der Abgabe: 03.02.2017
Datum der mündlichen Prüfung: 05.05.2017
The cover picture describes bending and printing of gold nanorods with a resonant laser. It was done by Dr. Michael Fedoruk.

For my mom, grandma, and grandpa, who has passed away.

Publications discussed in this work:

1) *"Bending gold nanorods with light"*
A. Babynina, M. Fedoruk, P. Kühler, A. Meledin, M. Döblinger, and T. Lohmüller
Nano Letters, Vol. 16, pp. 6485–6490, 2016

2) *"Near-field trapping of nano-sized objects with arrays of plasmonic nanoantenna"*
A. Babynina, P. Kühler, T. Lohmüller, and J. Feldmann
In preparation

3) *"Optothermal printing on gold nanorods"*
A. Graw, A. Babynina, S. Nedev, T. Lohmüller, and J. Feldmann
In preparation

Other publications:

1) *"Photoconductivity of nanocrystalline SnO_2 sensitized with colloidal CdSe quantum dots"*
R. B. Vasiliev, A. V. Babynina, O. A. Maslova, M. N. Rumyantseva, L. I. Ryabova, A. A. Dobrovolsky, K. A. Drozdov, D. R. Khokhlov, A. M. Abakumov, and A. M. Gaskov
Journal of Materials Chemistry C, Vol. 1, pp. 1005–1010, 2013

Contributions to conferences and workshops:

1) **SFB Workshop**, Hohenkammer, Germany, February 2013
Poster: *"Plasmonic sensing and manipulation of substrate supported bilayers with optical nanoantennas"*
A.Babynina, P. Kühler, T. Lohmüller

2) **Workshop on Photonics and Optoelectronics**, Riezlern, Austria, September 2014
Talk: *"Near-field trapping of nanoparticles on supported lipid membranes"*

3) **SFB Workshop**, Altötting, Germany, February 2015
Poster: *"Plasmonic sensing and manipulation of lipid membranes"*
Anastasia Babynina, Patrick Urban, Theobald Lohmüller

4) **DPG Conference**, Berlin, March 2015

Talk: *"Near-field trapping of nanoparticles on plasmonic nanoantenna arrays"*

Anastasia Babynina and Theobald Lohmüller

5) **Workshop on Photonics and Optoelectronics with New Materials**, Lenggries, July 2016

Talk: *"Bending gold nanorods with light"*

Content

Kurzfassung.

Die Wechselwirkung von Nanopartikeln mit Licht ist seit Jahrzehnten ein intensives Forschungsgebiet im Bereich der Nanowissenschaften. Dabei rücken insbesondere Methoden die es erlauben einzelne Nanopartikel mit Licht zu verändern und präzise zu positionieren immer mehr in den Fokus des wissenschaftlichen Interesses. Eine der größten Herausforderungen in diesem Zusammenhang ist es, neue und zuverlässige Wege zu finden, um einzelne Nanopartikel mit hoher Kontrolle zeitlich und räumlich exakt zu manipulieren. Zwei Beispiele, nämlich die Möglichkeit der kontrollierten Deformation einzelner Gold-Nanostäbchen mit Licht und die Verwendung plasmonischer Nanoantennenfelder für das optische Einfangen von Nanoobjekten mit hoher lateraler Präzession werden im Rahmen dieser Arbeit präsentiert.

Zunächst wurde untersucht, wie einzelne Gold-Nanostäbchen in Lösung mit Licht durch eine Kombination aus plasmonischem Heizen und der Wechselwirkung von optischen und hydrodynamischen Kräften in eine V-Form gebogen werden können. Dabei kann der Biegewinkel in Abhängigkeit der verwendeten Laserintensität kontrolliert werden. Derartige V-förmige Nanoantennen aus Gold haben ein großes Anwendungspotential bei der Herstellung von Metamaterialien. Die Möglichkeit einzelne, V-förmige Nanostäbchen mit Licht zu positionieren und auf einem Substrat zu orientieren ist eine Grundvorausetzung zur Verwirklichung derartiger Oberflächen und wurde in dieser Arbeit näher untersucht.

Im zweiten Teil dieser Arbeit wird die Eigenschaft von plasmonisch gekoppelten Nanoantennen, Licht in ein kleines Volumen zu bündeln ausgenutzt, um das optische Einfangen von Nanoobjekten auf plasmonischen Oberflächen zu ermöglichen. Mikro-nanostrukturierte Anordnungen von Gold-Nanodreiecken wurden durch eine Kombination aus kolloidaler Lithographie und Plasmabehandlung hergestellt. Die Anwendbarkeit dieser Nanoantennenstrukturen für das optische Einfangen von Siliziumdioxid-Partikeln wurde erforscht und die Abhängigkeit der Partikelgröße von der Nanoantennengeometrie genau untersucht. Als Erweiterung dieses Verfahrens wurde eine Kombination aus optischer Nah- und Fernfeldfalle angewendet, um einzelne Nanoobjekte wie Goldnanopartikel und Nanodiamanten präzise an einzelnen plasmonischen „Hot -Spots“ mit einer Genauigkeit von wenigen Nanometern exakt zu positionieren.

Abstract.

Exploiting the interaction of nanoparticles with light has been a vivid area of research in nanoscience for decades. Recently, the possibility of transforming and precisely positioning nano-objects with light has increasingly come into focus. One of the biggest challenges in this regard is finding new and robust ways of manipulating single nanoparticles with high spatio-temporal control. Two methods of addressing this demanding task - namely controlling the melting and shape transformations of individual gold nanorods, and the use of plasmonic nanoantenna arrays for the enhanced optical trapping of nano-sized objects - are the subject of this thesis.

First, individual gold nanorods in a solution can be bent into a V-shaped geometry upon laser irradiation through a combination of plasmonic heating, optical forces, and hydrodynamic interactions. The bending angle can be controlled within small margins by adjusting the laser intensity. Such V-shaped antennas hold great application potential for the design of metasurfaces if the precise alignment of individual antennas on a flat surface is achieved. To work toward this application, a method for optically printing and orienting bent nanorods on a surface with respect to the laser power density and polarization is presented.

Second, the ability of plasmonically coupled nanostructures or nanoantennas to concentrate light into a small volume is employed for the enhanced near-field trapping of nanosized objects at plasmonic interfaces. Micro-nanopatterned arrays of plasmonic nanoantennas were synthesized via plasma-enhanced colloidal lithography. The applicability of these nanoantenna arrays for the near-field trapping of silica beads with respect to the antenna geometry and the irradiation intensities was investigated. In an extension of this general approach, a combination of optical far-field and near-field trapping was used to actively deliver individual nano-objects, such as gold nanoparticles or nanodiamonds, precisely to individual plasmonic “hot spots” with the accuracy of a few nanometers.

1. Introduction.

Since ancient times, it has been known that the doping of ceramics, glass, or other composites with gold nanoparticles leads to changes in color. Some of the first known examples are the Lycurgus Cup, dating back to the fourth century in ancient Rome, and the windows in medieval churches, such as the rose window of the Notre-Dame de Paris cathedral (Figure 1.1). When light passes through the window, the particles scatter light at visible wavelengths, which causes the color.

a. b.

Figure 1.1. Gothic stained rose window of Notre-Dame de Paris. The color of the glass as it appears is due to colloidal gold nanoparticles. The photo of the front external view (a) is by Dietmar Rabich; the photo of the internal view (b) is by Krzysztof Mizera.

The nature of this phenomenon was unclear until the middle of the 19th century, when Michael Faraday established that the color originates from small sizes of colloidal particles [1]. In 1908, Gustav Mie provided a comprehensive mathematical explanation for how light interacts with small particles [2]. Twenty years later, Richard Zsigmondy earned the Nobel Prize for his work on colloids and his invention of the ultramicrosope [3]. Nowadays, a large range of well-developed methods exist for synthesizing gold nanoparticles with arbitrary sizes, morphologies, and optical properties [4,5,6,7].

Gold nanoparticles are intensively used in different nanotechnology fields [8,9,10,11,12]. Localized surface plasmon resonance, electromagnetic field enhancement, optical forces, and the possibility of plasmonic heating open up a broad range of applications, such as near-field

trapping [13], the sensing and detecting of single molecules [14,15], drug delivery [16], and photothermal and photoacoustic imagining [17].

This thesis shows how gold nanorods can be bent with a continuous wavelength (CW) laser at a wavelength matching plasmon resonance. The dependence of the bending angle on the laser power density is presented. The origin of the bending phenomenon is explained by taking into account optical properties as well as heating and hydrodynamic effects. Next, the possibility of the positioning of V-shaped antennas on a surface in accordance with laser polarization is investigated. This approach holds promising potential for future application in the area of metamaterials.

Moreover, in this work, the near-field trapping of small, low-refractive index objects on plasmonic nanoantennas has been investigated. The dependence of laser power densities on gap sizes and on silica bead size is shown. The new concept of the direct delivery of an object into “hot spots” on plasmonic nanoantennas by means of conventional optical tweezers is introduced. Thermoplasmonic effects on plasmonic nanoantennas are also addressed.

The thesis is organized as follows: After the introduction, fundamental physical concepts are introduced in the second chapter. Specifically, the unique optical properties of metal nanoparticles, electromagnetic field enhancement, plasmonic heating, and the optical forces exerted on plasmonic nanoparticles are discussed.

In the third chapter, the experimental techniques used in this work are explained. A description of optical techniques and techniques used for structural analysis is given as well. Second, the computational methods used for calculating optical forces, temperature, electromagnetic field enhancement, absorption, scattering cross sections, and hydrodynamics interactions are introduced.

The fourth chapter focuses on the investigation of bending gold nanorods with resonant laser illumination. The dependence of the bending angle on printing laser power densities is presented. The changes of the optical properties and of the crystal structure that take place upon irradiation with the laser beam are discussed. Furthermore, the positioning of V-shaped antennas and their orientation with respect to laser polarization on a surface have been studied.

The fifth chapter describes the synthesis of large arrays of plasmonic nanoantennas with desired optical properties by using bottom-up lithography. Plasmonic nanoantennas are a promising platform for establishing the near-field trapping of low-refractive index nanoparticles

in an ensemble. The direct delivery of nano-objects into individual gaps of plasmonic nanoantennas is shown.

The sixth chapter concludes the thesis, summarizes the findings of this work, and provides an outlook for possible future investigations.

2. Fundamentals.

2.1. Plasmonic nanoparticles and nanoantennas.

This chapter covers the origins of the optical properties of gold nanoparticles. The interaction of gold nanoparticles and external light is discussed. Furthermore, the interactions between two gold nanoparticles placed close to each other, as well as near-field enhancement at their surfaces will be explained. The plasmonic heating of gold nanostructures and the optical forces acting on gold nano-objects will be discussed.

2.1.1. The dielectric function of gold.

In a classic approach, an interaction between an electromagnetic field resulting from incident light and an irradiated structure explains the optical properties of gold nanoparticles. The dielectric function is discussed in terms of a basic theoretical approximation for free electrons, namely the Drude-Sommerfeld model [18,19]. In the ultraviolet-visible (UV-Vis) wavelength range, the electrons in a metal are considered free electron gas oscillating around positive nuclei. By considering one electron in electron gas and including the specific properties of certain metals in an effective electron mass, one can write the equation of motion as in Maier S.A. [18]:

$$m\ddot{x}(t) + m\Gamma\dot{x}(t) = -eE(t), \qquad \textbf{2.1}$$

where m is the mass of the electron, $E(t)$ is the external electric field, and Γ is the damping constant, which describes the collision of free electron gas with characteristic time τ due to the interactions of the oscillating electrons with lattice vibrations (electron-phonon scattering). At room temperature, typical means of relaxation time τ is in the range of 100THz. Taking into account that the electric field resulting from incident light has a harmonic time dependence, the expression for the electric field can be written as follows: $E(t) = E_0 e^{-i\omega t}$, where E_0 is the amplitude of the electric field, and ω is the frequency. Then, the solution of equation 2.1 illustrates the displacement of an electron exposed to a harmonic electric field as follows:

$$x(t) = \frac{e}{m(\omega^2 + i\Gamma\omega)} E_0 e^{-i\omega t}. \qquad \textbf{2.2}$$

Due to the displacement of electrons, one can observe the macroscopic polarization P = -*nex*, where *n* is an electron density, and *e* is a charge that is displaced from its position in *x*.

Using the equation for electric displacement field *D*, with external electric field *E*, and inserting macroscopic polarization *P*, one gets the following equation [20]:

$$D = \varepsilon_0 E(t) + P = \varepsilon\varepsilon_0 E(t), \qquad \textbf{2.3}$$

where ε_0 is the vacuum permittivity, and ε is the dielectric function of material. Meanwhile, ε is the frequency dependent dielectric function $\varepsilon_{drude}(\omega)$, which is determined based on the free electron gas in a metallic structure. Taking into account this assumption, one gets the following equations:

$$P = -\frac{ne^2}{m_e(\omega^2 + i\Gamma\omega)}E(t) \qquad \textbf{2.4}$$

$$D = \varepsilon_0\left(1 - \frac{ne^2}{m_e(\omega^2 + i\Gamma\omega)}\right)E(t) \qquad \textbf{2.5}$$

and therefore derives:

$$\varepsilon_{Drude}(\omega) = 1 - \frac{ne^2}{\varepsilon_0 m_e(\omega^2 + i\Gamma\omega)} = 1 - \frac{\omega_P^2}{\omega^2 + i\Gamma\omega}. \qquad \textbf{2.6}$$

In the last step, the substitution of $\omega_P^2 = \frac{ne^2}{\varepsilon_0 m_e}$ is used. Frequency ω_P is the plasma frequency of free electron gas [18]. The dependence of the dielectric function on the plasma frequency of free electron gas contains important information about the optical properties of certain metals under electromagnetic fields. The real part of the dielectric function of a metal changes the sight from positive to negative for frequencies below the plasma frequency, which leads to a change in the behavior of the metal. For instance, at ultraviolet frequencies that are much higher than the plasma frequency, metals acquire a dielectric character, and electromagnetic waves propagate through it. At frequencies lower than the plasma frequency, electromagnetic waves do not penetrate the metal. In this case, metals mainly absorb or reflect electromagnetic waves [18].

In the case of noble metals, such as silver and gold, one should take into account two factors. First, a strong interaction of the free electron gas with the positively charged ion core of the metal has to be considered [18]. Second, interband transitions that can happen in a noble metal - for instance, in gold at a wavelength below 700 nm - have to be taken into account. The energy of incident photons is sufficiently enough to induce interband transitions. Under interband transitions, one should understand the excitation of electrons from the low-energetic d-band to the higher-energetic s- or p-band. The first condition can be corrected by introducing background permittivity ε_∞ in equation 2.5. The second one can be amended by implementing in

equation 2.1 additional term ω_0, which corresponds to bound electrons with resonance frequency ω_0

$$m_e\ddot{x}(t) + m_e\Gamma\dot{x}(t) + m_e\omega_0^2 x(t) = -eE(t). \qquad \textbf{2.7}$$

In the case of gold for wavelengths shorter than 700 nm, the experimental data by Johnson and Christy has been used [21]. For exciting wavelengths above 700 nm, the analytical equations of the Drude-Sommerfeld theory can be applied for calculations [22].

2.1.2. Localized surface plasmon resonance in gold nanoparticles.

In the previous chapter, surface plasmons that propagate at the interface between a dielectric medium and a conductor were discussed. Regarding the conductor, a metal with infinite dimensions was considered. However, when the dimensions of a metal structure are confined and are smaller than the wavelength of an incident light, then the oscillations of the electrons are confined to a small volume and cannot propagate. Compared with an infinite boundary metal-insulator transition, in metallic nanoparticles, electromagnetic waves displace all free conduction electrons relative to the ions in the crystal lattice of the particle (Figure 2.1). As a result, the surface positive and negative charges are concentrated in different parts of the nanostructure. This leads to the emergence of an internal restoring electric field. The fields' values are proportional to the displacement of the electrons with respect to the ionic lattice. This system represents an oscillator, whose properties are determined based on the effective mass, the density of electrons in the metal particles, and the geometry. These non-propagating oscillations are called localized surface plasmons. Due to the small dimensions, the phase of the harmonic oscillations of the electrons remains almost constant over the particle size. Localized surface plasmons can take place in various plasmonic nanoparticles, e.g., gold [23], silver [24], and

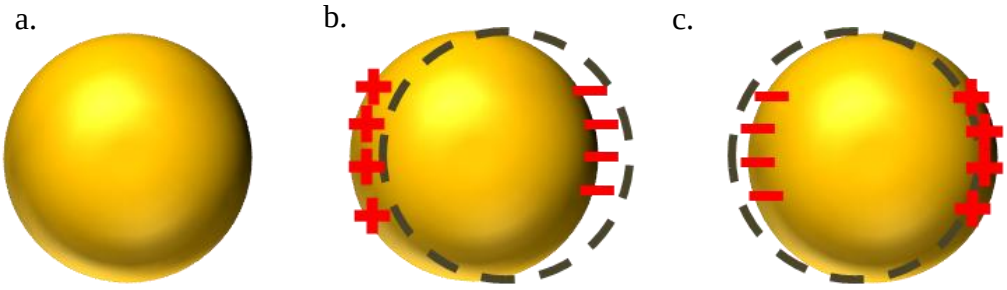

Figure 2.1. Illustrations of the behavior of a gold nanoparticle without (a) an electromagnetic field and excited by an external electromagnetic field (b and c). In figures (b) and (c), the charge displacement under incident electromagnetic waves is schematically illustrated.

copper nanoparticles [25,26] with different shapes; the resonance wavelengths are typically in the visible region [18].

To foster a better understanding of the interaction of a metal nanoparticle with electromagnetic waves, the quasi-static approximation was used, where a particle of radius $a<<\lambda$ is placed in isotropic surrounding media with dielectric constant ε_m under a static incident electric field with amplitude E_0. Here, the main condition of the quasi-static approximation can be defined. In the case of $a<<\lambda$, the phase of the harmonically oscillating electromagnetic field over the nanoparticle volume remains constant [18,19]. The dielectric constant of the dielectric surrounding medium is connected to a refractive index via $\varepsilon_m = n^2$, where n is a refractive index [20]. Using Laplace's equation, $\nabla^2\Phi = 0$, and cylindrical coordinates, one can solve the equation for the electromagnetic field, $E = -\nabla\Phi$:

$$\Phi_{int} = -\frac{3\varepsilon_m}{\varepsilon + 2\varepsilon_m} E_0 r\cos\theta \qquad \textbf{2.8}$$

$$\Phi_{out} = -E_0 r\cos\theta + \frac{\varepsilon - \varepsilon_m}{\varepsilon + 2\varepsilon_m} E_0 a^3 \frac{\cos\theta}{r^2}, \qquad \textbf{2.9}$$

where Φ_{out} is a superposition of the potentials associated with the external field and with the field of dipole in the sphere. By combining the equation of the dipole moment $\Phi_{dipol}(r) = \frac{pr}{4\pi\varepsilon_0\varepsilon_m r^3}$ and equation 2.9, one obtains an equation describing the dipole moment in the center of a sphere:

$$\Phi_{out} = -E_0 r\cos\theta + \frac{p * r}{4\pi\varepsilon_0\varepsilon_m r^3} \qquad \textbf{2.10}$$

$$p = 4\pi\varepsilon_0\varepsilon_m a^3 \frac{\varepsilon - \varepsilon_m}{\varepsilon + 2\varepsilon_m} E_0. \qquad \textbf{2.11}$$

Hence, the external field polarizes a sphere and creates a dipole moment in a sphere. Taking into account that $p = \varepsilon_0\varepsilon_m\alpha\frac{\varepsilon-\varepsilon_m}{\varepsilon+2\varepsilon_m}$, the Clausius-Mossotti equation can be derived:

$$\alpha = 4\pi a^3 \frac{\varepsilon - \varepsilon_m}{\varepsilon + 2\varepsilon_m}. \qquad \textbf{2.12}$$

As one can see, polarizability α reaches its maximum value under the condition of $|\varepsilon + 2\varepsilon_m| \to 0$ [18], which corresponds to resonant behavior. The dielectric function of gold has a frequency-dependent character: $\varepsilon(\omega) = Re[\varepsilon(\omega)] + Im[\varepsilon(\omega)]$. The imaginary part has much smaller values compared to the real part. By neglecting the small impact of the imaginary part, a resonant condition can be deduced as $Re[\varepsilon(\omega)] = -2\varepsilon_{m.}$. This equation is called the Fröhlich condition. The approach described above is called the quasi-static approach, which reveals major

parameters influencing surface plasmon resonance, including particle shape, the dielectric function of metal, and the surrounding environment.

Different damping or decaying mechanisms of surface plasmon resonances, such as radiation damping [27], energetic relaxation [28], and pure dephasing [28], exist. Radiation damping is the scattering process of surface plasmon resonance resulting in a re-radiation of a new electromagnetic wave. Energetic relaxation can be understood as an internal loss mechanism. Under an electromagnetic radiation charge, displacement in gold nanoparticles takes place, and therefore, electron-hole pairs form. Electron-hole pairs have usual decay channels via electron-electron scattering, electron-phonon scattering, etc. During a pure dephasing loss mechanism, oscillating plasmons lose their phase relation with the external electromagnetic field [28].

Effective cross section of gold nanoparticles.

The quasi-static approximation for local surface plasmons in gold nanoparticles under an electromagnetic irradiation has been discussed above. Equation 2.12 connects polarizability α with the scattering and absorption properties of gold nanostructures. The optical properties of gold nanostructures are characterized by effective scattering (C_{sca}), absorption (C_{abs}) cross sections, and the extinction (C_{ext}) cross section. The latter one is the sum of the scattering and absorption cross sections. Cross sections are the effective areas of gold nanoparticles with which nanoparticles absorb or scatter light; thus, cross sections have units of area and can be expressed through dipole polarizability α[29]:

$$C_{abs} = k * Im(\alpha) \quad \textbf{2.13}$$

$$C_{scat} = \frac{k^4}{6\pi}|\alpha^2| \quad \textbf{2.14}$$

$$C_{ext} = C_{abs} + C_{scat}, \quad \textbf{2.15}$$

where $k = {}^{2\pi}/_{\lambda}$ is a wave number. The complex polarizability of the particle, α, is proportional to the particle volume (equation 2.12) within the quasi-static approximation. Under resonance conditions, the absorption and scattering cross sections of the nanoparticles exceed the real geometrical parameters of nanoparticles and reach their maximum values at the resonance frequency. The enlargement in the absorption and scattering cross sections of nanoparticles at the resonance frequency allows one to consider the nanoparticles as optical nanoantennas. The resonance frequency depends not only on the particle's size but also on the refractive index of

the surrounding medium. In other words, an increase of the refractive index of the surrounding medium leads to a red shift of the resonance frequency and therefore leads to a red shift of the plasmonic peak. Scattering processes depend on the squared polarizability and therefore on the square of the particle volume. Meanwhile, the absorption part depends linearly on the particle volume. The given dependences show that damping processes strongly depend on the particle size. One can expect that for small plasmonic particles, absorption dominates as the damping process, and scattering dominates for larger particles [19].

The quasi-static approach provides adequate results for spherical particles each with a diameter of less than 50 nm. However, for larger particles, the retardation effects have to be considered, and therefore, for larger spherical nanoparticles, the model has to be expanded with Mie theory [23].

Nevertheless, in this work, gold nanostructures with complex shapes are of interest, and instead of the quasi-static approach and the Mie theory, the finite-difference time-domain method (FDTD method) was applied to calculate the absorption and scattering cross sections. In Chapter 3, the method mentioned above will be discussed.

2.1.3. Near-field enhancement.

As discussed in the previous section, plasmonic nanoparticles work as optical nanoantennas and are capable of enhancing and confining incident far-field light in the nanometer space. An enhanced electromagnetic field in the vicinity of a metallic surface can be used in different applications, e.g., molecular fluorescence [30], molecular sensing [31], near-field microscopy [32], and surface-enhanced Raman spectroscopy (SERS) [33]. Here, plasmonic nanoparticles with different shapes, electromagnetic field enhancement at the surfaces of plasmonic nanoparticles, and the hybridization of plasmons between two coupled plasmonic nanoparticles will be discussed.

Near-field enhancement in single plasmonic nanoparticles.

The main limitation of far-field optical forces is the diffraction limit: The light of certain wavelength λ can be focused to a spot with a size of $\lambda/2n$ in a medium with refractive index n [34]. Nowadays, the diffraction limit problem can be solved by using near-field techniques based on the idea of concentrating light into the vicinity of plasmonic nanoantennas.

The simplest example of a plasmonic nanoantenna, which converts electromagnetic radiation from far-field optical forces into near-field optical forces, is a metallic nanoparticle. Examples are gold nanoparticles or gold nanorods. [35]. The Clausius-Mossotti equation in the quasi-static approximation for the polarizability of a spherical nanoparticle in an electric field can be written as follows:

$$\alpha = 4\pi a^3 \frac{\varepsilon - \varepsilon_m}{\varepsilon + 2\varepsilon_m}. \qquad \textbf{2.16}$$

In section 2.1.2, the conditions required for observing plasmon resonance (the Fröhlich condition) were already discussed. In resonance conditions, polarizability $\boldsymbol{\alpha}$ is limited by the incomplete vanishing of its denominator, as $\boldsymbol{Im}[\boldsymbol{\varepsilon}(\boldsymbol{\omega})] \neq \mathbf{0}$. *E*lectric field $\boldsymbol{E}$ can be evaluated from the potentials as follows [18]:

$$E_{in} = \frac{3\varepsilon_m}{\varepsilon + 2\varepsilon_m} E_{0.} \qquad \textbf{2.17}$$

$$E_{out} = E_0 + \frac{3n(n \cdot p) - p}{4\pi\varepsilon_0\varepsilon_m} \frac{1}{r^3}, \qquad \textbf{2.18}$$

where $n = \boldsymbol{r}/r$. The resonance conditions of α also lead to the enhancement of the internal and external dipole fields. The dependence of the electric field enhancement on a factor of $1/r^3$ shows that the enhancement of the electric field takes place in the vicinity of the particle surface.

The near-field distribution around a gold nanoparticle is shown in Figure 2.2. The XY projection of the electromagnetic field enhancement in the vicinity of a gold nanoparticle with a diameter of 60 nm illuminated by light is shown. The linear polarized incident light is oriented vertically.

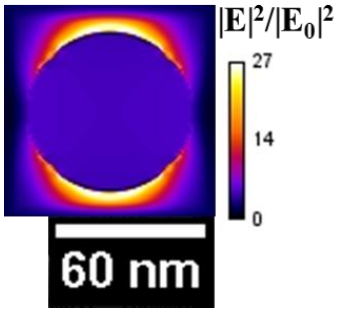

Figure 2.2. FDTD simulations of electromagnetic field enhancement at the surface of a gold nanoparticle. XY projection of calculated intensities. Simulations were performed for wavelength λ = 535 nm, assuming that glass was the substrate. The nanoparticle diameter was 60 nm. The colored scale bar represents the enhancement factor of the electric field compared with the incident field.

For spherical nanoparticles, the resonance frequencies are determined based on the maximum of polarizability α, which is of a monotonic nature. However, for complex shapes, polarizability α has an anisotropic character. Considering the case of an ellipsoidal particle -

particularly, a nanorod with asymmetry on the z axis - polarizability α has a different character along different axes and can be written as follows:

$$\alpha_{x,y,z} = \frac{4}{3}\pi L_x L_y L_z \frac{\varepsilon - \varepsilon_m}{\varepsilon_m + P_{x,y,z}(\varepsilon - \varepsilon_m)}, \qquad \textbf{2.19}$$

where L_x, L_y, and L_z are each half of the lengths of the ellipsoid along the x, y, and z axes; ε is the dielectric function of the material; ε_m is the dielectric function of the surrounding medium; and $P_{x,y,z}$ represents the depolarization factors along the x, y, and z axes [35]. If one assumes that the ellipsoid has equal lengths in two directions (for instance, L_x=L_y), one can expect two localized surface plasmon resonances: transverse and longitudinal. The longitudinal mode is more pronounced compared with the transverse mode. Therefore, stronger local electromagnetic field enhancement is expected when the longitudinal plasmons are excited.

In Figure 2.3, near-field enhancement for a gold nanorod with a length of 124 nm and a diameter of 21 nm with a polarization oriented parallel to the longer axis of the nanorod is presented. In the case of spherical gold nanoparticles, if the near-field enhancement factor reaches values of several dozens, then for a gold nanorod that possesses asymmetry and sharp edges, the electromagnetic field enhancement factor reaches values of a few thousands.

Figure 2.3. FDTD simulations of electric field enhancement at the surface of a gold nanorod. XY projection of calculated intensity. Simulations were performed for wavelength λ = 1064 nm, assuming that glass was the substrate. A gold nanorod with a 124-nm length and a 21-nm width is illuminated by light with linear polarization parallel to the longer axis of the gold nanorod. The colored scale bar represents the enhancement factor of the electric field relative to the incident field. The strongest enhancement is observed at the tips of the gold nanorod.

Several effects determine the factor of electromagnetic field enhancement in the vicinity of the plasmonic nanoparticles: elongation, curvature of the plasmonic structure, and asymmetry. In plasmonic nanostructures with shape asymmetry, e.g., silver nanocubes [36], gold nanocubes [37], gold nanostars [38], gold nanotriangles [39], and gold nanoprisms [40], at the sharp tips, greater electromagnetic field enhancement was observed.

Near-field enhancement in plasmonically coupled nanostructures.

Gold nanoparticle dimers with controlled gaps were successfully applied for SERS measurements, in which the signal was enhanced up to seven orders of magnitude [41]. Higher electromagnetic field enhancement could be achieved in plasmonically coupled nanoparticles compared with single nanoparticles [42]. It was also experimentally demonstrated that controlling the polarization of incident light is highly important for obtaining the maximal values of the enhancement factor [43]. Moreover, the possibility of controlling optical properties over a large range of wavelengths by varying the sizes of the nano-objects or by varying the distance between the nano-objects makes coupled nanostructures very attractive for a wide range of applications.

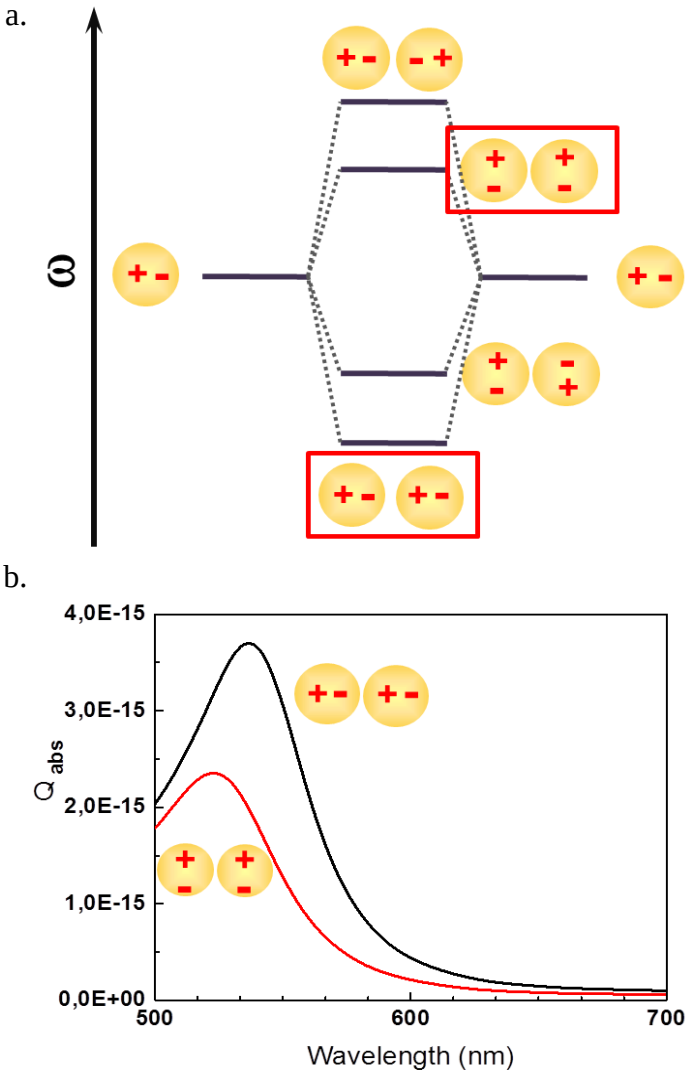

Figure 2.4. Plasmon hybridization between two interacting particles placed close to each other. Two optically excited modes can be distinguished (a). Absorption spectra of optically coupled gold (60 nm in diameter). Depending on the polarization of the incident light, one can selectively excite one of two modes (b) [40].

First, the hybridization of the plasmons of two individual nanostructures placed close to each other will be discussed. In such a system, the localized plasmon modes of the individual nanostructures couple due to Coulomb interactions, and the coupled system will possess the plasmon modes that differ from those of individual nanostructures. The overlapping of

individual plasmon modes gives rise to a new hybridized system with “bonding” and “antibonding” modes [44]. The hybridization of plasmon eigenmodes of individual nanostructures in principle is similar to the molecular orbital theory [40]. The most common and simple example of such plasmonically coupled structures is a system of two gold nanoparticles placed close to each other. In Figure 2.4a, plasmon hybridization between two gold nanoparticles is illustrated. The dipolar modes of individual nanoparticles undergo hybridization in the dimer, which leads to the formation of four new plasmon modes: two of them possess dipoles parallel to the dimer, and two of them have dipoles oriented perpendicularly to the dimer. However, light excites the plasmon modes only if the dipole moments of two particles are not mutually exclusive (marked with red boxes) [45]. The plasmon orbital with the parallel orientation of dipoles to the longest axis of the dimer - and therefore the orbital with less energy - gives rise to the longitudinal mode (or the bonding mode). Meanwhile, the plasmon mode with the perpendicular orientation of dipoles to the longest axis of the dimer leads to a higher energetic transverse mode (the anti-bonding mode) [40]. The eigenmode hybridization of two gold nanoparticles placed close to each other is shown in Figure 2.4a. Coupling between two plasmonic nanostructures over a narrow gap leads to highly localized and strongly enhanced electromagnetic fields in the gap.

The absorption spectra of two gold nanoparticles each with a diameter of 60 nm and with a distance of 10 nm between them are shown in Figure 2.4b. As one can see from the absorption spectra, the transverse mode (with the perpendicular orientation of dipoles to the longest axis of the dimer) is shifted to the blue region compared with the longitudinal mode (with the parallel orientation of dipoles to the longest axis of the dimer).

The plasmon hybridization depends on the distance (D) between the two nanoparticles. The interaction energy between classical dipoles has a $1/D^3$ dependence, therefore, a stronger interaction between individual plasmonic nanoparticles can be achieved by reducing distance D between them [44]. In Figure 2.5, the dependences of the resonance wavelengths of two coupled gold nanoparticles with an incident light polarization perpendicular (a) and parallel (b) to the longest axis of the dimer on the distance between the plasmonic gold nanoparticles are shown. Notably, for the incident light with the polarization perpendicular to the longest axis of the dimer, the position of the plasmon peak does not shift for a reduction of the distance between the nanoparticles. The orthogonal orientation of the dipoles is repulsive; therefore, with a decrease in the distance between the dipoles, the plasmon frequencies increase [46]. However, the decrease

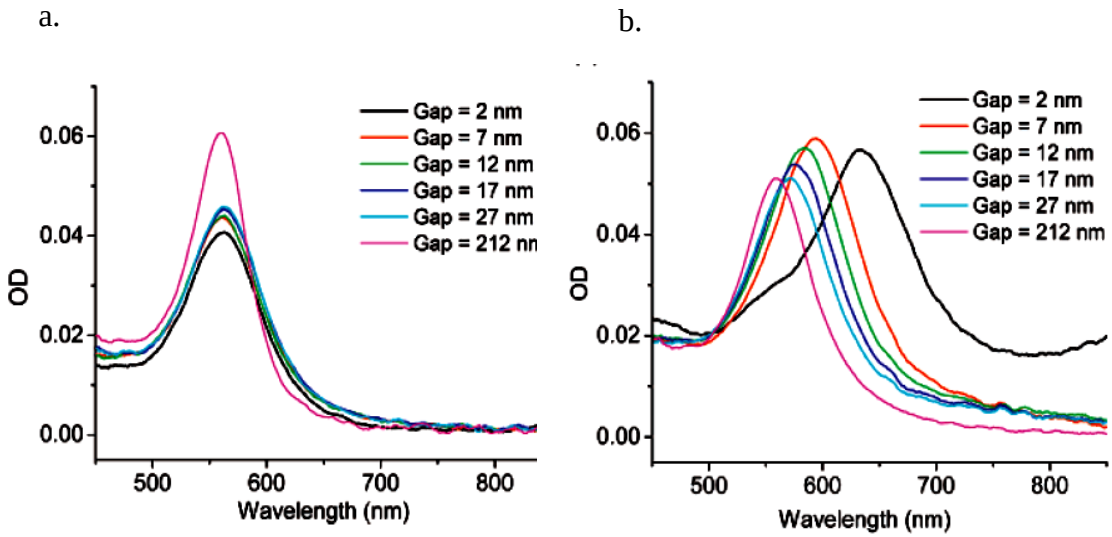

Figure 2.5. Optical properties of gold nanoparticle dimer under different orientation of light polarization vs. the distance between nanoparticles. Micro-absorption spectra of gold nanoparticle dimers for incident light with a polarization parallel (a) and perpendicular (b) to the longest axis of the dimer with different distances between nanoparticles. Reprinted with permission from [46]. Copyright (2007) American Chemical Society.

in the distance between the two nanoparticles under a parallel orientation of the polarization of incident light strongly shifts the plasmonic peak of the coupled nanoparticles to the red region of the spectrum (Figure 2.5b). For a parallel orientation of the light polarization the dipoles are attractive, which results in a decrease of the plasmon frequency and therefore a red shift of the longitudinal mode is observed [46].

Section 2.1.3 provides equation 2.18 for calculating the near-field enhancement of the nanoparticle surface. In the case of coupled nanoparticles, the interaction energy (U) between two nanoparticles can be written as follows [47]:

$$U = -k\frac{|p|^2}{4\pi\varepsilon_0\varepsilon_m s^3}, \qquad \textbf{2.20}$$

where s is the distance between two dipoles, and k is the coefficient that shows the relative orientation of dipoles to each other; where ε_0 is the vacuum permittivity, and ε is the dielectric function of the material; and where p is the dipole moment. In the case of a longitudinal mode, when the dipoles are oriented attractively to each other, k equals 2; in the case of a transverse mode, when the dipoles are oriented repulsively to each other, coefficient k equals 1.

Figure 2.6 illustrates that the electromagnetic field enhancement for two plasmonically coupled spherical nanoparticles depending on the orientation of the light polarization. The strongest coupling - and therefore, the strongest electromagnetic field enhancement - is achieved

when the dipoles are oriented attractively to each other, or when the polarization is parallel to the longest axis of the dimer. When the dipoles are oriented repulsively, the coupling and the electromagnetic field enhancement are significantly lower.

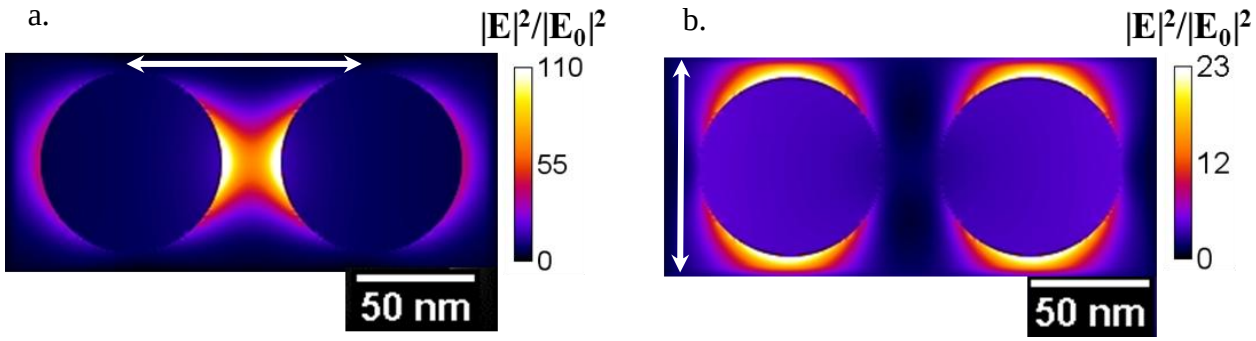

Figure 2.6. FDTD simulations of electric field enhancement between dimers of gold nanoparticles. Projections of calculated intensities of the electromagnetic field enhancement between two gold nanoparticles with a diameter of 60 nm and a distance of 10 nm between them under incident light with linear polarization parallel to the longest axis of the dimers (a) and perpendicular to the longest axis of the dimers (b). Simulations were performed at wavelengths of 537 nm (a) and 524 nm (b), assuming that glass was the substrate. Linear polarized light was injected with respect to the orientation of the longer axis of such a dimer. White arrows show the direction of light polarization in both cases. The colored scale bar represents the enhancement factor of the electric field compared with the incident field. For light polarizations parallel to the longest axis of the dimer, the electric field enhancement factor reaches values of 110; for polarization perpendicular to the longer axis of the dimer, the value is – 23.

Near-field enhancement in bow-tie structures.

Three different cases of electromagnetic field enhancement are shown: around a single gold nanoparticle (Figure 2.2), a single nanorod (Figure 2.3), and coupled nanoparticles (Figure 2.6). Direct comparison of the factor of electromagnetic field enhancement leads to the conclusion that electromagnetic field enhancement is stronger for coupled nanoparticles if the light is polarized parallel to the longest axis than for a single gold nanoparticle. Nevertheless, the strongest near-field enhancement can be expected at the sharp tips of the gold nanorods under linear polarization parallel to the longest axis of the rod. The possibility of combining plasmonic coupling between two nanoantennas, and the possibility of forming a "hot spot" with strong near-field enhancement at sharp tips give rise to the exploration of new geometries of plasmonic nanoantennas, e.g., bow-tie or nanotriangle nanoantennas [54].

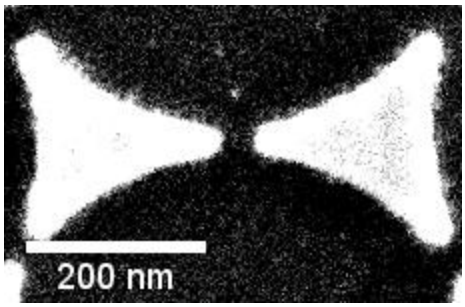

Figure 2.8. SEM image of bow-ties nanoantennas. Two gold nanotriangles are faced towards each other with the tips.

Bow-tie nanoantennas consisting of two nanotriangles with facing tips have been extensively studied during the past decade [48]. Figure 2.8 shows an example of bow-tie plasmonic nanoantennas. Sharp tips allow one to confine light to deep subwavelength dimensions [49]. Bow-tie nanoantennas have been used to enhance molecular fluorescence [50], in Raman scattering [51], in a plasmonic quantum cascade laser [52], and for near-field manipulation [53]. Bow-tie nanoantennas provide the unique possibility of controlling optical properties over a large range of wavelengths via controlling their geometrical parameter, e.g., side length [54], gap size [54,55,56], and shape [54]. The most pronounced plasmonic modes in nanotriangles are associated with dipolar and quadrupole excitations, which corresponds to near-field enhancement at the corners (for the dipolar modes) and at the edges (for the quadrupole mode) [57,58]. In case of gold nanotriangles an increase in aspect ratio (ratio between side length and height of nanotriangles) leads to the observation of quadrupole modes or higher-order modes (shorter wavelengths), which can be clearly identified in extinction spectra [57]. In Figure 2.7, the dipolar mode wavelength versus the edge length of a nanotriangle is

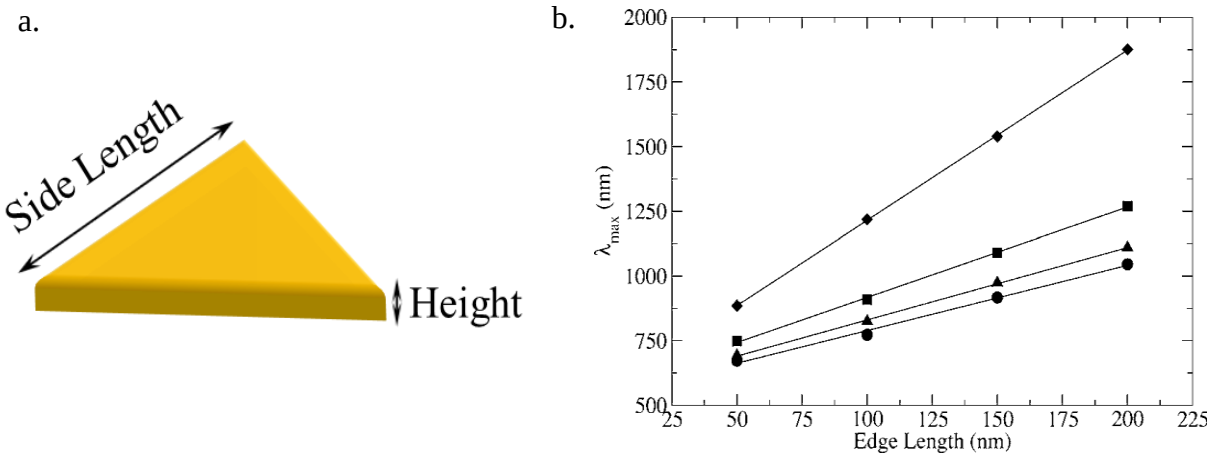

Figure 2.7. **Optical properties of gold nanotriangles vs. nanotriangle geometry.** A gold nanotriangle is illustrated (a). Side length and height of nanotriangle are indicated in the images. Dependence of extinction peak wavelength on nanotriangle's edge length is calculated and shown (b). The height of the nanoatriangle varied and was determined to be 5 nm (for spherical symbols), 10 nm (for square symbols), 15 nm (for triangle symbols), and 20 nm (for circle symbols). Reprinted with permission from [57]. Copyright (2005) American Chemical Society.

presented. When the height of a nanotriangle increases, the plasmon resonance shifts to the longer wavelength region. Furthermore, the plasmon resonance shifts linearly to the infrared (IR) region with an increase in the edge length of the nanotriangle [57]. In plasmonically coupled gold nanotriangles with tips directed toward each other, optical properties and an electro-magnetic enhancement depend on the distance between the tips.

So far, no analytical approach is available for predicting local surface plasmon resonance (LSPR) or for calculating the near-field enhancement factor in such structures. Hence, new numerical approaches, such as discrete dipole approximation (DDA) or finite difference time domain method (FDTD), have emerged recently [59] and have been intensively used. In Chapter 5.1, the FDTD simulations of near-field enhancement around gold nanotriangles will be provided.

2.1.4. Plasmonic heating.

Under electromagnetic radiation, energy is converted from incident light into the collective oscillation of electrons in gold nanostructures (surface plasmons) [60]. After excitation, surface plasmons can decay in different ways. Basically, two main energy loss mechanisms are distinguished: radiative decay, which consists of the elastic scattering of light, and non-radiative decay, which results in heat generation in gold nanostructures and therefore in the increasing

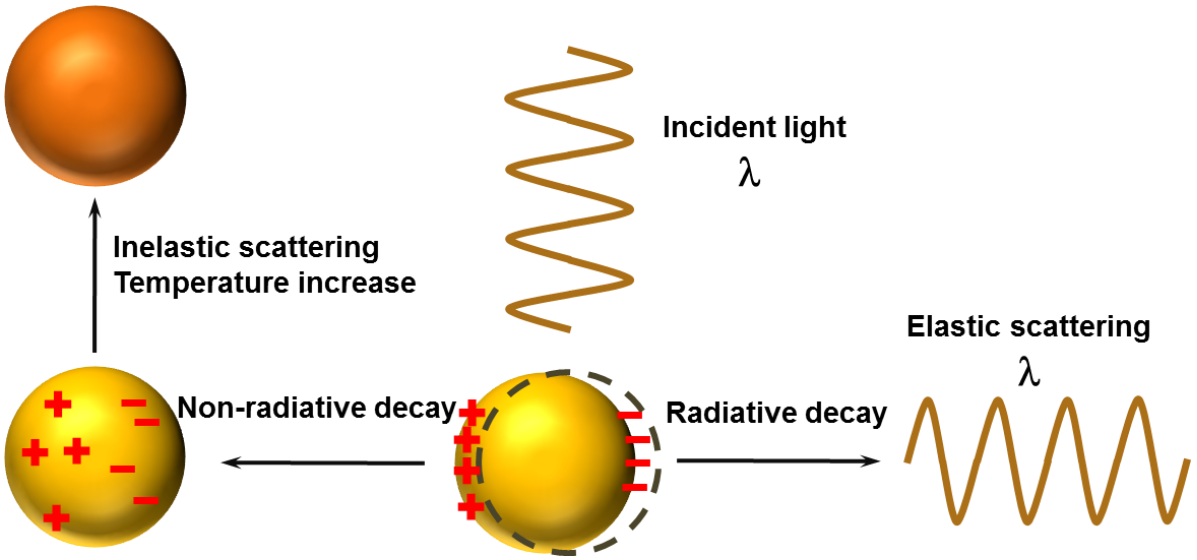

Figure 2.9. Two principal ways of localized surface plasmons to decay. The radiative decay results in elastic scattering and in the emitting of light with the same wavelength. The non-radiative decay consists of the inelastic scattering of the electrons and leads to the temperature increase of the gold nanostructure.

temperatures of the gold nanostructures and their surroundings (Figure 2.9). This section focuses on non-radiative plasmon decaying. Non-radiative decay consists of incoherently oscillating electrons and the subsequent transfer of energy from electrons to phonons through electron-electron and electron-phonon interactions, which leads to an increase in the temperatures of the gold nanostructures [19,61]. Because gold nanoparticles in contrast to dyes possess low photoluminescence quantum efficiency, they transfer almost all absorbed energy of incident illumination into heat [62]. The heat generation and temperature increase strongly depend on the absorption cross section of the gold nanostructures. As already discussed in the previous chapter, for small particles, greater absorption is expected along with less scattering, and vice versa for large particles. Gold has a high thermal conductivity [63,64]; hence, the temperature becomes uniform over the entire gold nanostructure almost immediately.

Gold nanostructures under electromagnetic illumination placed in a surrounding medium generate heat, which diffuses away from gold nanostructures' surfaces. Heat diffusion can be described by the following [65]:

$$\rho(r)c(r)\frac{\partial T(r,t)}{\partial t} = \nabla k(r)\nabla T(r,t) + Q(r,t), \qquad \textbf{2.21}$$

where $\rho(r)$ is the density, $c(r)$ is the heat capacity, $T(r,t)$ is the temperature at the r - a position at time t, and $k(r)$ is the thermal conductivity of the surrounding medium. $Q(r,t)$ is a heat source, which, in our case, is a gold nanostructure under electromagnetic irradiation. The local temperature distribution around a gold nanoparticle that reaches thermal equilibrium (steady-state condition) can be calculated as follows [65]:

$$\Delta T(r) = \frac{V_{NP}Q}{4\pi k_0 r}, \qquad \textbf{2.22}$$

where r is the distance from the center of the gold nanoparticle, k_0 is the thermal conductivity of the surrounding medium, and V_{NP} is the nanoparticle's volume. The equation is valid only for $r > R_{NP}$, where R_{NP} is the nanoparticle radius. For calculating absorbed heat Q, another equation can be used:

$$Q = \frac{\sigma_{abs} I}{V_{NP}}, \qquad \textbf{2.23}$$

where σ_{abs} is the absorption cross section of the gold nanoparticle, and I is the power density of electromagnetic irradiation.

2.1.5. Optical forces.

In 1970, A. Ashkin first reported the possibility of trapping and accelerating particles 2.68 μm in diameter with laser radiation [66]. This approach was later extended to smaller objects - for instance, to spheres 200 nm in size [67]. For objects with remarkable size differences, various regimes are valid, and different approaches to understanding and explaining optical forces have been introduced. The illustration of the different regimes described above is given in Figure 2.10. The regime, where the size of object α is much smaller than the light wavelength ($\alpha<<\lambda$), is called the Rayleigh regime. In this regime, a propagating laser light interacts with a particle in such a manner that the scattering force is proportional to term $1/\lambda^4$. The second regime is when the size of an object is much larger than the wavelength of incident light. In this case, the interactions can be described in terms of ray optics. When the particle is placed in the center of the beam, the individual rays pass the particle without changing the direction of propagation, and no additional internal forces are created. The situation changes when the particle is no longer in the center of the beam. When the rays enter and exit the particle, the particle will refract the rays. Therefore, the light will exit the particle at different angles from the original direction of propagation. According to the law of the conservation of momentum, a change in the direction of

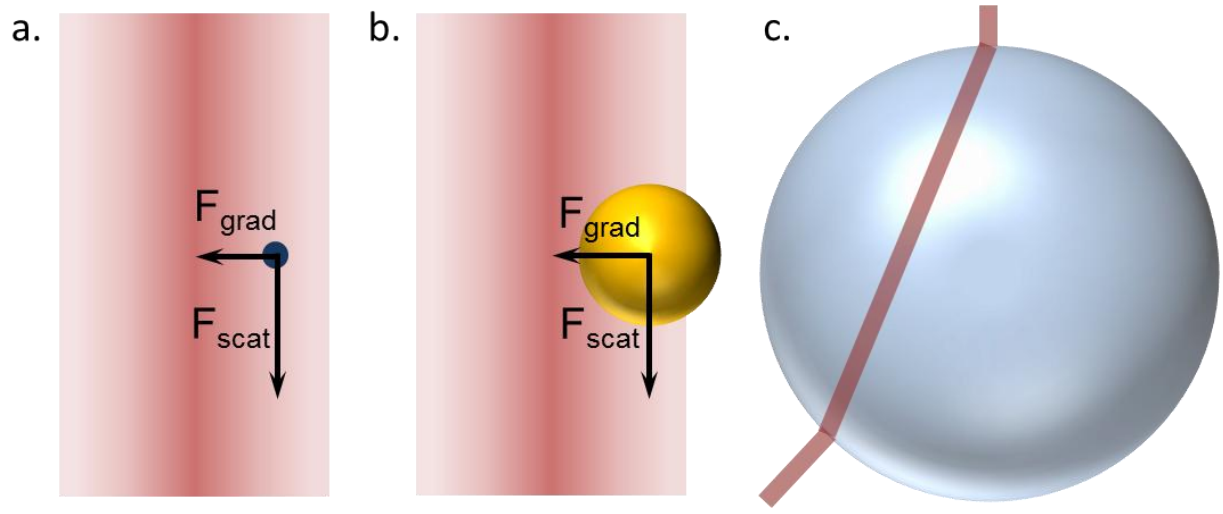

Figure 2.10. Three different regimes for optical forces on trapped object are shown. The Rayleigh regime, when the particle size is much smaller than the wavelength of incident light (a). The Mie regime, when the size of the object is comparable to the wavelength of incident light (b). Ray optics corresponds to the case when the size of the object is much larger than the wavelength of the incident light and the beam diameter (c).

exiting light leads to the creation of equal and opposite momentum, which affects the particle position. This internal momentum pushes the particle toward the region of the most intense light. The third regime that should be described is the Mie regime. When the interaction takes place between light and the objects with size $a \approx \lambda$, it takes place in the Mie regime. Because most of the objects used in this work have sizes comparable to the wavelength of light, the main focus here will be on the third regime.

In the Mie regime under light illumination, the particle behaves as a dipole with charges q and velocity v under electric and magnetic fields E and B [20,68]. Then, the Lorentz force can be expressed as follows [28]:

$$F_{Lorentz} = q\big(E(r,t) + v(r,t) \times B(r,t)\big). \qquad \textbf{2.24}$$

The substitution of the charge of a dipole q with dipole moment $p(r,t)$ leads to the following expression for the electromagnetic force:

$$F(r,t) = [p(r,t)\nabla]E(r,t) + \frac{dp(r,t)}{dt} \times B(r,t). \qquad \textbf{2.25}$$

The dipole moment of the particle can be written as follows [28,69]:

$$p(r,t) = \varepsilon_m \alpha E(r,t), \qquad \textbf{2.26}$$

where $\varepsilon_m = n_m^2 \varepsilon_0$ is the dielectric function of the medium, $n_m$is the refractive index of the medium, ε_0=8.854 x 10^{-12} F/m is the vacuum permittivity, and α is the polarizability of the particle [28, 70].

By applying the equation for the polarization of dipole $p = \alpha E$ and vector analysis equality $(E \cdot \nabla)E = \nabla\left(\frac{1}{2}E^2\right) - E \times (\nabla \times E)$ in Maxwell's equation, $\nabla \times E = -\frac{\partial B}{\partial t}$, equation 2.25 can be written as follows:

$$F(r,t) = \alpha \varepsilon_m \left[\frac{1}{2}\nabla E(r,t)^2 + \frac{d}{dt}(E(r,t) \times B(r,t))\right]. \qquad \textbf{2.27}$$

By averaging equation 2.27 over period $T = \frac{1}{\omega}$ and taking into account the complex character of polarizability α (for gold nanoparticles, $\alpha = \alpha' + i\alpha''$) equation 2.27 can be presented as follows:

$$F(r) = \frac{\varepsilon_m}{4}\left(\alpha' \nabla\big(\bar{E}(r)E(r)\big) + \alpha'' Im\left\{\sum\nolimits_i \bar{E}_i(r)\nabla E_i(r)\right\}\right), \qquad \textbf{2.28}$$

where E_i is the complex conjugate of E_i. The force in the last equation 2.28 can be divided into two components: gradient force and scattering force:

$$F(r)_{grad} = \frac{\varepsilon_m}{4}\alpha'\nabla\left(\bar{E}(r)E(r)\right) \qquad \textbf{2.29}$$

and

$$F(r)_{scat} = \frac{\varepsilon_m}{4}\alpha'' Im\left\{\sum_i \bar{E}_i(r)\nabla E_i(r)\right\}. \qquad \textbf{2.30}$$

The scattering force has the same direction as the Poynting vector $\boldsymbol{S}$ of the incident electromagnetic radiation. An alternative way of calculating scattering force F_{scat} is as follows [71]:

$$\langle F_{scat}\rangle = \frac{\varepsilon_m^2}{c}(\sigma_{scat} + \sigma_{abs})\langle S\rangle. \qquad \textbf{2.31}$$

The so-called gradient force $F(r)_{grad}$ is a part of equation 2.28, which depends on the real part of complex polarizability α'. The force acts along the intensity gradient toward the highest intensity. For the tightly focused Gaussian laser beam, the highest intensity is in the focal plane, where the potential reaches its minimum, and the gradient force is the strongest. Therefore, optical trapping takes place [72,73].

The scattering force $F(r)_{scat}$ depends on the imaginary part of complex polarizability α''. The dependence of optical forces on different parts of the complex polarizability of the particle, e.g., the gradient force, depends on real part α', and the scattering force depends on imaginary part α'', thus allowing one to choose different regimes for optomechanical manipulations. Figure 2.11 presents the dependence of complex polarizability on the light wavelength for a spherical gold nanoparticle with an 80-nm diameter in water. As one can notice, the real part of polarizability changes the sight from negative to positive; then, the gradient force changes from repulsive to attractive. Therefore, when the real part overcomes the imaginary part and is positive, one can expect stable optical trapping. In the case shown in Figure 2.11, stable optical trapping could be achieved between 600 and 1000 nm. When one chooses the light source with a wavelength close to plasmon resonance, the scattering force possesses the highest means, and therefore, optical printing could be performed under chosen experimental conditions.

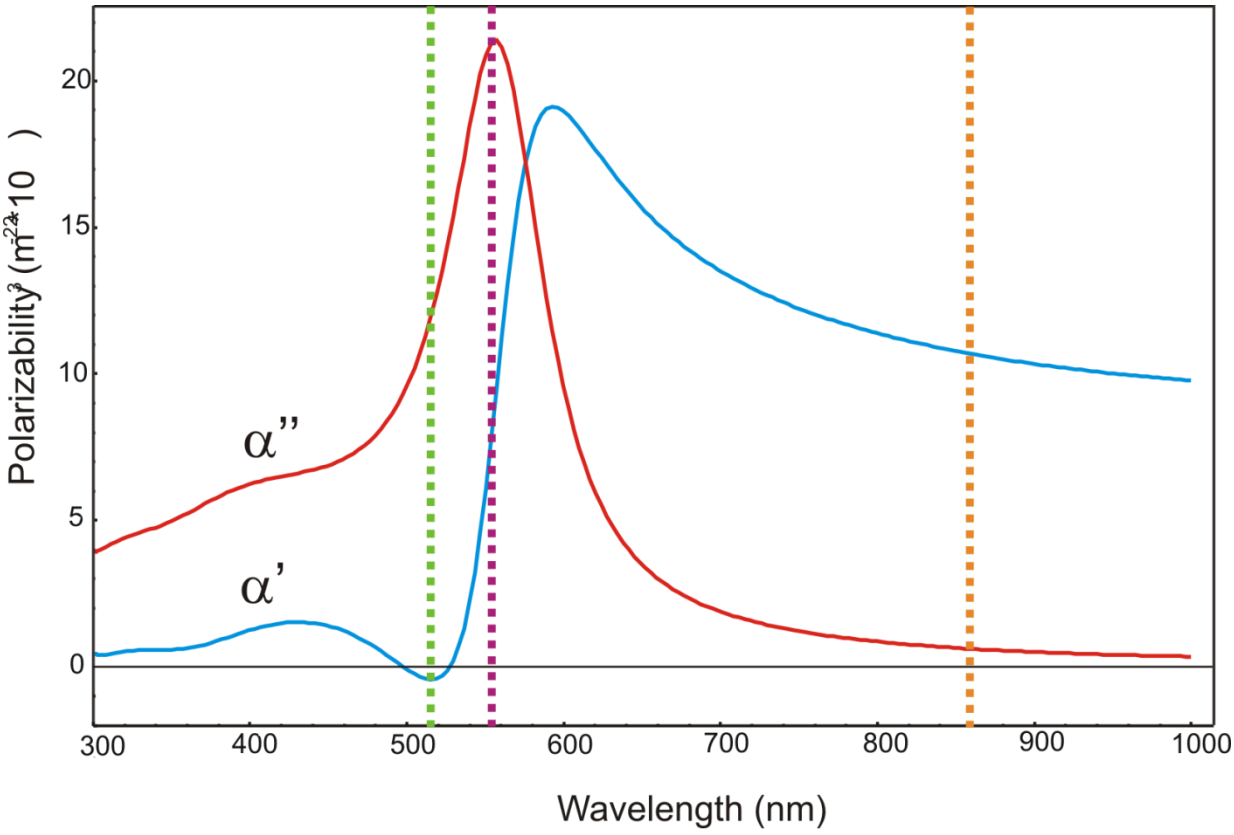

Figure 2.11. Complex polarizability of gold nanoparticles. The real part of polarizability is illustrated as a blue line, and the imaginary part as a red line. The diameter of a gold nanoparticle is 80 nm, and the refractive index of the medium is 1.33. The green vertical line shows the wavelength region where the gradient force is maximally repulsive; the purple line represents wavelengths with the strongest scattering force. The orange line indicates the region where the gradient force is attractive.

If the geometrical parameters of the investigated nanoparticle are changed, e.g., the diameter, the asymmetry of the system (nanorods, nanostars), or the refractive index of the surrounding medium, the complex behavior of the polarizability changes as well. In Figure 2.12, the complex polarizability of gold nanorods each with a diameter of 20 nm and a length of 120 nm in a medium with a refractive index of 1.33 (water) is presented. The maximum of the imaginary polarizability is shifted to 1064 nm compared with spherical gold nanoparticles (corresponding to the longitudinal plasmon resonance). Therefore, optical printing is most efficient with 1064 nm wavelength light, and stable optical trapping can be achieved by using light with wavelengths larger than 1200 nm.

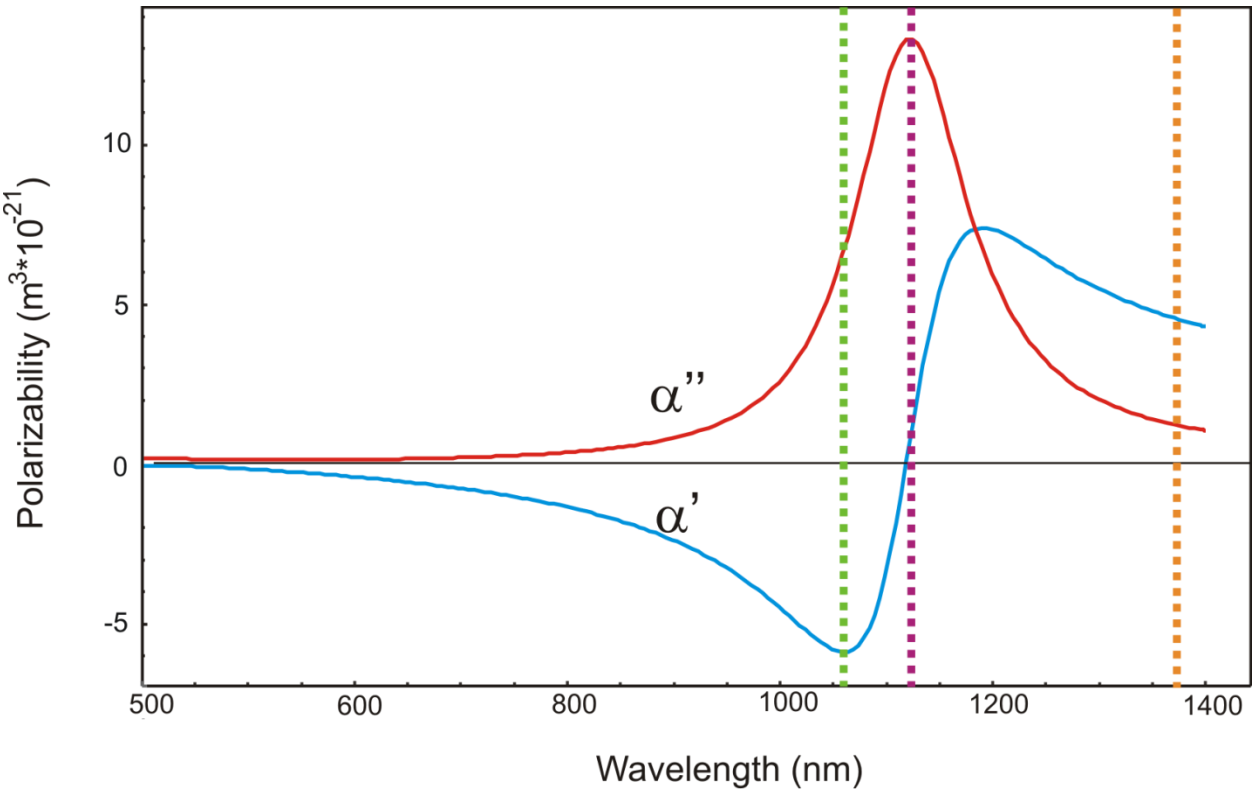

Figure 2.12. Complex polarizability of gold nanorods. The real part of polarizability is illustrated as a blue line, and the imaginary part as a red line. The diameter of the gold nanoparticle is 20 nm, the total length is 120 nm, and the longitudinal plasmon resonance takes place at 1064 nm. The refractive index of the medium is 1.33. The green vertical line shows the wavelength region where the gradient force is maximally repulsive; the purple line represents wavelengths with the strongest scattering force. The orange line indicates the region where the gradient force is attractive.

The complex behavior of the polarizability of gold and its dependence on the experimental conditions and properties of the regarded nano-object offer many opportunities to manipulate nano-objects and to tune experimental parameters.

Using the refractive index of water (1.33), a laser wavelength of 1064 nm, the scattering and absorption cross sections of straight nanorods at 1064 nm, and an objective with numerical aperture NA 1.0, the optical forces acting on a straight gold nanorod at 0.45 MW/cm^2 were calculated and are shown in Figure 2.13. Under resonant illumination, the scattering force dominates and overcomes the gradient force. Therefore, the total force acting on a gold nanorod in a laser beam is repulsive and leads to the optical printing.

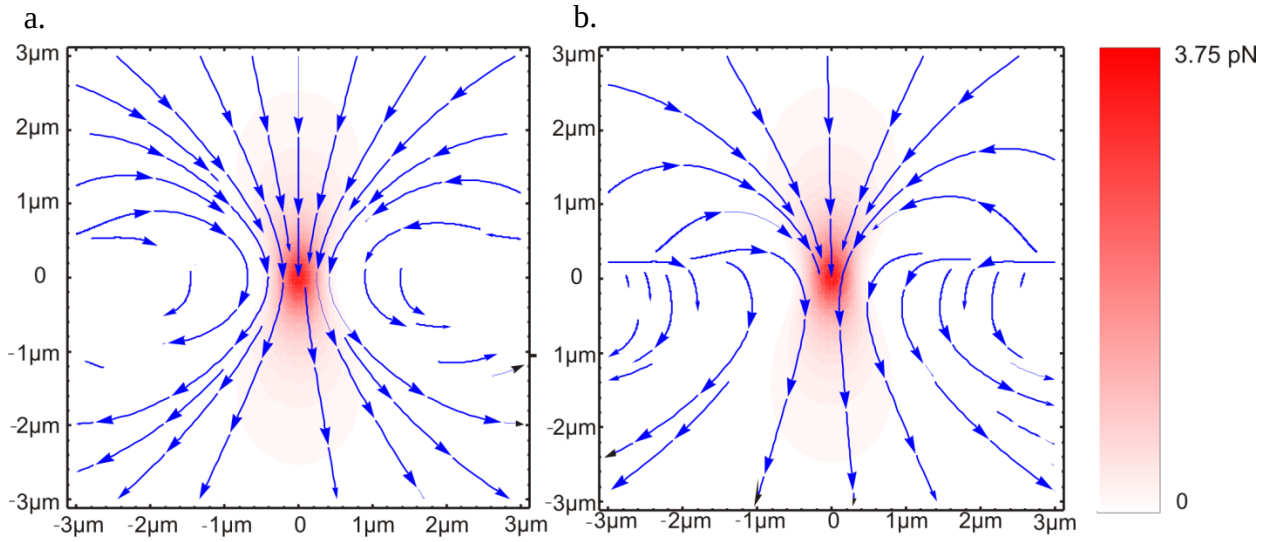

Figure 2.13. Optical forces acting on a straight gold nanorod under resonant irradiation with an near-infrarred (NIR) laser. Scattering force (a) and total force (b) acting on a straight gold nanorod are presented. The forces are calculated for a straight gold nanorod with a longitudinal plasmon resonance at 1064 nm, in a laser beam with a wavelength of 1064 nm. The laser power was 4.4 mW (0.45 MW/cm^2), and a water-immersion objective with NA=1.0 was used. The scattering and absorption cross sections of the straight nanorod were taken as 1.9735 and 3.98928* 10^{-14} m^2, respectively.

3. Methods and Characterization.

This section describes experimental setups, sample fabrication procedures, and characterization methods. The first part provides an overview of a dark field microscope coupled with lasers. This setup has been used to print and bend gold nanorods and to trap silica beads. The section about scattering Rayleigh spectroscopy on single objects and about transmission and absorption spectroscopy on ensembles is presented. These sections are followed by a description of scanning electron microscopy along with transmission and high-resolution transmission electron microscopes, which have been used to characterize the morphology of nanostructures (geometry, shape, and orientation in space) as well as to investigate the crystal structure of bent gold nanorods. Combined, these techniques provide full information about the sample's morphology, optical properties, and crystal structure.

3.1. Experimental techniques.

3.1.1. Optical characterization.

Dark-field microscopy.

Dark-field microscopy is an example of optical microscopy, where image contrast is achieved by collecting only scattered light from a sample. The principle of dark-field microscopy (DFM) can be described as follows. A condenser is designed in such a way as to form a hollow cone of propagating light. A light-collecting objective is located in a dark hollow cone formed by the condenser. Therefore, the illumination from the light source will be blocked out; only the light scattered from the investigated object will be collected. The field of view appears dark except for a light-scattering sample that appears bright. To obtain good-quality dark-field conditions, the numerical aperture of the objective has to be smaller than the numerical aperture of the condenser. Otherwise, the objective will collect the incident light, thus disturbing the observation of the sample and degrading the image quality.

Owing to these plasmonic properties, gold nanoparticles are excellent light scatters. Thus, it is possible to observe single particles in a dark-field microscope, even though their sizes are well below the diffraction limit. The colors of gold nanoparticles correspond to their plasmon resonance. In Figure 3.1, dark-field images of spherical gold nanoparticles that are 40 nm, 60 nm, and 80 nm in diameter are shown. The particles display 560-nm (green), 580-nm (green-yellow), and 600-nm (yellow-red) plasmon resonance wavelengths in water.

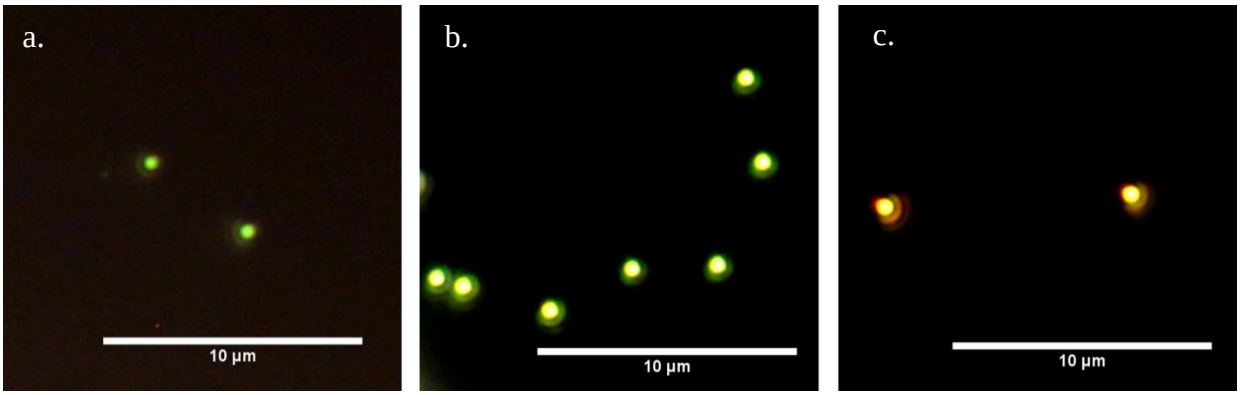

Figure 3.1. Dark-field images of gold nanoparticles. Gold nanoparticles with sizes of 40 nm (a), 60 nm (b), and 80 nm (c) on glass substrate in water. The scattered light color changes from green to yellow with an increase in the nanoparticle's diameter.

To increase the contrast between scattered light from nanoparticles and the sample background, a substrate should be thoroughly cleaned before an experiment to remove unwanted scatterer, such as dust. In this work, a standard cleaning protocol was used. Glass cover slips (24 x 24 mm) with a thickness of 0.17 mm were cleaned in three steps - in isopropanol (10 minutes), acetone (10 minutes), and Milli-Q water (10 minutes) in an ultrasonic bath - and blow dried with nitrogen.

A schematic illustration of the optical setup is presented in Figure 3.2. It includes a conventional upright microscope, Zeiss Axio Scope A1 from Zeiss GmbH, coupled with a 100-W halogen lamp that covers the whole visible spectrum of light. The oil dark-field condenser Zeiss Axio Scope A1 with an NA between 1.2 and 1.4 was used. To bring a condenser and a glass cover slip in contact with each other, immersion oil with a refractive index of 1.518 was

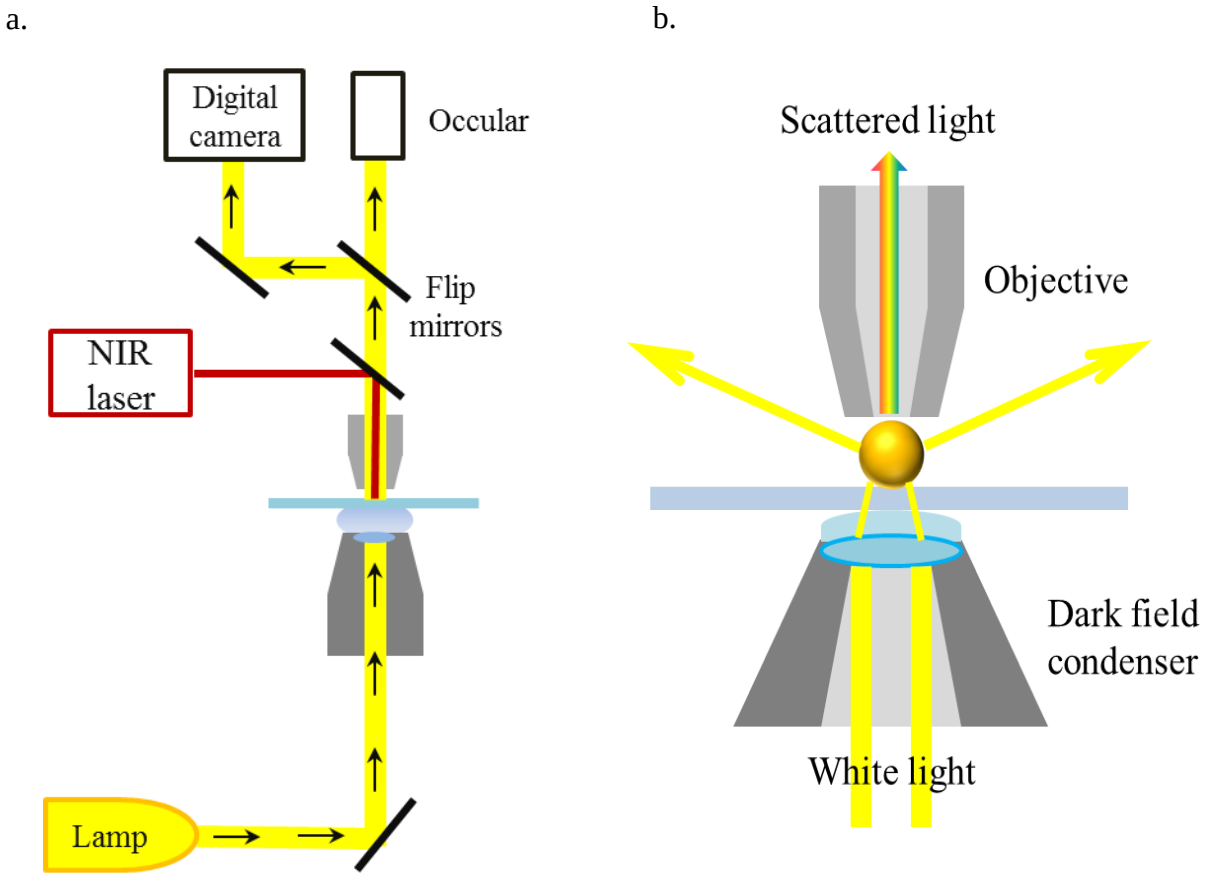

Figure 3.2. Dark-field microscopy principle. A dark-field microsopy (DFM) setup that was used for near-field trapping of silica beads and bending of gold nanorods with light is shown in (a). The main operating principle of a DFM is illustrated in panel (b).

used. Most of the experiments were performed with a light-collecting water immersion objective with a magnification of 100x and NA = 1.0. Scattered light from the sample was detected by using a digital camera (Canon 500D). It was possible to control the acquisition time to obtain the desired light intensity.

Rayleigh scattering spectroscopy.

Rayleigh scattering spectroscopy was performed on the Acton SpectraPro 2300i (Princeton Instruments) spectrometer. The spectrometer is equipped with different gratings that are sensitive to certain wavelength regions. The spectrometer is connected to a liquid nitrogen cooled charge coupled device (CCD) (Spec-1.0 by Princeton Instruments). The working region of the CCD is between 300 and 1050 nm. To perform polarization-dependent Rayleigh scattering measurements, a polarization filter (Thorlabs, Germany), optimized between 600 nm and 100 nm, was inserted into the optical path after the sample and before the spectrometer. The precise positioning of the sample was achieved with a sample holder with the remote control of movements in the XY directions.

Optical transmission and absorption spectroscopy.

The extinction spectra of plasmonic nanoantenna structures on glass substrates and gold nanorods in a solution were measured with a double-beam UV-Vis-NIR spectrometer (Cary Varian 5000) in a spectral range from 190 nm to 1700 nm. A baseline was recorded and used for signal correction. During a measurement, one light beam is sent through the sample, and the transmitted signal is collected by using the detector (I), while a second beam is used as a reference beam (I_0). After subtracting the baseline, the Beer-Lambert law can be applied, and the transmittance of a particular ensemble can be calculated with the following:

$$T = \frac{I}{I_0} = e^{-\tau} = 10^{-A}, \qquad \textbf{3.1}$$

where I is the light intensity that the substrate transmits, I_0 is the light intensity of the reference beam, τ is the optical depth, and A is absorbance.

3.1.2. Structural analysis down to atomic scale.

Scanning electron microscopy.

The resolution of optical microscopy is limited. The shape of nanoparticles simply cannot be resolved by using dark-field microscopy. In electron microscopy, an image is achieved with a focused beam of electrons. The electron wavelength can be calculated from the de Broglie relation and depends on the applied acceleration voltage U: $\lambda_e = \frac{h}{\sqrt{2eUm_e}}$, where h is the Plank constant, and e and m_e are the electron charge and mass, respectively. Under an accelerating voltage of up to 5kV, the wavelength is in the order of a few picometers. The operating principle of a scanning electron microscope (SEM) is based on the interaction of electrons with a sample. Inelastic or elastic scattering produces different types of electrons: secondary electrons, back-scattered electrons, characteristic X-rays, a specimen current, and transmitted electrons. All of this together contains information about the sample's topography and material. In this work, all SEM measurements were carried out with a Gemini Zeiss Ultra 55 SEM with a nominal resolution of 2 nm (Figure 3.3a). The spatial resolution of an SEM is based on the size of the electron spot, which is defined both by the wavelength of electrons and by the electron-optical system. Besides that, the resolution is limited by the volume of the specimen that interacts with the electron beam.

Depending on the type of detected electrons, different detectors and configurations and geometries of SEMs exist. In this work, SE2 and In-Lens detectors for secondary electrons were mainly used. The In-Lens detector operates under an applied acceleration voltage of between 100V and -20kV and registers only the secondary electrons that the primary electron beam generates directly. Hence, only the electron beam diameter limits the resolution of the In-Lens detector. The typical working distance for the In-Lens detector is less than 10 mm. However, the SE2 detector operates at an applied accelerating voltage of 1–30kV and at working distances larger than 4 mm. This detector registers the secondary electrons, which backscattered electrons generated in the sample and which were returned to the surface. The SE2 detector covers an area bigger than the electron beam diameter.

Transmission electron microscopy.

In transmission electron microscopy (TEM), more attention is paid to electrons that do not deviate far from the incident-electron direction. In TEM, electrons pass through the specimen

and are scattered in a "forward direction" (scattering angle of < 90°). A simple illustration of the operating principle of TEM can be described as follows: A system of electromagnetic lenses and apertures focuses the electrons that an electron source emits, and these electrons are guided toward a sample (Figure 3.3b). Afterward, a system of objective and imagining lenses focuses the electrons transmitted through the sample, and the electrons reach a phosphorescent screen, where the final image is projected. By applying the equation for the electron wavelength provided in the previous chapter and taking into account the accelerating voltage of 80–100 kV in TEM, one can expect the resolution to be below 1 nm. The main limitation of TEM is the diffraction limit, which restricts the resolution down to 10^{-7} m. Electrons with higher energies

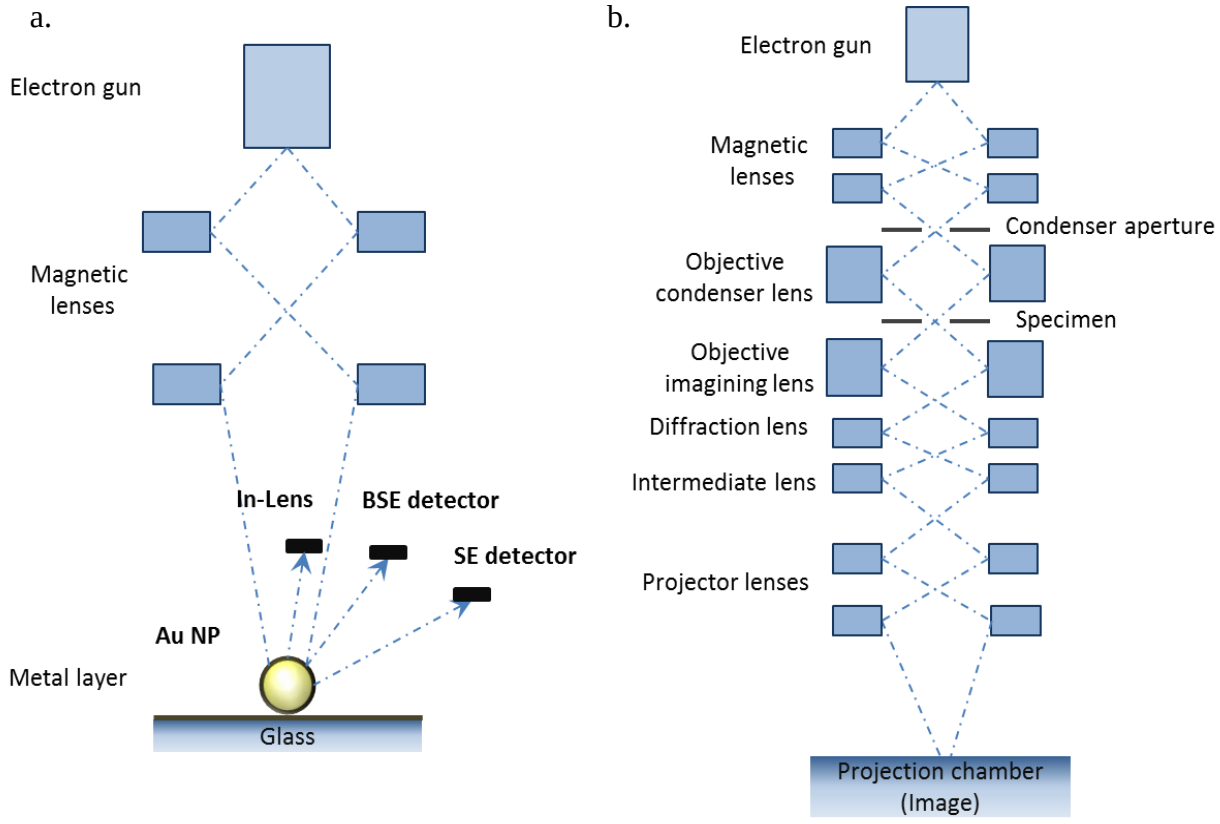

Figure 3.3. Operating principles of SEM (a) and TEM (b). A schematic view of an SEM is provided (a). Electrons are accelerated and focused on the sample by using magnetic lenses. Depending on the types of scattered electrons from the sample, different detectors collect the electrons. In the case of a non-conductive sample, a thin metal film should be put on top of a substrate to prevent charging. An SEM image of gold nanorods on a glass substrate is given. A schematic view of TEM is given (b). Electrons accelerated by magnetic lenses pass objective condenser lenses; therefore, a primary beam is formed. Objective imagining lenses focus the electron beam that went through the specimen. The projector lenses expand the electron beam onto the phosphor screen, where the final image is formed.

and therefore smaller wavelengths allow for resolving objects down to 10^{-10} m, which is comparable to the sizes of atoms. Along with diffraction limitations, three types of aberrations exist, which affect the resolution of this method: spherical aberrations, chromatic aberrations, and astigmatism are known. Therefore, in TEM, different lenses are applied for correcting aberrations and for improving the spatial resolution. Typical values for the spatial resolution with TEM are between 0.25 and 0.3 nm [74, 75].

High-resolution transmission electron microscopy (HRTEM) was used in this thesis for completing a detailed analysis of the crystallographic changes that took place during gold nanorod melting and bending. All HRTEM measurements were carried out using a probe-corrected FEI Titan Themis at 300 kV. Compared to TEM, in HRTEM, the image is formed due to interference between the forward-scattered and diffracted electron waves from the specimen. All electrons emerging from the sample pass the objective and magnifying lenses to form a final-phase contrast image. The final image is a phase-contrast image. The HRTEM technique provides many opportunities, such as the selective imaging of sub-lattices, imaging interfaces, and surfaces (stacking faults, twin boundaries), using electrons scattered to large angles for z-contrast and resolving single atoms in scanning transmission microscopy (the STEM mode). In the STEM mode, the final image forms by scanning over the sample with a small probe. The resolution depends on the size of the initial probe of the source. In addition, with an SEM, different detectors are available in TEM, and the choice of detector depends on the types of electrons detected. In this thesis, measurements were performed in the high-angle annular dark-field mode (HAADF). Therefore, the detector collected the transmitted electrons that were scattered to high angles [76].

Crystal structure analysis.

Solid crystals feature a certain atomic organization and ordering. The crystal structure of solid substances can be imagined as infinite periodic small boxes in all three spatial directions. Each small box is called a unit cell and is defined as the smallest unit of volume that contains all of the essential information about the structure and symmetry [77]. Using these parameters, the position of every atom in the crystal can be precisely determined and described. Seven lattice systems exist in a three-dimensional (3D) space: cubic, hexagonal, rhombohedral, tetragonal, orthorhombic, monoclinic, and triclinic. In this chapter, mainly the cubic lattice system will be described, where all three lengths of the cell edges are equal to one another, and where all three

angles are 90°. Three main types of cubic crystal system are known: primitive cubic (simple cubic), body-centered cubic (bcc) and face-centered cubic (fcc). Ionic compounds, such as NaCl, KCl, PbS, and MgO, possess a primitive cubic crystal structure; alkali metals (K, Na, Cs) and transition metals (W, Fe, Cr, V) have a body-centered cubic crystal structure; and most of the noble metals (Al, Cu, Ag, Au, Pt, Pd) and transition metals (Ni, Ir) are assigned to a face-centered cubic crystal structure [78,79].

As a common notation system in crystallography, Miller indices are used. Miller indices (*hkl* or *uvw*) describe the position of atom planes in a crystal [77,80]. The coefficients of *hkl* define reciprocal vectors $\mathbf{r}^{\mathbf{I}}=h\mathbf{a}^{\mathbf{I}}+k\mathbf{b}^{\mathbf{I}}+l\mathbf{c}^{\mathbf{I}}$, whereas the coefficients of *uvw* define direct space vectors $\mathbf{r}=u\mathbf{a}+v\mathbf{b}+w\mathbf{c}$. Miller indices with different brackets have different meanings in crystallography. The notation of {*hkl*} corresponds to the set of planes that are equivalent to *hkl* by symmetry transformation. The Miller indices of [hkl] indicate a direction on the basis of the direct lattice vectors. The Miller indices of <*hkl*> define the set of all directions that are equivalent to [*hkl*]. In the case of cubic structures, the Miller indices denote vectors in Cartesian coordinates.

For a cubic lattice, the spacing between lattice planes can be calculated as

$$d_{hkl} = \frac{a}{\sqrt{h^2 + k^2 + l^2}}, \qquad \textbf{3.2}$$

where *d* is the spacing between lattice planes, *a* is the lattice constant, and *hkl* are the Miller indices [77]. Figure 3.4 illustrates some crystallographic planes with Miller indices for cubic crystals.

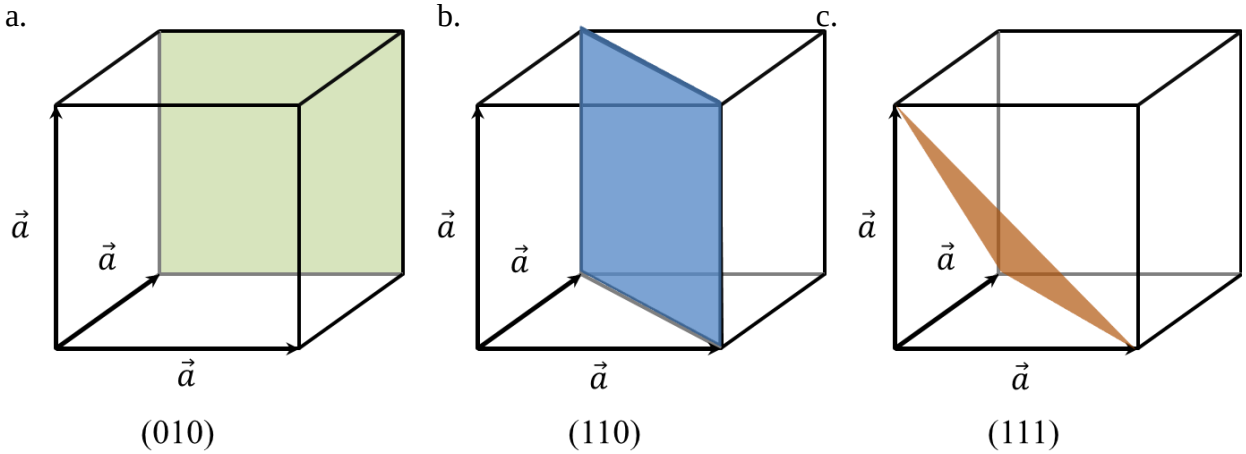

Figure 3.4. Example of Miller indices. Planes in cubic crystals with different Miller indices (010) (a), (110) (b), and (111) (c) are schematically illustrated [28].

Real crystals may contain defects in the ideal atom arrangement (Figure 3.5a-c) [80]. A simple example of a defect is a point-like defect, which takes place in a volume of fewer than a few lattice constants. In other words, point defects occur only at or around a single lattice point. Two types of point defects exist: vacancy defects and interstitial defects (Figure 3.5b). The vacancy defects are empty lattice sites that were initially filled with certain atoms [28]. On the other hand, interstitial defects are atoms that occupy lattice sites in between the regular lattice. Nearby vacancy defects and interstitial defects together form Frenkel defects [28,80]. These point defects are difficult to detect; however, they influence the physical properties of crystals, e.g., ionic conductivity [28].

Another type of defect is the line defect. Common examples of line defects are dislocations and disclinations (Figure 3.5c) [28]. Due to lattice strain, atoms can move, creating a dislocation. Besides that, planar defects exist in a crystal, e.g., grain boundaries, stacking faults, or crystal twinning. The latter type of planar defects, crystal twining, will be the topic of focus here (Figure 3.5d). When a crystal has two parts that are oriented to each other with a certain symmetry law, one can say that twinning took place in the crystal. The most widespread symmetry law in twinning is the mirroring of the crystal structure along a crystal plane. Depending on the conditions, one can distinguish three types of twinned crystals: growth twins, annealing or deformation twins, and gliding twins. Growth twins form in a crystal during the growth process due to interruption; annealing twins form in crystals when they have cooled down; and gliding twins form under mechanical stress. Most commonly found is the twin defect in the fcc lattice along the (111) plane. In this case, one crystal part is the mirror of another part along the crystal plane (111) [81,82,83].

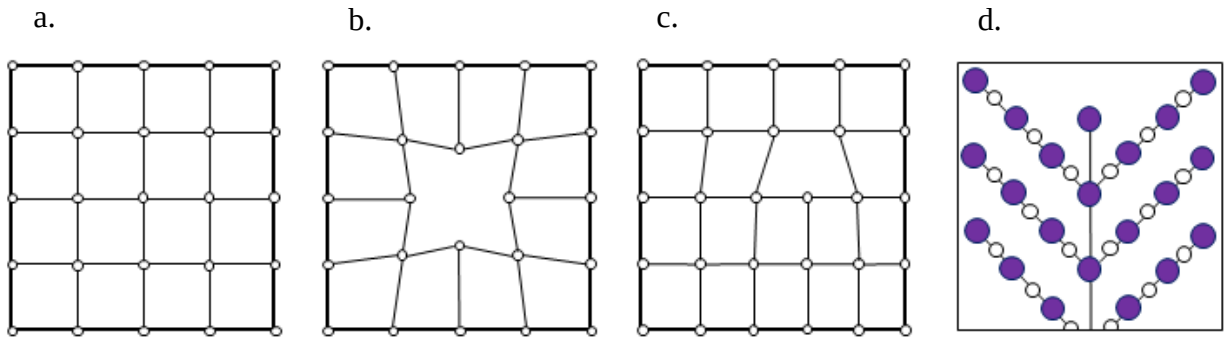

Figure 3.5. The ideal crystal structure and possible crystallographic defects are illustrated. (a) Ideal crystal without any defects, (b) vacation defect, (c) dislocation defect, (d) twin defect [28,81,82].

3.2. Calculations.

3.2.1. Optical forces.

All optical force calculations were performed with Mathematica, version 8.0 (Wolfram Research). Optical forces were calculated with the assumption that a tightly focused Gaussian beam irradiates plasmonic nanoparticles.

In cylindrical coordinates, one can write the equation for electric field distribution in a focused laser beam as follows [73]:

$$\mathrm{E(r,z)} = \mathrm{E_0}\sqrt{2/\pi}\frac{\mathrm{w_0}}{\mathrm{w}}\mathrm{e}^{-\frac{\mathrm{r}^2}{\mathrm{w}^2}}\mathrm{e}^{\mathrm{i}\left(\mathrm{k}\left(\frac{\mathrm{r}^2}{2\mathrm{R}}+\mathrm{z}\right)+\eta\right)}, \qquad \textbf{3.3}$$

where *k* is the wave vector, w_0 is the minimum width of the tightly focused Gaussian beam at the focal plane, and *w* is the width of the tightly focused Gaussian beam at different distances from the focal plane. The electric field amplitude in the focus can be calculated as follows:

$$E_0 = \frac{\sqrt{2\mu_0 c_0 P}}{w_0}, \qquad \textbf{3.4}$$

where *P* is the power of the laser beam, μ_0 is the vacuum permeability, and c_0 is the speed of the light in vacuum. Then w_0 can be calculated for an objective with numerical aperture NA as follows:

$$w_0 = \frac{\lambda}{\pi * NA}, \qquad \textbf{3.5}$$

where λ is the wavelength of the incident light. The width *w* of the focused laser beam changes along beam propagation axis z according to the following equation:

$$w(z) = w_0\sqrt{1 + (z/z_0)^2}, \qquad \textbf{3.6}$$

where z_0 is the distance e to the beam waist, where the beam cross section area is doubled, and:

$$z_0 = \frac{\pi w_0^2 n}{\lambda}, \qquad \textbf{3.7}$$

where *R* and η change with the dependence as follows:

$$R = z(1 + (\frac{z_0}{z})^2) \qquad \textbf{3.8}$$

and

$$\eta = tan^{-1}\left(\frac{z_0}{z}\right). \qquad \textbf{3.9}$$

For future calculations of optical forces, equations 2.29 and 2.30 are split into *r* and *z* components. The gradient force is given by:

$$F_{gradZ}(r,z) = -\frac{\varepsilon_0}{\pi}\alpha' E_0^2 \frac{r w_0^4}{z_0^2}\left(\frac{1}{w^4} - \frac{2r^2}{w^6}\right)e^{-\frac{2r^2}{w^2}} \quad \textbf{3.10}$$

and

$$F_{gradR}(r,z) = -\frac{2\varepsilon_0}{\pi}\alpha' E_0^2 \frac{r w_0^2}{w^4} e^{-\frac{2r^2}{w^2}}. \quad \textbf{3.11}$$

For the scattering force, one gets the following:

$$F_{scatZ}(r,z) = \frac{\varepsilon_0}{\pi}\alpha'' E_0^2 \left(k\left(1 - \frac{r^2}{2}\frac{(z^2 - z_0^2}{(z^2 + z_0^2)^2}\right) + \frac{w_0^2}{z_0 w_0^2}\right)e^{-\frac{2r^2}{w^2}} \quad \textbf{3.12}$$

and

$$F_{scatR}(r,z) = \frac{\varepsilon_0}{\pi}\alpha'' E_0^2 \frac{r w_0^2}{w^2}\frac{k}{R} e^{-\frac{2r^2}{w^2}}. \quad \textbf{3.13}$$

In this work, the optical forces were calculated for straight and bent gold nanorods propagating in a laser beam. The required absorption and scattering cross sections were calculated using the Software FDTD Lumerical Solution. Using absorption and scattering cross sections and equations 2.13–2.15, the real and imaginary parts of the polarizability of gold nanorods were derived, and afterward, they were implemented in equations 3.10–3.13.

3.2.2. Temperature.

Temperature profiles were calculated by solving the heat diffusion equation (equation 2.21) numerically. COMSOL Multiphysics version 4.2 (the "heat transfer" module) by FemLab was used, which implements the finite element method to discretize a given geometry and solves the differential equations on the resulting mesh with boundary conditions [84], such as object size and material, and the surrounding medium properties, such as heat transfer and insulation constants. Within the program, it is possible to design the desired shape and size of an object and to choose the proper material, e.g., gold or copper, with certain heat capacity and thermal conductivity values. This allows one to simulate steady-state conditions as well as the evolution of the temperature distribution over time.

The gold nanorod was modeled as a cylinder with two spheres at the ends with a length of 124 nm and a thickness of 21 nm. For large distances from the gold nanorod, the temperature was fixed as 293.15K. Absorption cross sections and the volume of gold nanorods, laser powers,

and the full width at half maximum (FWHM) of the focused laser beam were used as input parameters for the simulations.

3.2.3. Electromagnetic field enhancement.

Using the FDTD method, Maxwell's derivational equation can be solved. The changes in the electric field over time depend on the changes of the magnetic field across space, and vice versa. The electric and magnetic fields at each step are calculated taking into account the values at the previous step. The computational domain typically represents the region where the simulations will be conducted. One has to define the material and the permeability, permittivity, and conductivity of each cell of the computational domain. With FDTD, it is possible to analyze the response of the system over a wide range of frequencies. The major drawback lies in the calculation time.

Simulation of the charge distribution, electromagnetic field enhancement, and absorption and scattering cross sections.

For all simulations, the dielectric function of gold was taken from Johnson and Christy [22], and that of water from Palik [85]. Convergence tests were performed to determine the optimal mesh size.

Simulations of the absorption and scattering cross sections of bent nanorods were performed using Lumerical FDTD solutions (Lumerical Solutions, Canada). The bent gold nanorods were represented as two cylinders connected by a sphere and terminated by two spheres; they had a total length of 124 nm and a thickness of 21 nm. The bent nanorods with the desired bending angles were placed in the surrounding medium (water with refractive index 1,33).

FDTD simulations of gold nanotriangle pairs with varying sizes (thickness 30 nm, side lengths: 145 nm, 166 nm, and 196 nm) and tip distances (130 nm, 93 nm, and 46 nm) on a glass substrate in water were carried out using Lumerical FDTD solutions. The simulation volume of 1.2 x 1.2 x 1.0 μm^3 was confined with a stack of up to 64 perfectly matched layers with a reflection of 10^{-4}. Linear polarized light was injected with a total-field scattered-field source perpendicular to the substrate surface. In this setup, convergence was reached with a refined mesh size of 0.5 nm around the plasmonic particles.

3.2.4. Hydrodynamics.

Simulations of the hydrodynamic pressure acting on the gold nanorods under an external stationary laminar flow were performed by solving the Navier-Stokes equations using COMSOL Multiphysics software 5.2 (the "fluid flow" module).

$$\rho(u \cdot \nabla)u = \nabla \cdot [-pI + \mu(\nabla u + (\nabla u)^T] + F \qquad \textbf{3.14}$$

and

$$\rho\nabla \cdot (u) = 0, \qquad \textbf{3.15}$$

where u denotes the velocity [m/s], ρ corresponds to the density of water (1000 kg/cm^3), μ denotes the dynamic viscosity of water (0.001 Pa·s), p corresponds to the pressure [Pa], and I denotes the unity matrix. In the center of a water box (4 x 4 x 4 μm^3), a solid nanorod with a length of 124 nm and a diameter of 21 nm was placed. The rod experienced an external stationary laminar flow perpendicular to the longer axis of the gold nanorod. Under the assumption that the scattering force of 20 pN, which was calculated before, acted on spherical nanoparticles with a radius of 60 nm (the radius of the gold nanoparticle was fixed to be equal to the length of the gold nanorod), the Stokes drag equation for spherical particles was used to estimate a laminar flow speed as follows:

$$F_d = 6\pi\mu R\upsilon, \qquad \textbf{3.16}$$

where F_d is assumed to be equal to a scattering force of 20 pN, μ represents the dynamic viscosity of water (0.001 Pa·s), and R represents the particle radius. Here, υ denotes the velocity of the particle movement. Under specified conditions, gold nanoparticles with a radius of 60 nm experience a laminar flow with a speed of 0.02 m/s.

4. Bending gold nanorods with light.

Metamaterials gain their optical properties from the unique patterning of their individual building blocks. The precise geometry, orientation, and arrangement of the metamaterial components allow for the manipulation of electromagnetic waves in an unprecedented way.

Smith *et al.* [86] and Pendry [87] presented the first experimental demonstration independently in 2000. Nowadays, "negative-index" metamaterials are applicable for cloaking [88], sensing [89], super-lensing with a subwavelength resolution [90], and energy harvesting [91]. The crucial aspect of the manipulation of electromagnetic waves by using metamaterials is the precise shape control, size, and arrangement of the material. Because the individual building blocks of a metamaterial have to be smaller than the incident wavelength is, the common fabrication techniques are e-beam lithography [92,93], nanoimprint lithography [94], or focused-ion beam milling [95]. However, these techniques have certain limitations [96]. First, most nanotechnologies suffer from low throughput and are time-consuming techniques. The largest area that can be produced is around a millimeter. Second, the resulting nanostructures possess polycrystallinity and shape deviations, which can affect the interaction with incident light. Third, the average size of the repeating unit is in the range of a few hundred nanometers; therefore, the optical response of such metasurfaces takes place outside of the visible spectral range. For instance, Yu et al. showed that V-shaped antennas around 200 nm in size that have been fabricated by using electron beam lithography operate in the mid-infrared region of the spectra [97]. Only recently were the metasurfaces that work at visible wavelengths announced [98].

The optical printing of plasmonic particles can be considered as an alternative route to arranging particles on a substrate. Recently, the possibility of patterning gold or silver spherical nanoparticles on surfaces was experimentally demonstrated [99,100]. It was possible to extend this approach to gold nanorods and to optically print individual particles with a preferred orientation [101,102]. Optical printing is very efficient for a laser wavelength that is resonant with the localized surface plasmon of the particle and is generally not restricted to spheres or rods. This approach can be extended to all kinds of complex-shaped nanoparticles. Particles of various shapes have been chemically synthesized, including nanotriangles [103], nano-cubes [104], nano-wires [105], or nano-stars [106]. To date, however, no synthetic strategy is available to generate a V-shaped gold nanoparticle with a controlled angle.

Another method of changing the shapes and sizes of already-synthesized nanoparticles can be achieved via laser irradiation. Recently, different groups investigated intensively the reshaping of plasmonic particles [107,108]. They paid particular attention to the melting of gold nanorods under laser irradiation. In addition, several groups have extensively studied nanorod melting and re-shaping with femtosecond and nanosecond laser irradiation [109,110,111,112]. Link *et al.* [113] proposed the re-shaping mechanism of gold nanorods under pulsed laser irradiation. They showed that nanorod re-shaping starts in the interior of the rod with the creation of point and line defects, which eventually result in the formation of planar stacking defects and twins. Depending on the rate of the pulsed laser irradiation, the heating of gold nanorods can be divided into three steps. In the first step, the thermalization of the electron gas by absorbing pulse energy takes place for more than 100 fs. In the second step, electron-phonon thermalization happens during 3–4 ps. In the third step, the heat diffuses into the surrounding medium from the gold nanorods, and therefore, the gold nanorods are cooled. The third step lasts for more than 100ps [17]. When the short-pulsed (femtosecond-pulsed) laser irradiation is used, the gold nanorods stay in the heated condition. Link et al. also proved that melting with a femtosecond laser pulse is more effective for the formation of spherical nanoparticles, whereas an abundance of ϕ-shaped particles was observed when the nano-pulse laser was used. Taylor *et al.* [111] reported that the photo-thermal re-shaping of rods to spheres is even possible below the rod's melting temperature due to the curvature-induced diffusion of surface atoms. This is particularly true for rods with a large aspect ratio. Horiguchi *et al.* [114] studied the reshaping of gold nanorods with different passivating layers under pulsed laser irradiation. The authors concluded that not only the pulse energy of lasers but also the passivating layer dramatically affected the re-shaping and melting processes. Cetrimonium bromide (CTAB) as a passivating agent works as an effective heat barrier; it increases and speeds up the photothermal reshaping of gold nanorods. In addition, several groups observed the formation of banana- or sickle-shaped nanoparticles [115,116]. The formation of polycrystalline twins in the particle center was discussed as the likely source of this particle shape, which molecular dynamics simulations also seem to predict [117]. However, the nature of this phenomenon has not yet been explained. Furthermore, the possibility of bending single gold nanorods with laser light while controlling the resulting bending angle of the bent structure has not been realized to date.

This chapter describes a method for the fabrication of V-shaped gold nanoantennas by bending gold nanorods with light. A focused laser beam at a wavelength resonant to their

longitudinal plasmon mode is used to both heat and exert an optical force on individual gold nanorods in a solution. Temperature simulations and HRTEM imaging reveal that the rods melt almost instantaneously as they enter the laser beam, while optical forces simultaneously push the rods in the direction of the propagating light. The molten gold nanorods propagate along the laser beam and experience hydrodynamic interaction with the surrounding water, which results in a bending of the straight rods. The laser power and polarization can control the bending angles and the orientation of the printed antenna structures, respectively.

4.1. Optical manipulation of gold nanorods.

The extinction spectrum of gold nanorods in water measured with the Cary Varian 5000 spectrometer possesses two plasmonic peaks at 515 and 1064 nm, which correspond to transverse and longitudinal plasmon modes (Figure 4.1a). Therefore, optical printing was performed with the usage of a near-infrared laser with a wavelength resonant to the longitudinal plasmon resonance [118]. In chosen conditions, the scattering force acting on the gold nanorods in the laser beam overcomes the gradient force (Chapter 2.1.5), and they are pushed by the laser. SEM investigations revealed that original gold nanorods have a straight shape, and according to statistical analyses of the size distribution, the mean length and thickness are 120±1 nm and 21±1 nm, respectively (Figure 4.1b).

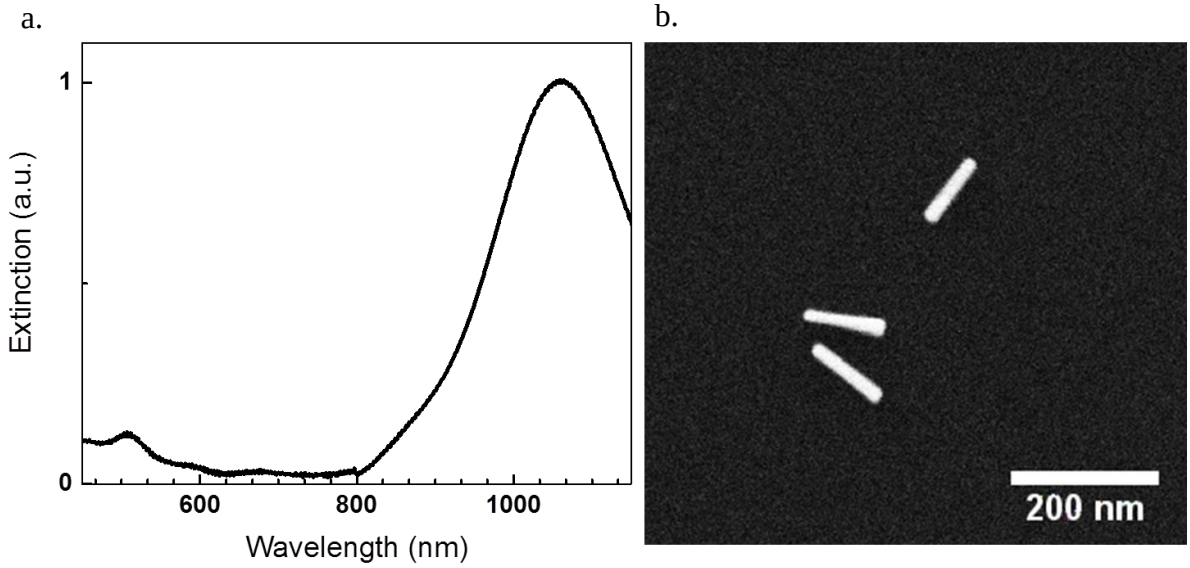

Figure 4.1. Characterization of an original solution of gold nanorods. The extinction spectrum of an ensemble of gold nanorods in water is presented (a). The SEM image of randomly deposited gold nanorods on a glass substrate is provided (b). Reprinted with permission from [118]. Copyright (2016) American Chemical Society.

To investigate the bending process, lines of gold nanorods were optically printed with different laser powers. The laser power was measured directly below the water-immersion objective with a powermeter and then recalculated into laser power densities. In Figure 4.2, SEM images of gold nanorods printed with laser power densities of 0.45 and 0.75 MW/cm^2 are presented. In the case of the lower laser power, gold nanorods were printed on the glass surface with hardly any shape changes. With increasing the laser power, one notices that most gold

nanorods undergo a shape transformation and become bent after optical printing. The experiments were performed on the same day with the same glass substrate and the same solution of gold nanorods.

a. b.

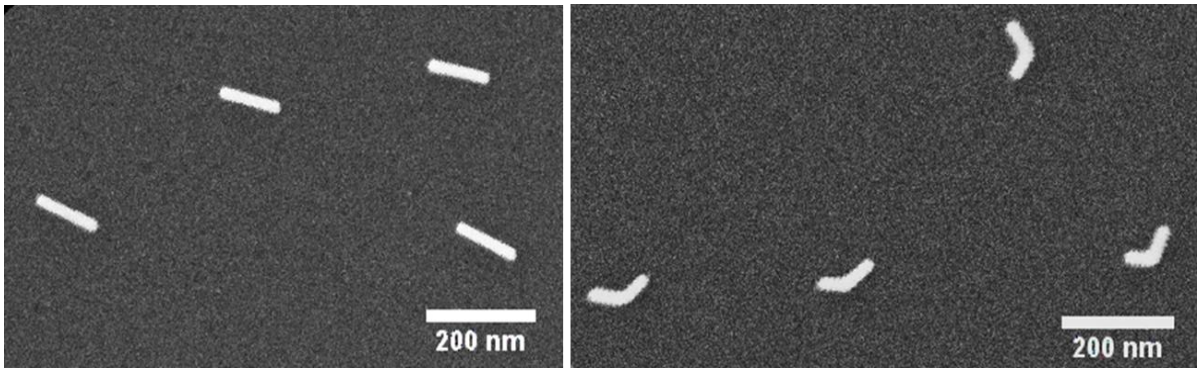

Figure 4.2. Printed straight and bent nanorods. SEM images of printed gold nanorods on glass substrate with laser power density 0.45 MW/cm^2 (a) and 0.75 MW/cm^2 (b).

Optical printing was performed while gradually increasing the laser powers. The changes in the bending angle were subsequently studied. Examples of bent gold nanorods with different bending angles are shown in Figure 4.3.

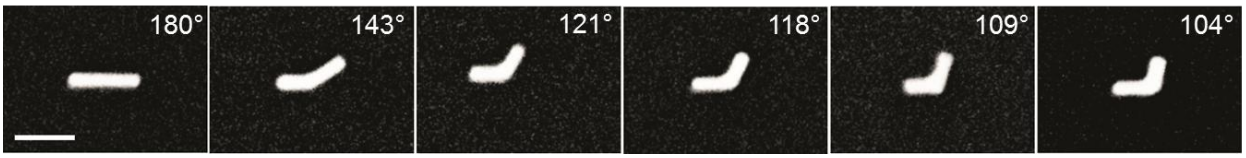

Figure 4.3. Printed gold nanorods with different bending angles. The SEM images of bent gold nanorods with gradual increase in bending angles. The scale bar is 100 nm. Reprinted with permission from [118]. Copyright (2016) American Chemical Society.

The scheme of the printing process is presented in Figure 4.4a. The Gaussian laser beam is focused on the glass surface. Gold nanorods are diffusing in solution (step 1). A single nanorod aligns horizontally as soon as it enters the laser focus (step 2). The nanoparticle is then heated in the laser beam while optical forces simultaneously push it toward the substrate (step 3). Figure 4.4b demonstrates the dependence of the bending angle on the applied laser power density. The bending angle is defined as the angle between the two arms of a gold nanorod. In other words, a 180° opening angle corresponds to a straight nanorod, and a 120° opening angle to a bent structure with an angle between the two arms equal to 120°. With an increase in the printing laser

power, the bending angle gradually increases. By adjusting the laser power, it is possible to control the bending angle in a range from 180° (straight rod) to approximately 110°.

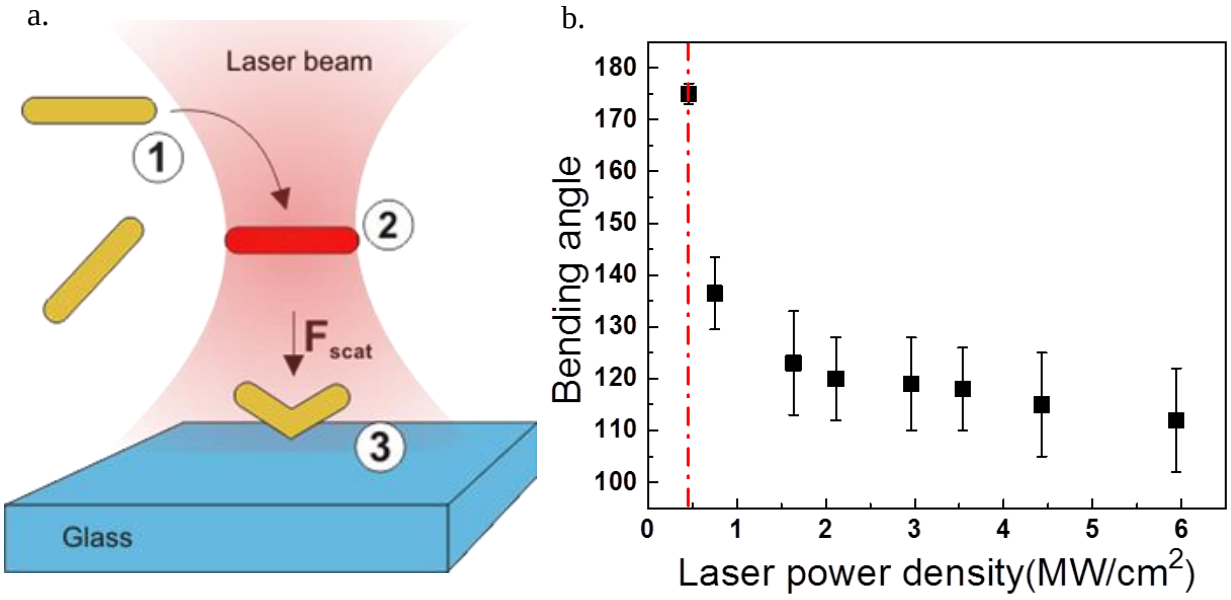

Figure 4.4. Optical printing of gold nanorods: scheme of the experiment and the laser power density and bending dependence. The optical printing process of gold nanorods with a continuous wavelength laser is presented. A gold nanorod first diffuses in water (step 1); when the nanorod enters the laser beam, it is heated, and aligned with respect to linear laser polarization (step 2); and the third gold nanorod is subsequently bent and printed on the glass surface (step 3) (a). The dependence of the bending angle on the applied laser power density is shown. A gradual increase in the applied laser power density leads to an increase in the bending angle (b). Reprinted with permission from [118]. Copyright (2016) American Chemical Society.

The SEM analysis also revealed sub-products of the optical printing process. In Figure 4.5, the ratio between the fractions of differently reshaped gold nanorods is presented. After optical printing with higher laser powers not only straight and bent gold nanorods but also partially or completely molten nanoparticles, ϕ-shaped particles and dimers were observed on the glass substrate. No molten nanoparticles or bent nanorods were found in the original solution of the gold nanorods. The molten shapes started to appear at the printing laser power density of 1.63 MW/cm^2. The ratio of the molten shapes slowly increased with an increasing printing laser power density and reached a maximum value of 20% at the highest laser power density used in this work (5.94 MW/cm^2). Moreover, the ratio between the straight nanorods and bent nanorods did not stay constant and instead changed at different laser power densities. At lower laser power

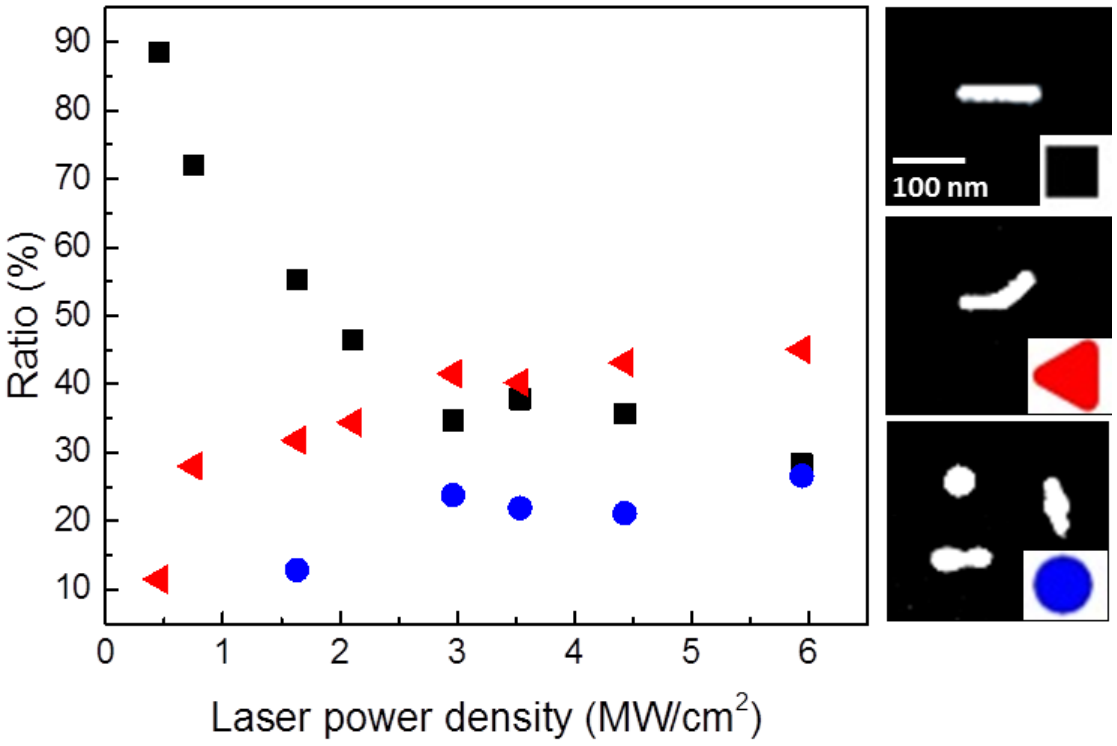

Figure 4.5. Yield of gold nanoparticles shapes. After optical printing with an NIR laser, it was possible to observe straight, bent, molten, and ϕ-shaped particles. The ratio of bent nanorods gradually increases and the ratio of straight nanorods decreases with an increase in laser power density. The SEM images on the right side show straight, bent, and molten nanorods after optical printing. Reprinted with permission from [118]. Copyright (2016) American Chemical Society.

densities, only 10% of all gold nanorods were bent. However, the ratio of bent nanorods increased gradually with an increase in the laser power density, and at 2.96 MW/cm^2, it overcame the ratio of the straight nanorods. With laser power densities higher than 2.96 MW/cm^2, bent nanorods became the main product of the optical printing process.

Statistical analysis of the bending spot showed that the bending primarily occurs in the center of the rod (around 45% of the total length from one of the tips). The statistics are presented in Figure 4.6.

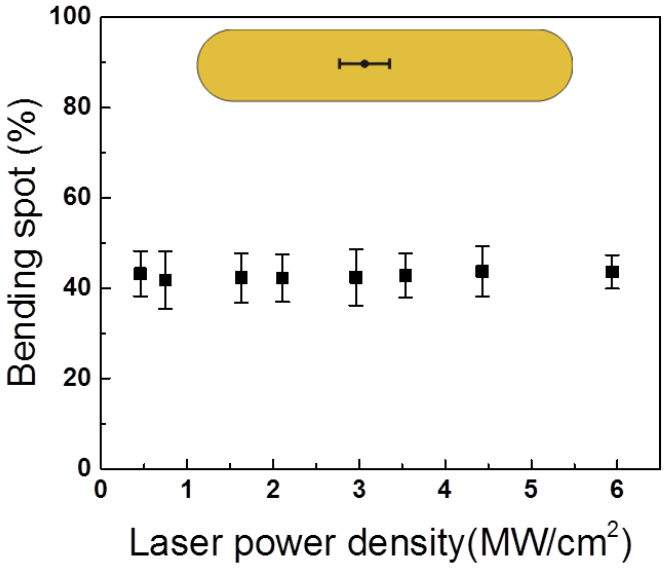

Figure 4.6. Bending point. Dependence of the bending spot on applied laser power density. Statistically, bending happens in the middle of the nanorod within the error bars. Most bending spots are in the region of 10% of the middle of the nanorods. Reprinted with permission from [118]. Copyright (2016) American Chemical Society.

4.2. Optical properties of V-shaped antennas.

Several groups have investigated the optical properties of complex-shape plasmonic structures [97,119,120,121]. Bukasov *et al.* studied the extinction properties of gold nanocrescents [119]. The 2D nanocrescent particles showed transverse and longitudinal peaks, which strongly depend on the total length of the nanocrescents and on the gap between the two tips. Husu *et al.* measured the optical properties of L-shaped antennas [120]. The authors observed higher orders of plasmon oscillations for an array of L-shaped nanoantennas. Kats *et al.* proposed that in V-shaped optical antennas, two eigenmodes of plasmon oscillation exist [121]. The symmetric mode is a plasmon oscillation in the arms of V-shaped antennas (green arrows), and the antisymmetric mode is a plasmon oscillation along the V-shaped antenna (red arrow in Figure 4.7). The calculated scattering spectrum exhibits two plasmon peaks in the shorter wavelength region (symmetric mode) and in the longer wavelength region (antisymmetric mode).

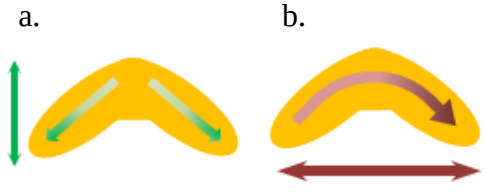

Figure 4.7. Eigenmodes of plasmon propagation in V-shaped antennas. Symmetric (a) and antisymmetric (b) modes in V-shaped antennas. Incident light is polarized parallel (a) and perpendicular (b) to the symmetry axis of the V-shaped antenna.

To study the optical properties of bent nanorods, Rayleigh scattering spectroscopy was performed on single bent gold nanorods with different bending angles. The spectra were recorded on a glass substrate in water. Polarization-dependent spectroscopy allowed to asign the spectral peaks to the different plasmon eigenmodes. In Figure 4.8a, the normalized polarization-dependent scattering spectra of a bent gold nanorod with a bending angle of 104° are presented. The scattering spectra exhibit two plasmonic peaks near 700 nm and 900–1000 nm. When the polarization was oriented parallel to the symmetry axis of the structure, the symmetric mode in the scattering spectrum was observed. Meanwhile, under 90-degree polarization, the symmetric plasmonic peak vanished, and only the antisymmetric peak appeared. The polarization dependence of the symmetric and antisymmetric mode is presented in Figure 4.8b. The original transverse mode of straight gold nanorods is weakly pronounced at 580 nm and is independent of an orientation of polarization. The transversal mode is shifted compared with the transversal mode of the original straight gold nanorods in the ensemble. The shift is observed due to a higher refractive index of a glass substrate compared with a water medium. Meanwhile, the symmetric plasmonic peak appears in the scattering spectra and corresponds to the plasmon oscillation in

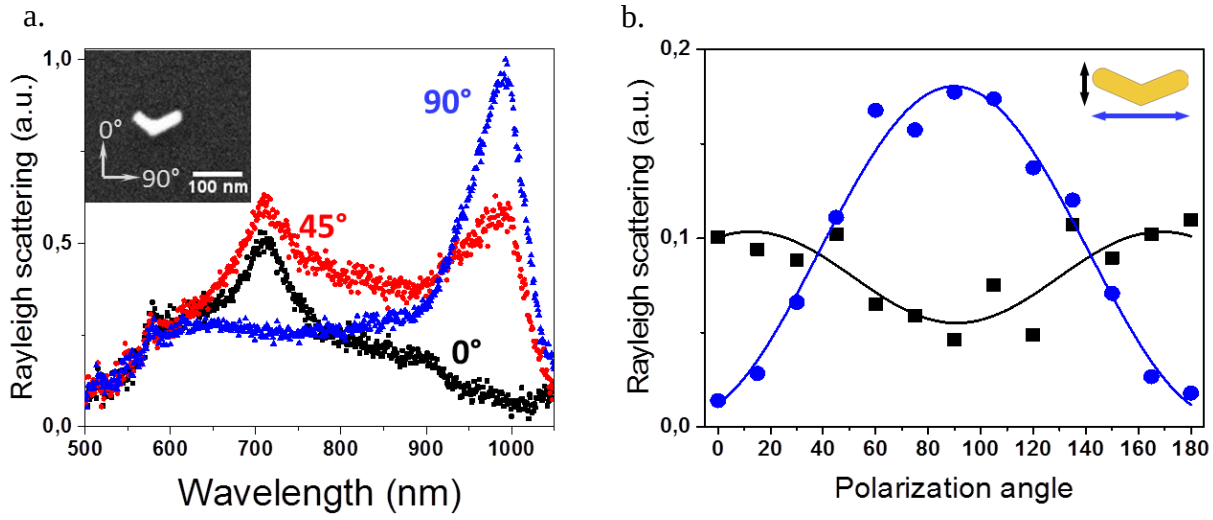

Figure 4.8. Normalized polarization-dependent Rayleigh scattering spectra of V-shaped gold nanoantenna with a bending angle of 104°. A bent gold nanorod exhibits plasmon peaks at 709 nm and 990 nm, which correspond to the symmetric and antisymmetric modes of plasmon propagation in such structures, respectively. The inset shows the SEM image of the examined bent nanorod. The white arrows show the polarization direction (a). The dependence of the two plasmonic peaks on polarized light is shown. The dependences exhibit an inverse character, and the peak intensities recover to their initial values after 180° (b). Reprinted with permission from [118]. Copyright (2016) American Chemical Society.

the arms of bent nanorods. The symmetric plasmonic peak does not shift for different bending angles of gold nanorods and remains constant in contrast to the antisymmetric plasmonic peak. The latter, being located in a longer wavelength region, is shifted to the blue region in comparison with the spectrum of straight gold nanorods. N. Yu *et al.* claimed that the antisymmetric mode of V-shaped antennas corresponds to the plasmon propagation over the whole length of the nanostructure [97]. Therefore, the antisymmetric peak located at 900–1000 nm corresponds to the plasmon propagation along the entire bent structure. The blue shift of the longitudinal plasmon peak is attributed to the reduction of the effective length of the plasmon propagation along the structure.

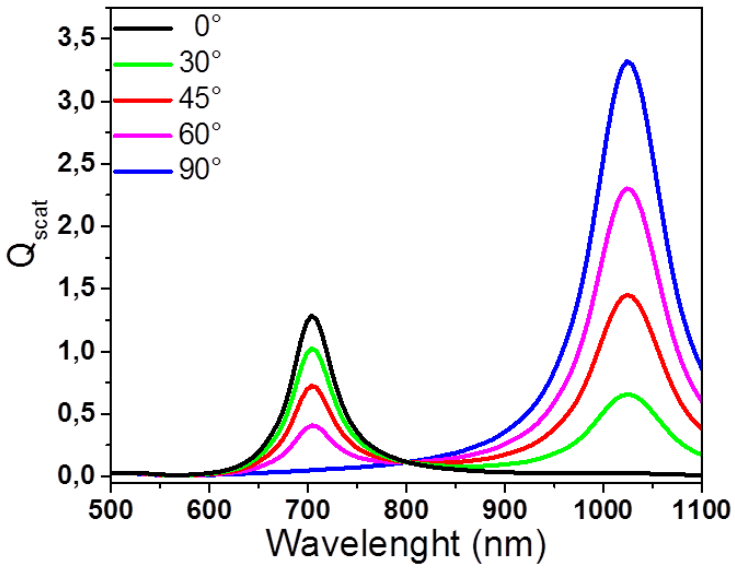

Figure 4.9. The polarization-dependent scattering cross section of a bent gold nanorod calculated with FDTD. Exciting the symmetric mode, the antisymmetric mode, or both modes is possible, depending on the polarization of incident light. Reprinted with permission from [118]. Copyright (2016) American Chemical Society.

The scattering spectra of a bent gold nanorod with a 105° bending angle on a glass substrate and covered with water was calculated using Lumerical FDTD solutions (Figure 4.9).The simulations revealed two plasmonic peaks, which appear at 668 nm and 1034 nm. The incident light polarization was rotated relatively to the axis of symmetry of the bent structure. When the light polarization was oriented parallel to the axis of symmetry, only the symmetric mode was observed in the scattering spectrum. The rotation of the light polarization by 90 degrees (perpendicular to the symmetry axis) leads to the disappearing of the symmetric mode and the appearing of the antisymmetric mode in the scattering spectrum. The scattering spectra simulated in FDTD are in good agreement with the experimental data.

To confirm suggestions about plasmon propagation in bent nanorods, simulations of charge distribution were performed. By plotting the charge distribution at the wavelength indicated above, visualizing the plasmon oscillations in the bent structure was possible. When the polarization is set parallel to the axis of symmetry, the charges accumulate at the nanorod tips and at the bending region, which results in an oscillation of charges in the arms of the bent nanorods. The oscillation of charges in the arms of the bent structure corresponds to the symmetric mode at 668 nm, which is presented in Figure 4.10a. When the polarization of light is rotated by 90 degrees, only the antisymmetric mode is pronounced in the scattering spectrum. A plot of the charge distribution at the resonance wavelength of the antisymmetric plasmon mode shows a higher charge density at the tips and a slightly higher density above the bent spot. The oscillation of charges in a bent nanorod with 90° polarized light happens over the bending region and over the whole length of the structure. The accumulation at the bent spot can be considered an artifact and can be explained with the geometry of a bent nanorod. In the used model, no smoothing objects were used, and the high sharpness of a particular spot led to an artificial spot with a higher charge density. The electromagnetic field enhancement factor is one order of magnitude higher in the case of the antisymmetric mode than in the case of the symmetric mode. When the symmetric mode is excited, all excited charges split between the two arms. For the asymmetric mode, all optically excited charges oscillate over the entire structure; hence, the charge density is higher, which subsequently leads to a higher factor of the electromagnetic field enhancement.

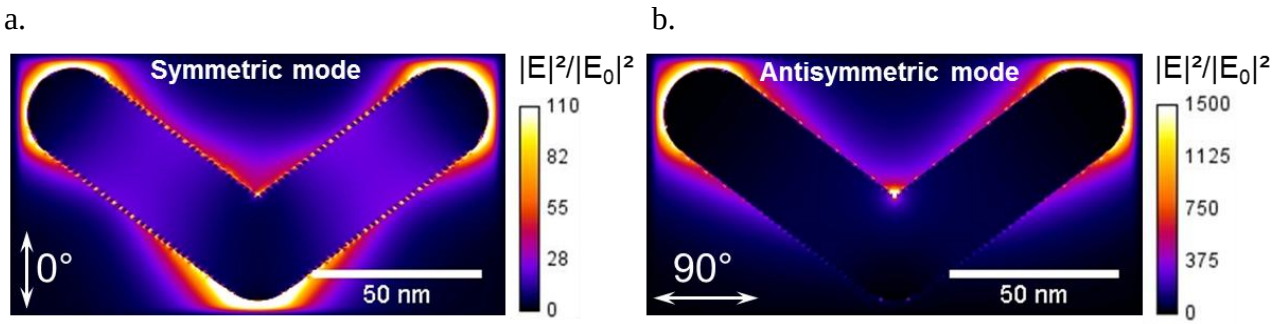

Figure 4.10. FDTD simulations of charge distribution in bent gold nanorods. The charge distribution in bent gold nanorods under external illumination with perpendicular (a) and parallel (b) polarized light (with respect to the long axis of the bent structure). The white arrows represent the polarization of incident light. The colored scale bars present the enhancement factor of the electromagnetic field with respect to the initial incident light. Reprinted with permission from [118]. Copyright (2016) American Chemical Society.

To investigate the influence of the bending angle in the printing process, optical properties of a bent nanorod with an 87° bending angle were investigated. Figure 4.11 shows the Rayleigh scattering spectra of the bent gold nanorod with an 87° bending angle. The symmetric mode appeared at the same wavelength, as the symmetric mode of a bent gold nanorod with a 104° bending angle. The antisymmetric mode, however, had a resonance of 850 nm and was shifted to a blue region compared with the antisymmetric mode of a bent gold nanorod with a 104° bending angle

Figure 4.12 shows the extinction spectrum of straight nanorods in water in an ensemble,

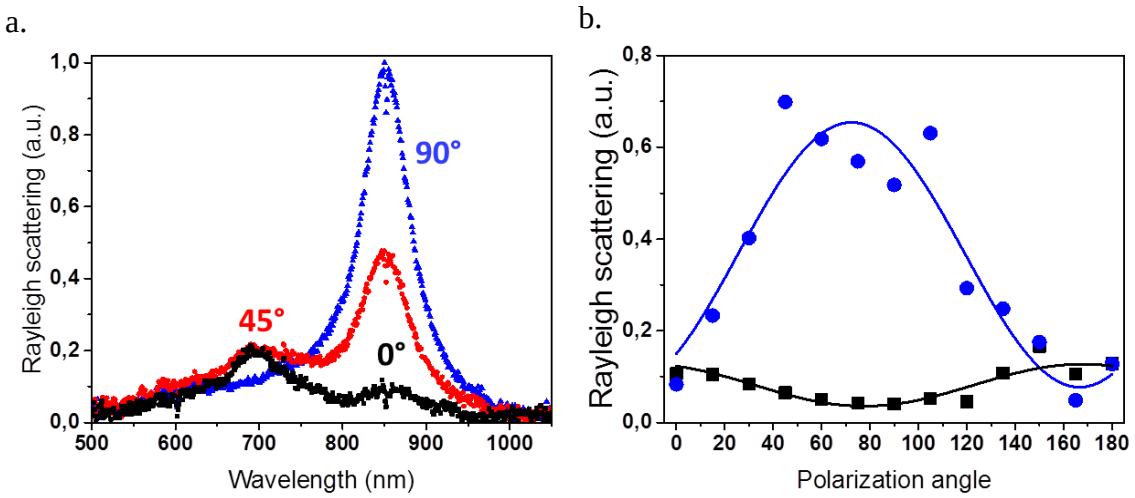

Figure 4.11. Normalized polarization dependent Rayleigh scattering spectra of V-shaped gold nanoantenna with a bending angle of 87°. Spectra were taken on glass substrate and in water. The bent gold nanorod exhibits plasmon peaks at 700 nm and 850 nm (a).The intensity dependence of the two plasmonic peaks on polarization degree is shown. The dependences have the reverse character, and peak's intensities recover to initial values at the same polarization angle (b). Reprinted with permission from [118]. Copyright (2016) American Chemical Society.

and the scattering spectra of bent nanorods with bending angles of 104° and 87° on a glass substrate in water. The symmetric mode appears in the scattering spectra of bent nanorods and is located at wavelengths of around ~700 nm. The symmetric mode does not shift dramatically with an increase in a bending angle. Plasmon propagations in arms (symmetric mode) have almost the same effective length, and hence, the energy of plasmon propagation remains almost constant. However, the antisymmetric mode shifts in the blue region of the spectrum with an increase in the bending angles, e.g., the antisymmetric plasmon resonance in a bent nanorod with bending angle 104° takes place at 1000 nm, and in a bent nanorod with bending angle 87° at 870 nm. This

phenomenon can be explained in terms of the effective length of plasmon propagation in nanorods. When plasmon propagations take place along the whole structure, one can clearly notice a decrease in the effective length of plasmon propagations, which leads to an increase in the energy of plasmon oscillations and to the blue shift of the antisymmetric peak.

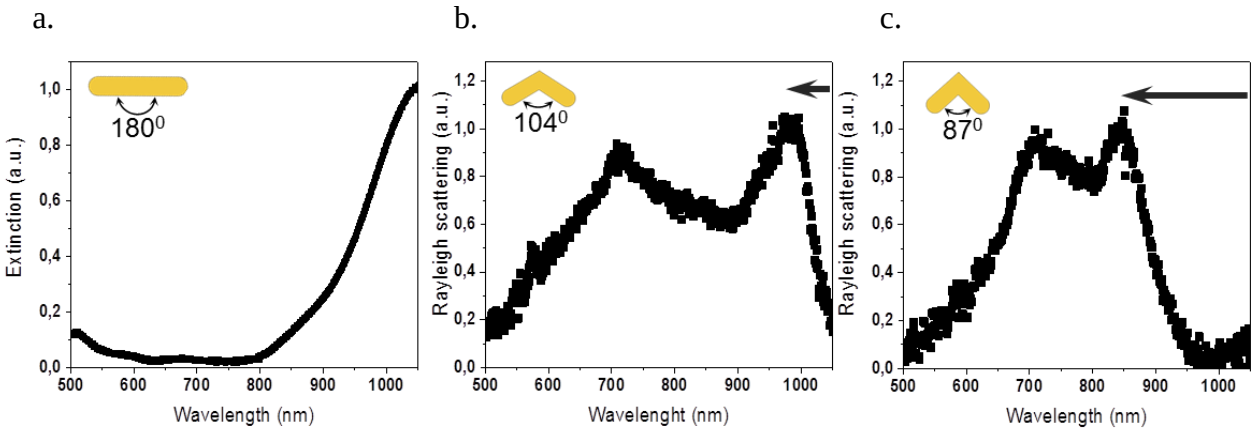

Figure 4.12. The spectra of gold nanorods with different bending angles. The extinction spectrum of gold nanorods in an ensemble (a). The scattering spectrum of the bent gold nanorod with a bending angle of 104° on a glass substrate in water (b). The scattering spectrum of the bent gold nanorod with a bending angle of 87° on a glass in water (c). With an increase in the bending angle, the antisymmetric mode of the plasmon resonance shifts toward the blue region of the spectrum. Reprinted with permission from [118]. Copyright (2016) American Chemical Society.

FDTD simulations confirm the experimental observations. The nanorods were configured in such a way as to have a total length of 124 nm and a thickness of 21 nm, along with bending angles 180° (straight), 150°, 120°, and 90°. The incident illumination with the polarization of zero degrees (parallel to the axis of symmetry) and 90 degrees (perpendicular to the axis of symmetry) was used. In Figure 4.13, the calculated scattering spectra of the bent nanorods with different bending angles with polarization perpendicular (a) and parallel (b) to the longer axis are shown. As discussed earlier and observed in experiments, the antisymmetric mode shifts towards the blue region of the spectrum, whereas the symmetric mode appears at wavelengths ~ 700 nm immediately after bending and does not shift with an increase in the bending angle.

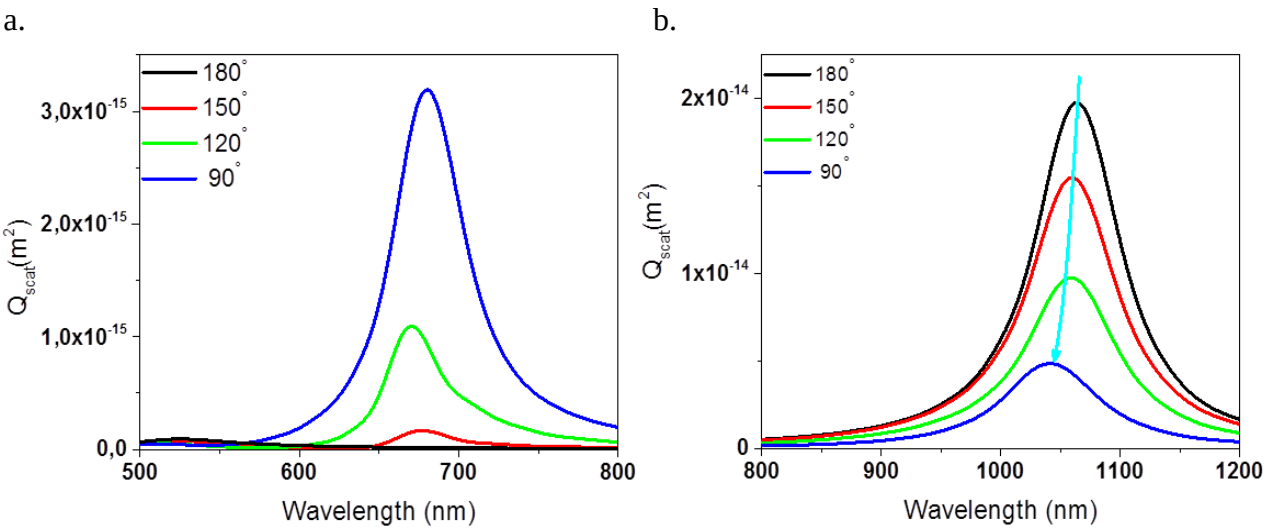

Figure 4.13. Scattering cross section of gold nanorods with different bending angles were simulated in FDTD. The symmetric mode of bent nanorods appears in the red region of the spectrum immediately after bending; however, the symmetric mode does not shift with an increase in bending angle (a). The antisymmetric mode of plasmon oscillation shifts toward the blue region of the spectrum with an increasing bending angle (b). Reprinted with permission from [118]. Copyright (2016) American Chemical Society.

4.3. How does a single gold nanorod bend?

The change of the nanorod geometry is an indication of laser-induced melting. To fully understand the bending mechanism, changes of the crystal structure of the nanorods were examined. HRTEM investigations of the crystal structure of straight, bent, and molten-to-sphere nanorods were performed.

Figure 4.14 shows the HRTEM images of a straight gold nanorod. It displays a high order of crystallinity with almost no visible defects, such as stacks, vacancies, or dislocations, and with no signs of melting or reshaping. The nanorod exhibits two facets {200} and {1-31} corresponding to the crystal zone [310]. It is oriented along the <100> axis.

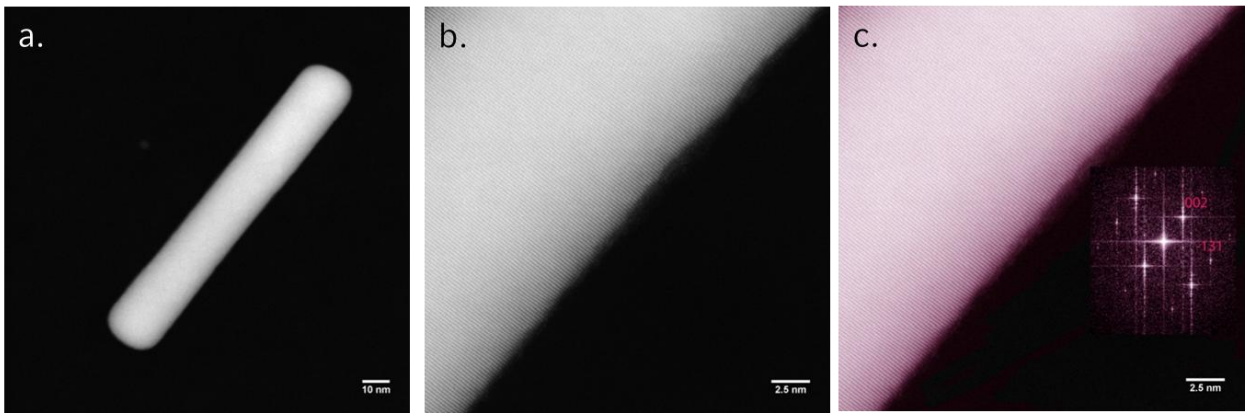

Figure 4.14. HRTEM images of a straight gold nanorod in STEM. HRTEM images of straight gold nanorod with a scale bar of 10 nm (a), 2,5 nm (b,c), and a fast Fourier transform (FFT) analysis of crystal structure (c). The straight nanorod does not contain any visible crystal defects and shows an orientation along <100> axis.

The STEM images of the bent nanorod are show in Figure 4.15. It displays four domains of monocrystallinity that twins have separated. As discussed in Chapter 3.1., one defines crystal twinning as occurring when two parts of crystal domains are oriented relative to each other with a certain symmetry law. The domains display the thermodynamically stable twin grain boundaries along the {111} planes (Figure 4.15). The facet of {111} was reported as a more stable facet in gold nanorods [113,117]. Our observation was in accordance with the reports by Link *et al.*, who showed that the {111} and {100} facets mainly dominated melting gold nanorods. Unstable facets {110} are no longer found in spherical nanoparticles [113,122,123]. Authors have proposed that in a heated gold nanorod, any point-like defect becomes a melting seed. In bent gold nanorods, the appearance of the {111} crystal facet leads to the conclusion

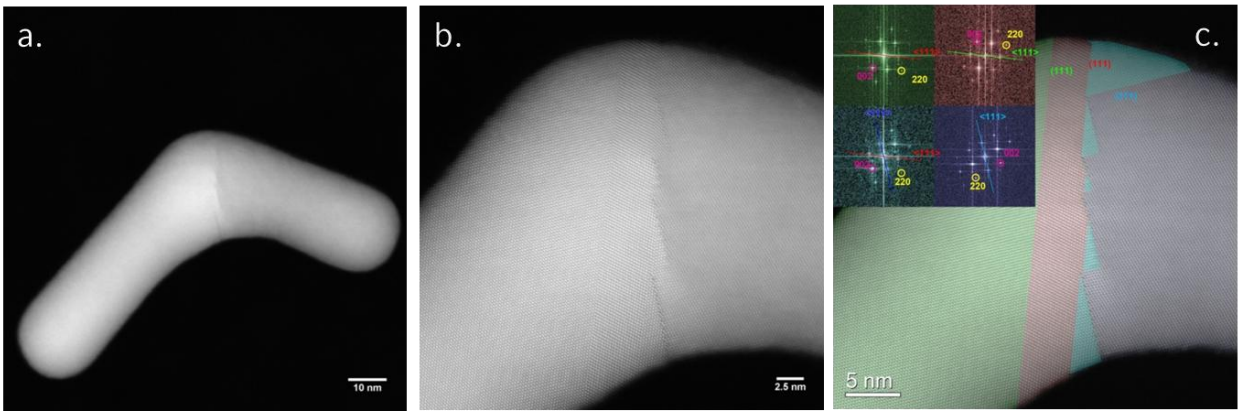

Figure 4.15. HRTEM images of a bent gold nanorod in STEM. Images of a bent gold nanorod with a scale bar of 10 nm (a), 2,5 nm (b,c), and a FFT analysis of crystal structure (c). Bent gold nanorod is elongated along <100> axis. The crystal domains marked in (c) are separated one from another by twin defects formed along {111} plane. Reprinted with permission from [118]. Copyright (2016) American Chemical Society.

that the local melting took place during the optical printing process. Wang *et al.* showed that under heating, the less stable {100} and {110} facets on the surface are substituted by more stable and therefore more energetically favorable {111} planes due to surface-driven bulk reorganization [124]. H. Park et al. performed molecular dynamics simulations of fcc gold nanowires under compression and claimed that deformation in a single fcc lattice is possible due to twin formation along the {111} crystal planes [81]. The bent gold nanorod is elongated parallel to the <100> direction like a straight gold nanorod.

The investigation of molten-to-sphere gold nanorods showed that the molten particle regained its crystallinity, albeit a number of twin defects along the {111} crystal plane remain (Figure 4.16).

As it was already mentioned above, the defects in the crystal structure hint towards a melting process of the gold nanorods. To prove that the gold nanorods reach their melting temperature during optical printing, their steady-state temperatures in the laser beam for specific experimental conditions were calculated.

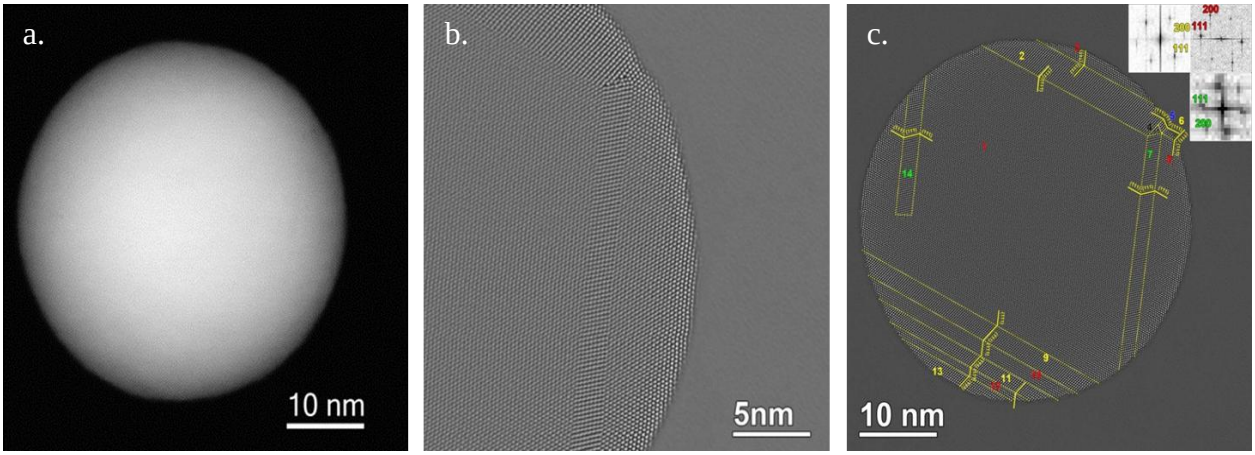

Figure 4.16. HRTEM images of a molten-to-sphere gold nanorod after optical printing. The molten gold sphere with a scale bar 10 nm (a, c) and 5 nm with applied high-pass filter (b). The crystal defects in the molten sphere are illustrated (c). Twin defects along the {111} plane were found. The crystal zone of the molten sphere is [110]. Reprinted with permission from [118]. Copyright (2016) American Chemical Society.

Temperature simulations.

The melting point of bulk gold is 1070°C [125]. Ph. Buffat investigated the size effects on the melting temperature of gold and claimed that the melting point decreases with a reduction in the sizes of gold objects [126]. According to this dependence, and taking into account that the smallest dimension of gold nanorods is the diameter, which is 25 nm, the melting point of gold nanorods used in this work was assumed to be 1070°C.

The heat that plasmonic structures absorb is proportional to the absorption cross section and to the intensity of the incident light (equation 2.23, Chapter 2.1.4, and Chapter 3.2.1). The absorption and scattering cross sections calculated for bent gold nanorods with different bending angles are given in Table 1.

Table 1. Absorption and scattering cross sections of bent gold nanorods with different bending angles at a wavelength of λ=1064 nm.

Bending angle [°]	Absorption cross section [10^{-14} m^2]	Scattering cross section [10^{-14} m^2]
180 (straight)	3.87928	1.9735
150	3.79915	1.5312
120	3.47151	0.961838

Figure 4.13 presents the scattering spectra of bent gold nanorods with different bending angles and demonstrated that with an increasing bending angle, the antisymmetric plasmonic mode shifts into the blue region. In Figure 4.17a, the absorption spectra of bent gold nanorods with different bending angles in the same spectral region are shown. The spectral region between 900 and 1100 nm is illustrated because the laser with a wavelength of 1064 nm was used in this work. The absorption process effectively takes place at this wavelength. The maxima of the absorption cross section shifts towards the blue region with increasing bending angles.

For a straight nanorod, the calculated temperature distribution when irradiated with a focused laser beam with a laser power density of 0.45 MW/cm^2 is presented in Figure 4.17b. According to this, under the smallest applied laser power density, the gold nanorod reaches a temperature of 1150°C, which is above its melting point. Therefore, gold nanorods become soft when entering the laser beam.

Because an increase in laser power density leads to stronger heating, the gold nanorods attain their melting temperature even before reaching the waist of the laser beam. For higher laser power densities, gold nanorods stay molten for a longer period of time while they propagate

a. b.

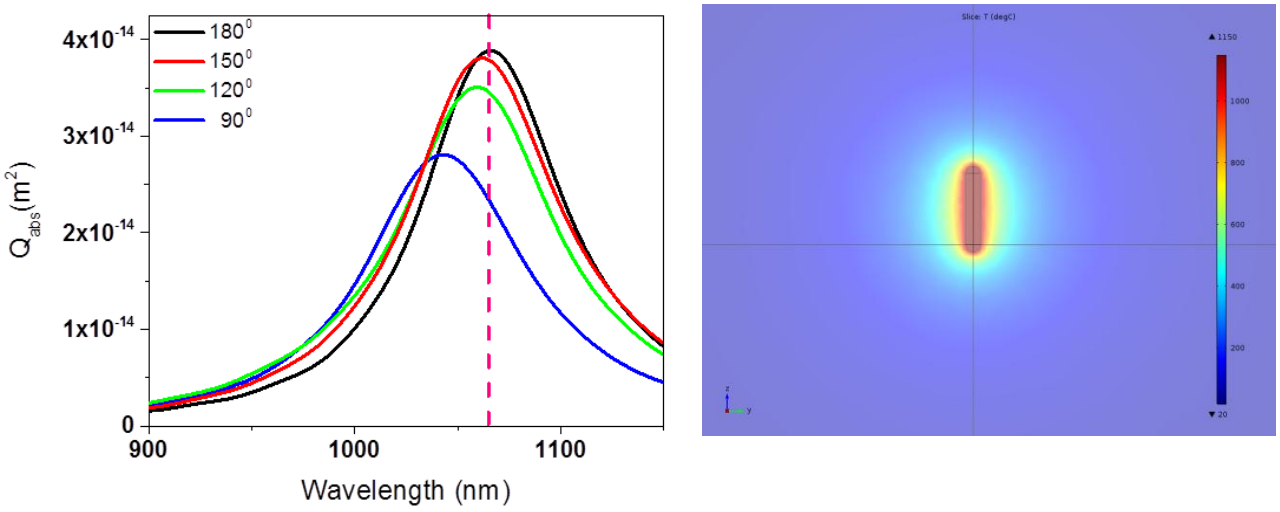

Figure 4.17. Simulated absorption cross sections of bent gold nanorods with four different bending angles. With increasing bending angle, the plasmon resonances shift to the blue region, and hence, the absorption at λ=1064 nm decreases (a). Simulation of the temperature distribution around a gold nanorod with a diameter of 21 nm and a length of 124 nm illuminated with a laser power density of 0.45 MW/cm^2. The surrounding medium is water. The laser beam was focused on the object via a water-immersion objective (NA = 1.0) (b). Reprinted with permission from [118]. Copyright (2016) American Chemical Society.

in the laser beam. According to the absorption spectra presented in Figure 4.17a, the absorption cross sections of bent gold nanorods gradually decrease at the wavelength of 1064 nm with an increase in the bending angle. Therefore, for temperature simulations with higher laser power densities, the absorption cross sections for the bent gold nanorods with pre-defined bending angles have to be used. The distance from the laser waist, where the straight gold nanorods reach their melting temperature, and the position where the bent nanorods with pre-defined opening angles undergo a phase transition from a molten to solid-state condition were calculated. Beforehand, the amount of heat required to reach the melting temperatures for straight and bent nanorods was calculated in COMSOL Multiphysics. The diameter of the laser beam was modeled in such a way as to match the amount of heat required to reach the melting temperature of the gold nanorod. With an increase in the printing laser power density, the distance where the nanorod remains molten in the laser beam increases. When the bending angle is big enough, the absorption cross section is significantly reduced due to the shift of the antisymmetric mode of the plasmon resonance to the blue region. As a results, the bent gold nanorods are not heated sufficiently and freeze out at a certain distance from the focal plane of the laser. At a laser power density of 0.45 MW/cm^2, a straight nanorod is heated above its melting temperature within a range of ±200 nm in z-direction from the laser focus. For 0.75 MW/cm^2, the range is already increased to approximately ± 800nm and to ~ ± 1.5 μm for a laser power density of 2.11 MW/cm^2 (Figure 4.18).

However, the melting or thermally induced re-shaping of the nanorods alone does not provide a sufficient explanation for the observed bending angle dependence on the laser power. To understand and examine the nature of the bending process of gold nanorods during optical printing, the simulations of optical forces acting on gold nanorods during the printing process were performed, and the hydrodynamic pressure that gold nanorods experience during propagation in a laser beam was calculated.

Optical force calculations.

The scattering and absorption cross sections previously calculated were used to calculate the optical forces acting on gold nanorods (straight and bent) in a laser beam. As discussed earlier in Chapter 2.1.5, the scattering force is proportional to the imaginary part of the complex polarizability and hence to the extinction cross section. The gradient force is proportional to the

real part of the complex polarizability of the nanoparticle and thus to the scattering and extinction cross sections.

Using the appropriate absorption and scattering cross sections for bent gold nanorods with

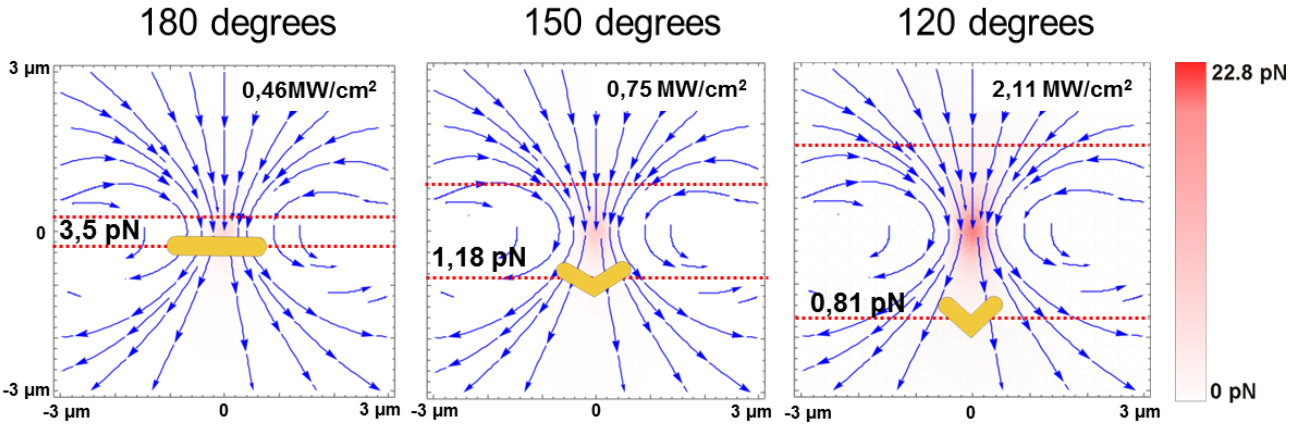

Figure 4.18. Optical forces acting on a bent gold nanorod during optical printing. The scattering forces acting on straight or bent nanorods when they undergo phase transition from molten to solid state. Reprinted with permission from [118]. Copyright (2016) American Chemical Society.

certain bending angles and laser power densities, the scattering force was calculated at the distance from the laser waist, where the gold nanorods undergo a phase transition from molten to solid state. As shown in Figure 4.18a, the scattering force acting on a straight nanorod is 3.5 pN. For a bent nanorod with a bending angle of 150°, it equals 1.18 pN, and for one with a bending angle of 120°, it equals 0.81 pN. Nevertheless, with an increase in the distance from the beam waist and a decrease of the absorption cross section of bent nanorods at 1064 nm, the scattering force is still high enough to print the nanorod.

Hydrodynamic interactions.

The formation of twin defects confirms that gold nanorods reach a molten or soft state. Temperature calculations confirm that gold nanorods reach their melting temperature at a laser power density of 0.45 MW/cm^2 and that the scattering forces are high enough to print the particles. However, it does not fully explain the dependence of the bending angle on the laser power. To understand in depth the nature of the nanorod bending, hydrodynamic interactions have to be taken into account. In previous studies, Manghi *et al.* discussed the hydrodynamic effects that can take place in soft driven matter in non-equilibrium situations [127]. Particularly,

the authors discussed the hydrodynamics of an elastic charged rod with a length of 380 nm and a thickness of 20 nm in the low Reynolds regime and under external forces. The authors demonstrated that hydrodynamic effects can lead to the bending of elastic rods. Besides, S. Mazur *et al.* theoretically predicted the bending of deoxyribonucleic acid (DNA) fragments in strong electric fields [128]. C. Elvingson studied the bending of a DNA strain and changes in the distance between the two ends of a strain in an electric field by taking hydrodynamic interactions into account. In the same electric field without and with hydrodynamic interactions, the distance between the two ends of the DNA strain stayed constant or was significantly reduced, respectively. With an increase of the electric field, the hydrodynamic interactions affected the DNA strain to a higher degree [129]. By reducing the distance between the two ends of the DNA strain, the authors proved the bending of the charged DNA.

A gold nanorod aligns perpendicularly to the Poynting vector when it diffuses into the laser beam. In this position, the optical forces push the rod in the direction of beam propagation. This causes hydrodynamic pressure on the rod, which works in the opposite direction of its movement [127]. Therefore, during optical printing, soft gold nanorods will experience the influence of a laminar flow directed perpendicular to the long axis. The Navier-Stokes equations for a gold nanorod with a length of 124 nm and a diameter of 21 nm exposed to a laminar flow with a speed of 0.02 m/s were solved using COMSOL Multiphysics (Chapter 3.2.4).

The distribution of the hydrodynamic pressure along a gold nanorod (Figure 4.19a) is

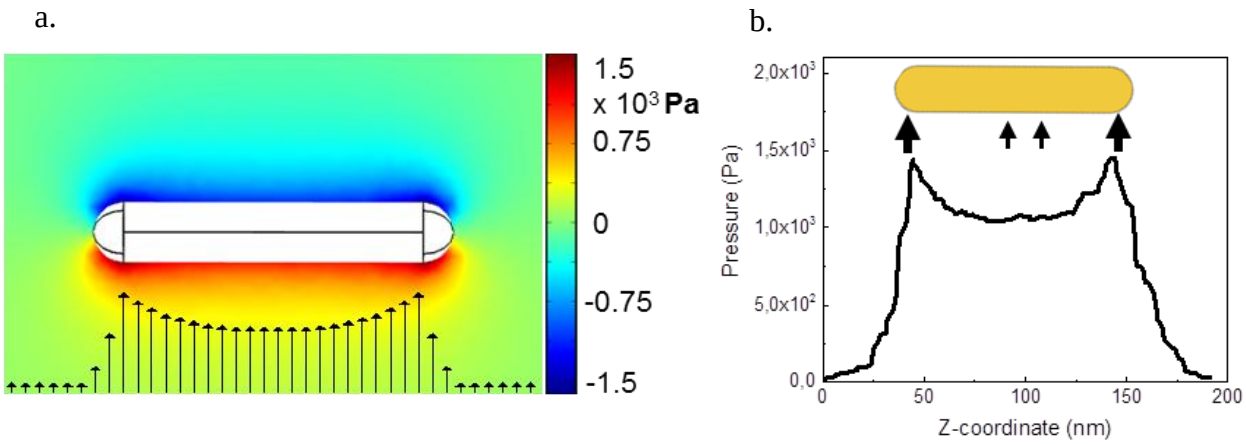

Figure 4.19. Simulation of the hydrodynamic pressure acting on a gold nanorod during propagation in a laser beam. Distribution of hydrodynamic pressure along the long axis of a gold nanorod for stationary laminar flow with a flow speed of 1m/s (a). The pressure distribution at 1 nm away from the gold nanorod surface (b). One can clearly notice that the hydrodynamics pressure is higher at the tips of the gold nanorod. Reprinted with permission from [118]. Copyright (2016) American Chemical Society.

plotted. In Figure 4.19b, the pressure at a distance of 1 nm from the surface of the gold nanorod is shown. A higher hydrodynamic pressure (~30%) is observed at the tips of the gold nanorods. Assuming that the heated rods are soft and deformable, this additional hydrodynamic pressure difference leads to a symmetric deformation of the linear structure. To reduce the friction and hydrodynamic pressure difference, the molten soft nanorod tends to bend.

Overall, the degree of nanorod bending observed for different laser intensities is a result of an interplay of both the hydrodynamic pressure acting on the rod and the change of the optical properties with increasing nanorod deformation. The nanorods are continuously heated and pushed while interacting with the laser beam. The continuous melting and particle movement combined with hydrodynamic interactions allow for nanorod reshaping.

4.4. Positioning of V-shaped antennas.

In the past decade, researches paid huge attention to the design of new optical metasurfaces, which might substitute traditional optical components for light manipulation [94,97,130,131,132]. Metasurfaces, also known as "flat optics", are common tools for the manipulation of light properties, such as amplitude, phase, and polarization [94,97]. One of the most prominent examples of flat optics is plasmonic metasurfaces consisting of a periodically arranged array of V-shaped nanoantennas with custom engineered geometrical parameters. They made it possible to achieve a phase shift between incident and scattered light over the entire 2π range [97]. The design and fabrication of metasurfaces based on arranged V-shaped antennas requires the positioning of individual optical antennas with controlled lateral spacing (smaller than the wavelength of incident light), orientation, and an opening angle on a flat substrate. V-shaped antennas fabricated by using e-beam lithography are applicable only in the NIR and mid-infrared region due to their relatively large sizes. To fabricate such metasurfaces in the visible range, the sizes of the V-shaped nanoantennas have to be decreased.

The precise arrangement of bent nanorods on a glass substrate is a subject of discussion. It was mentioned in Chapter 4.3 that during the optical printing process, gold nanorods orient in the laser beam in such a way that they align parallel with the linear polarization of the laser [127]. In other words, gold nanorods, both straight and bent, will be printed with a preferential orientation on top of the glass substrate. A statistical analysis of the gold nanorods' orientation after printing relative to the laser polarization was performed and is presented in Figure 4.20a. Straight gold nanorods printed with the lowest laser power exhibit a preference in orientation. It was possible to orient straight gold nanorods with a standard deviation of 26° with respect to the laser polarization. For bent nanorods, one can also see a preferential orientation if only the long axis of the bent structure is considered. Bent gold nanorods were printed on the glass surface with a standard deviation between 20° and 30°. The nanorods bent during their movement along the propagating light beam touched the substrate at first with the tip and subsequently fell over to one side of the substrate. The orientation of the opening angle was thus distributed equally to both sides of the antenna's long axis.

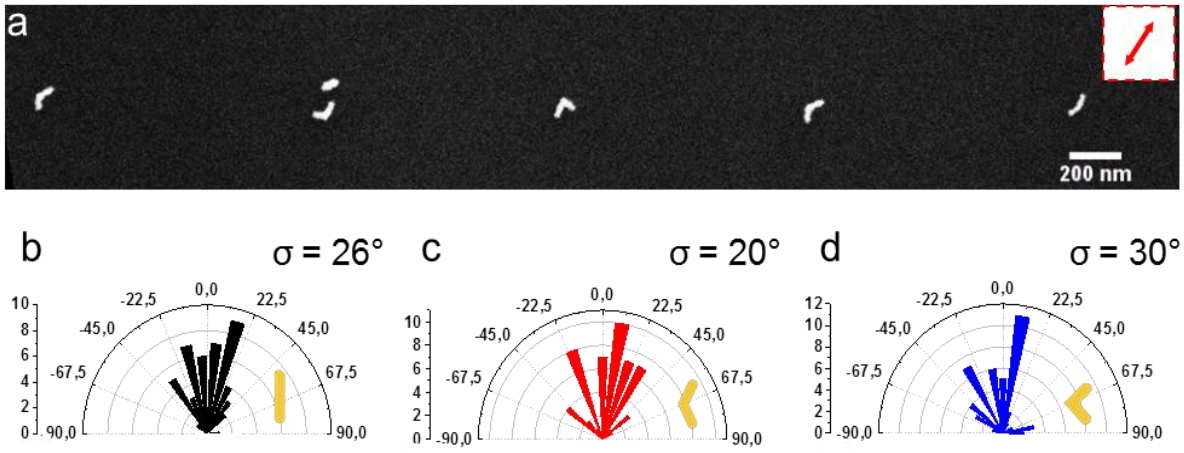

Figure 4.20. Orientation control during optical printing with a linear polarized laser. SEM image of a line of five optically printed, V-shaped nanorods (a). Statistical analysis of the nanorod orientation with respect to the laser polarization (b-d). The '0,0' direction (red arrow) shows the polarization of the laser beam. The data for 50 nanoparticles was measured for each histogram. Angular standard deviation of straight nanorod printed with polarized light (b). Angular standard deviation of bent nanorod with opening angle of 136°(c), and angular standard deviation of bent nanorod with opening angle of 118°(d). Reprinted with permission from [118]. Copyright (2016) American Chemical Society.

4.5. Summary

The possibility of bending gold nanorods and simultaneously positioning and aligning them on a flat substrate using a resonant *cw* laser was demonstrated. The amount of heat, the optical force, and the polarization of the laser beam control the degree of bending and the alignment on the substrate of each individual V-shaped antenna.

A gradual increase in the printing laser power leads to the transformation of gold nanorods from a straight to a bent shape. The bent structures in this study were observed for laser power densities greater than 0.45 MW/cm^2, which is sufficient for heating the particles above the melting temperature of gold. A gold nanorod aligned perpendicular to the light propagation direction is subject to hydrodynamic interactions with the surrounding water. The calculated distribution of the hydrodynamic pressure along the long axis of the gold nanorod indicates that the pressure is almost 30% stronger at the tips compared to the center. Assuming that the heated rods are to some degree soft and deformable, this pressure difference leads to a symmetric deformation of the linear structure.

The bent nanorods display two plasmon resonances at ~700 nm and ~1000 nm that correspond to a symmetric and an antisymmetric modes with respect to the symmetry axis of the structure. The symmetric mode does not experience a strong shift with an increase in the bending angle. The antisymmetric plasmonic peak was found to be shifted to the blue region due to a reduction of the effective dipole length of the plasmon propagation. A blue shift of the antisymmetric mode with an increase in the bending angle leads to a decrease in the absorption and scattering cross sections at 1064 nm, associated with less heating and weaker optical forces. The STEM studies of bent structures revealed twin domains that are formed in the bending region. The domains display the thermodynamically stable twin grain boundaries along the {111} planes.

All in all, the dependence of the bending angles of bent nanorods on laser power densities is a consequence of an interplay between the hydrodynamic pressure and the changes of the optical properties with increasing nanorod deformation.

This new approach renders it possible to generate arrays of bent or V-shaped nanoantennas and to assemble them in a controlled orientation on top of a solid substrate, which holds great potential for the fabrication of flat optics and metasurfaces in the future. Yu *et al.* in 2011 introduced one of the most well-known examples of V-shaped antennas used as metasurfaces

[97]. In their work, it was shown that precisely arranged V-shaped antennas with defined opening angle are capable of modulating the shape of a laser beam and creating vortex beams (Figure 4.21).

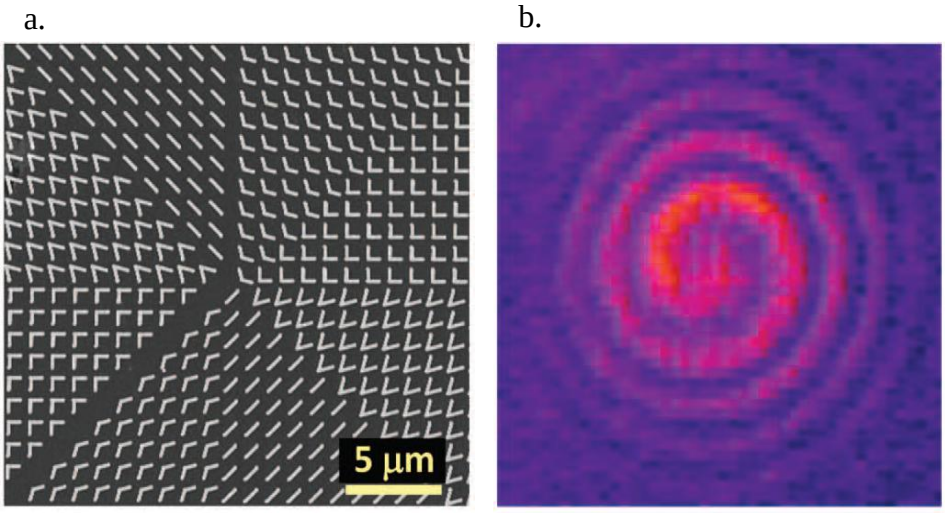

Figure 4.21. Optical metamaterials based on V-shaped antennas. The SEM image of precisely arranged V-shaped antennas, fabricated by using e-beam lithography (a). The measured pattern created by the vortex beam passing through metasurfaces and co-propagating Gaussian beam (b). From [97]. Reprinted with permission from AAAS.

To improve the control over the orientation and positioning of the bent nanorods, the modification of the shape of the laser beam or the tilting of the substrate on one side can be implemented. These strategies will likely allow one to gain better control over the angle distribution.

5. Plasmonic nanoantenna structures for near-field trapping.

In Chapter 2.1.5, it was discussed that optical manipulations of objects with sizes smaller than the laser wavelength take place in the Rayleigh regime. In the Rayleigh regime, the optical forces exerted on objects originate from the interaction between the laser beam and the induced dipoles of investigated objects. The last term is determined based on the polarizability of the objects used. Metallic nanoparticles possess a high polarizability; therefore, the optical forces reach substantial values to perform stable optical trapping. Because non-metallic objects of nanometer sizes, e.g., biological species, have lower polarizabilities than metallic nanoparticles do, the optical forces do not overcome thermal fluctuations [133]. Higher laser power densities, which are required for the stable optical trapping of biological objects a few hundred nanometers in size, can destroy biological species. Hence, the optical trapping of non-metallic objects, like such as viruses, quantum dots, or molecules, remains a challenging task. Near-field trapping with the assistance of plasmonic nanoantennas has emerged as an alternative technique to perform optical manipulations of such objects. The capability of locating and enhancing light in the vicinity of surfaces remarkably improves the trapping and manipulating of non-metallic objects without damaging them [134].

It was shown for the first time that plasmonic nanopads assist the trapping of polystyrene spheres with diameters of 200 nm [135]. The displacement of polystyrene spheres in a trap located between the nanopads was dramatically reduced compared with the displacement of polystyrene particles in an optical trap. Polystyrene particles of larger sizes (around 500 nm) have been successfully trapped optically with plasmonic substrates consisting of nanopillars [136] and bow-tie plasmonic nanostructures [53]. The enhancement factors reached values of 20 and 200, respectively. The trapping of particles with diameters of 100 nm by one nanopillar [137], four nanopillars [137], double nanopyramids [138], and double nanoblocks [139] has been reported.

Later on, the trapping of 12 nm silica particles, 20 nm polystyrene particles [140], and bovine serum albumin protein [141] with double nanohole structures was reported. The complex geometry of the plasmonic antenna structures mentioned above was achieved by using high-end nanofabrication methods, such as electron-beam lithography, ion-beam lithography, and electron-beam lithography [53,139]. Furthermore, all near-field trapping experiments of particles

and molecules were performed for individual objects. To perform near-field trapping experiments in an ensemble, large arrays of plasmonic nanoantennas are required. For producing large arrays of plasmonic nanoantennas with the desired parameters, these techniques are inappropriate due to their high costs and long procedure times. Shoji *et.al.* demonstrated the possibility of producing larger arrays of gold nano-pyramidal-dimers with the use of angular-resolved nanosphere lithography (AR-NSL) and of reversibly trapping DNA chains between the tip and side of pyramidal dimers [142]. The geometry of the plasmonic substrates makes it complicated to control the distance between plasmonic nanoantennas and to create spots of strong electromagnetic field enhancement. Plasmonic nanoantennas made of nanotriangles with tips directed toward each other are able to overcome these drawbacks. Colloidal lithography, on the other hand, enables one to fabricate a large area of plasmonic nanoantennas [143]. Such a technique provides the possibility of establishing the near-field trapping of nanoparticles in an ensemble, which will be discussed later.

Chapter 5 describes colloidal lithography as a fabrication method of the micro-nanopatterned surfaces of plasmonic nanoantenna for the near-field trapping of low-refractive index nanoparticles in an ensemble and ways of controlling the optical and geometrical properties of nanoantenna arrays in a wide range. Shadowing masks were applied on top of these arrays of polystyrene beads to form a micro-nanopatterned surface over an area of several cm^2. The dependence of laser power densities required to achieve the stable near-field trapping of silica beads with different sizes on plasmonic nanogap antennas was discussed.

The possibility of delivering single nanoparticles, such as gold nanoparticles or nanodiamonds directly into individual plasmonic “hot spots” by a combination of optical tweezers and electromagnetic field enhancement was demonstrated. Vapour bubble formation due to the overheating of the surrounding solvent on plasmonic nanoantennas was investigated as well.

5.1. Creating micro-nanostructures by colloidal lithography.

Grober *et al.* suggested the possibility of using plasmonic nanostructures for local electromagnetic field enhancement [144]. The authors predicted the possibility of concentrating microwaves in a small volume with aluminum nanoantennas. Later, plasmonic nanoantennas were developed for the visible range of the spectrum [145]. Fromm *et al.* discussed the dependence of the plasmon peak on the gap distance between the tips of nanoantennas and on the polarization of the incident light [145]. Nowadays, such nanostructures are mainly fabricated by using e-beam lithography [53,145,146]. Here, an alternative bottom-up approach for producing large (24*24 mm) arrays of plasmonic bow-tie nanoantennas is presented. The general approach of this type of bottom-up lithography is described elsewhere [149,147,148].

The main steps of this approach can be listed as follows. A layer of polystyrene spheres are deposited on the surface of a glass substrate be it either spin-coating [149] or the Langmuir-Blodgett technique [150,151]. Here, a hexagonally closed layer of polystyrene beads was formed on the glass surface. In a second step, air plasma was used to etch the polystyrene beads (Figure 5.1a, step 1). During plasma etching, polystyrene beads start to melt [152]. Attractive capillary forces between neighboring molten beads induce the formation of bridges between beads (Figure 5.1a, step 2) [152]. In a third step, bigger structures can be created by putting micro-masks on top of polystyrene beads. Mask protection assists the formation of sharp edges between the nanoantenna array and the glass area. Micro-nanopatterned surfaces facilitate the tracking of the exact location on plasmonic nanoantennas and the examination of the near-field trapping efficiency of nano-objects by using an SEM. In the last step, gold was evaporated on top of the polystyrene sphere array with an average rate of 3 $Å s^{-1}$ with an Edwards Auto 306 Turbo evaporator at an average pressure of 10^{-6} mbar. Here, the average layer thickness was 30 nm. A schematic illustration of the fabrication approach discussed above is given in Figure 5.1a.

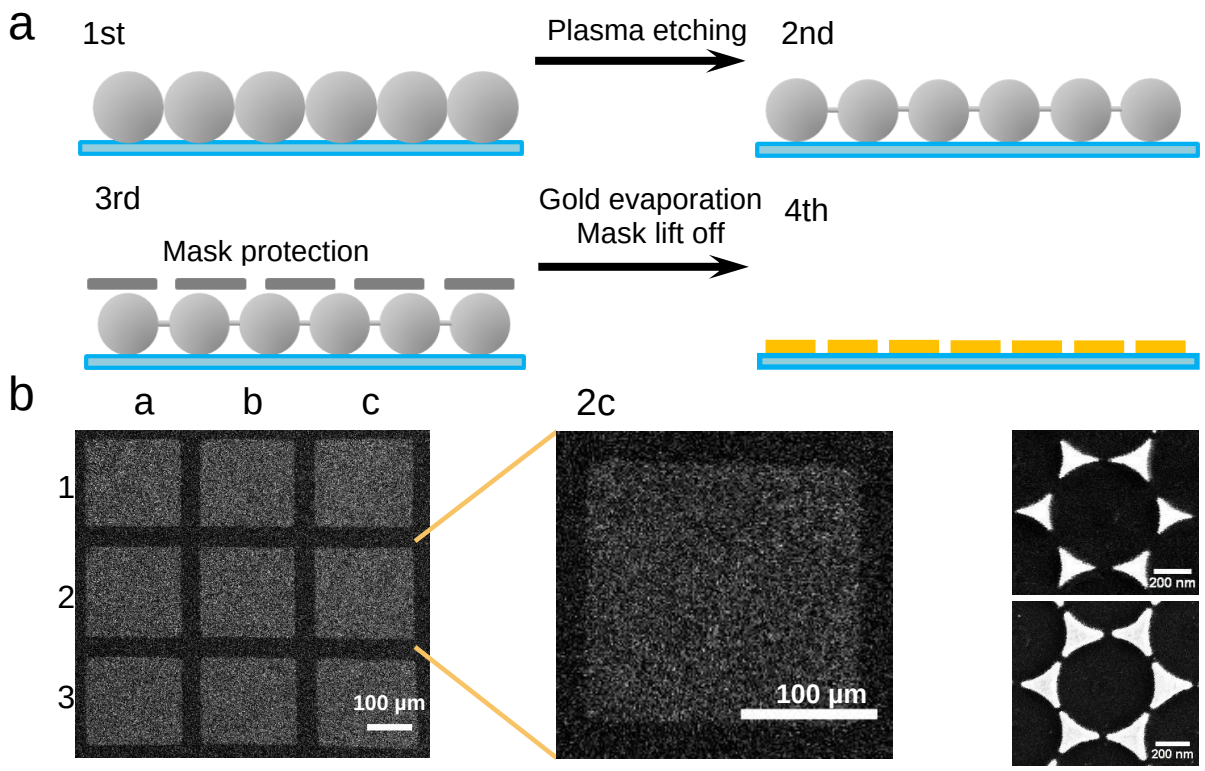

Figure 5.1. Fabrication process of plasmonic nanotriangles. A hexagonal layer of polystyrene beads on the substrate was formed by colloidal lithography (first step, a). The substrate was treated with air plasma to control the gaps between the tips of the nanoantennas (second step, a). A metallic mask shielded parts of the array of polystyrene beads, and a 30-nm Au layer was evaporated on top (third step, a). Finally, the masks were lifted off (fourth step, a). Micro-nano patterning allows for forming sharp borders between the glass surface and plasmonic nanoantenna array, and it assists in labeling and detecting certain spots on the substrate (b). An increase in plasma etching time leads to stronger melting of polystyrene beads, which results in a decrease in gap sizes and an increase in nanoantenna side length. SEM images show the final structures without plasma treatment and after 90 s of plasma treatment (b).

Control of optical properties of plasmonic nanoantenna structures.

The possibility of controlling and adjusting the optical properties of plasmonic nanoantennas allows one to use them in various applications. By choosing appropriate sizes of polystyrene beads, it is possible to tune the plasmon resonance of the plasmonic structure from the visible range to the NIR region. Subsequent air plasma treatment adjusts the precise position of the optical response. Using polystyrene spheres with larger sizes shifts the plasmon resonance of the structure toward the NIR region. In Figure 5.2, the extinction spectra of plasmonic bow-tie

structures fabricated with polystyrene spheres of different sizes are shown. Polystyrene spheres with 477-nm, 607-nm, and 756-nm diameters were used. The plasmon resonance of such structures shifts by more than 250 nm into the NIR region. The differences in the polystyrene bead sizes yield differences in nanotriangles lengths. Fisher *et al.* claimed that the resonance peak of bow-tie nanoantennas shifts in the NIR region with an increase in the antenna length [54].

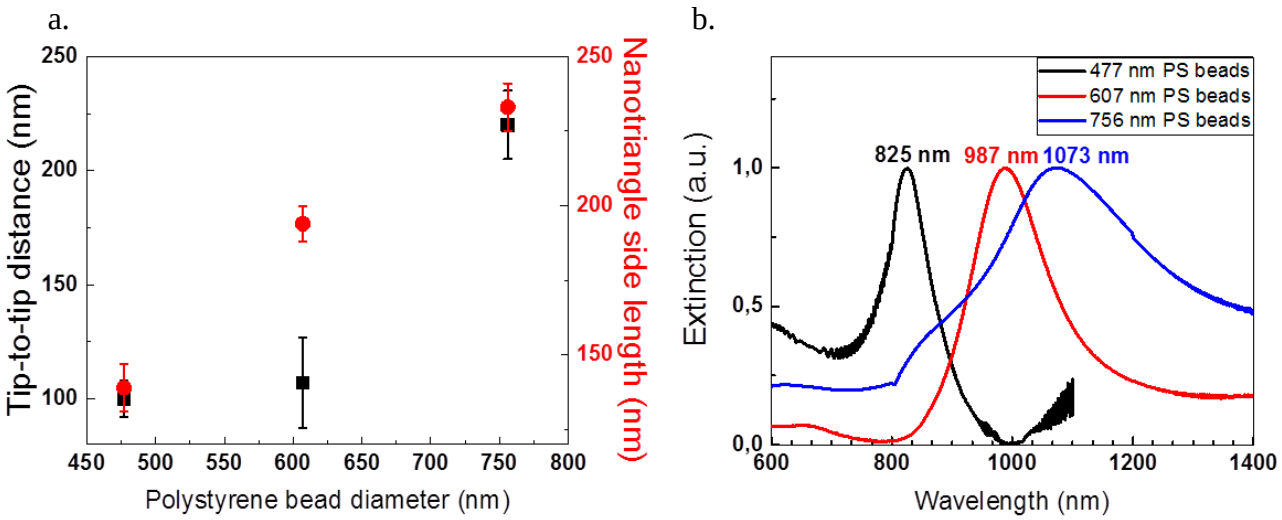

Figure 5.2. Characterization of plasmonic nanoantennas scaffold fabricated with different polystyrene bead diameters. The dependence of the gap size (black squares) and of nanoantenna side length (red circles) on the diameter of used polystyrene beads (a). Extinction spectra of plasmonic bow-tie nanoantennas fabricated with polystyrene spheres of different diameters (b). Using polystyrene spheres with larger diameters results in an increase in the nanoantenna side length and gap size, which consequently shifts the plasmon resonance into the low-energy region of the spectrum.

Despite the fact that no air plasma treatment was applied on these substrates, gap distances between the tips in all three cases are not the same. The mean gap distance between the tips decreases gradually with a decrease in the polystyrene bead diameter. Using polystyrene beads with different diameters leads to significant changes in the side length of the nanoantennas, which affect the wavelength of the plasmon resonance. Therefore, by using smaller or larger polystyrene spheres, it is possible to shift the plasmon resonance to higher or lower energies, respectively.

Fischer *et al*. proposed that the gap size does not affect optical properties but only the near-field enhancement [147]. However, the gap size is responsible for coupling between neighboring

plasmonic nanoantennas. With a decrease in the gap size, stronger coupling between nanoantennas takes place, and therefore, stronger electromagnetic field enhancement occurs between the tips. The plasmon peaks of nanoantenna substrates shift to the NIR with smaller gap sizes and large nanoantenna sizes (Figure 5.3). When longer plasma etching is applied, it is possible to reduce the gap sizes down to 12 nm; however, many plasmonic nanoantennas are interconnected at the tips. In near-field trapping experiments, an NIR laser with a wavelength 1064 nm was used. Therefore, plasmonic nanoantenna substrates with a 70-nm gap size perfectly match the laser wavelength as shown in Figure 5.3b.

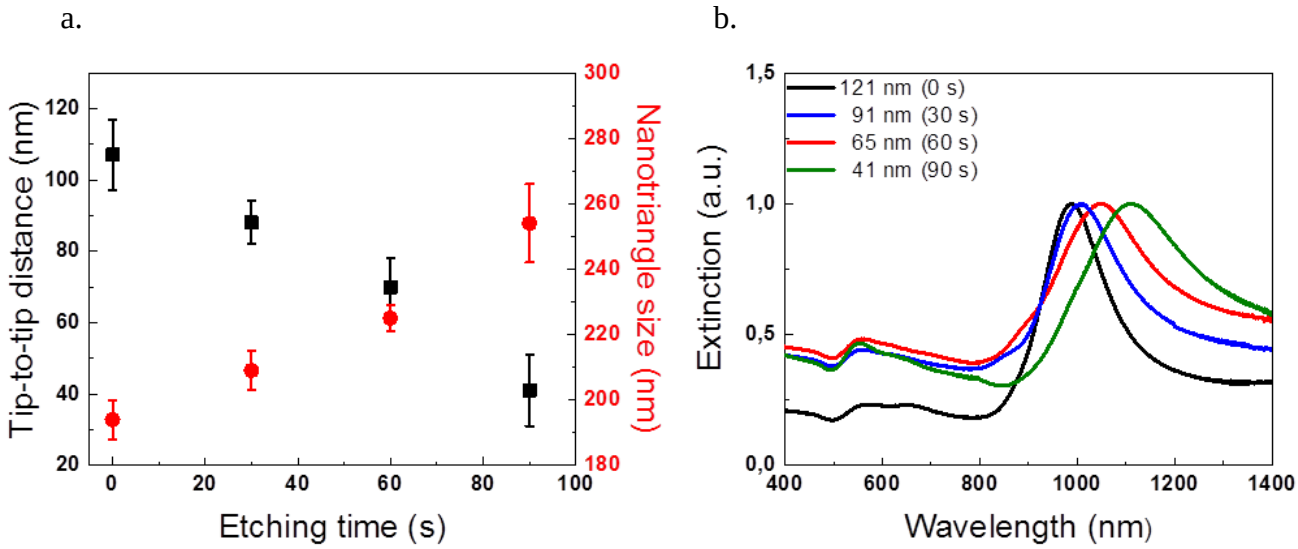

Figure 5.3. Characterization of plasmonic nanoantennas with different plasma treatment time. The dependence of the tip-to-tip distance (black squares) and the dependence of nanoantenna side length (red circles) on the etching time (a). The extinction spectra of plasmonic nanoantennas with different geometrical parameters (b). A longer plasma etching time leads to an increase in the nanotriangle side length, a decrease in the tip-to-tip distance, and a shift in the longitudinal plasmon resonance to the longer wavelength region.

Control over near-field enhancement of plasmonic nanoantenna structures.

Smaller gap sizes lead to stronger coupling between nanoantennas [147] and hence to a stronger near-field enhancement [39]. In Figure 5.4, the electromagnetic field enhancement simulated with FDTD is presented. Simulations of gold nanoantenna pairs with varying sizes (the thickness of the gold nanoantennas was 30 nm, side lengths were 145 nm, 166 nm, and 196 nm) and tip distances (130 nm, 93 nm, and 46 nm) on a glass substrate in water were carried out

using Lumerical FDTD solutions. According to simulations, one can expect a field enhancement up to 10^3 at the tips in the configuration with the smallest gap size (Figure 5.4).

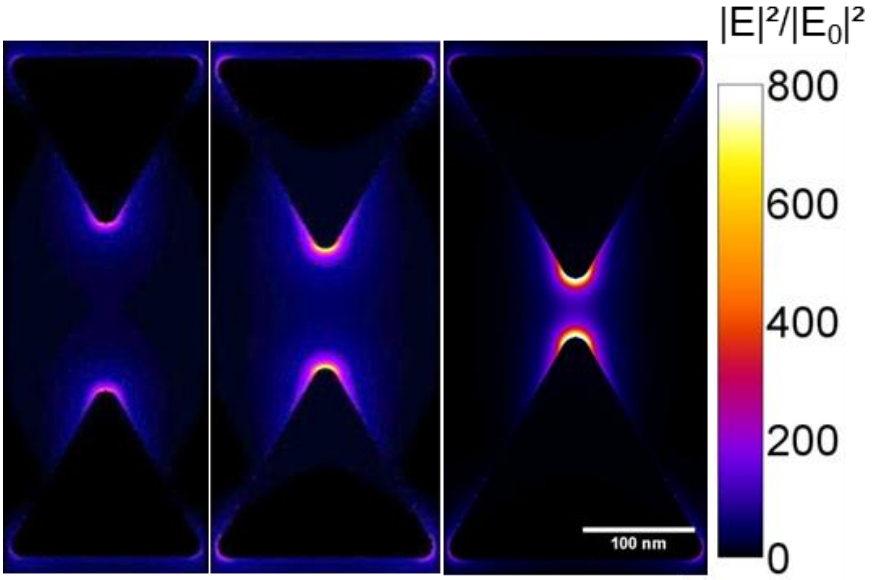

Figure 5.4. FDTD simulations of the electromagnetic field enhancement between tips of gold nanoantennas. XY projections of the calculated intensities of the electromagnetic field enhancement between tips of plasmonic bow-tie nanoantennas. Simulations were performed for a wavelength λ = 1064 nm, assuming a glass substrate. The triangle height was set to be 30 nm, and the tip distances were set between 130 nm, 93 nm, and 46 nm. The colored scale bar represents the enhancement factor of the electric field.

The results obtained via FDTD computations are comparable to values in the literature. Sundaramurthy et al. computed the electromagnetic field enhancement factor between 10^2 (for 160 nm tip's distance) and 10^3 (for 16 nm tip's distance) [55].

5.2. Near-field trapping and positioning of dielectric particles of nano- and micro-sizes.

Polystyrene beads with 1.1-µm diameter.

To investigate the principle possibility of near-field trapping on plasmonic nanoantenna arrays, near-field trapping of 1.1 µm big polystyrene spheres was performed. Polystyrene beads diffuse freely in a solution before laser irradiation (Figure 5.5a). At the time of switching on the NIR laser, the polystyrene beads have been trapped on the part of plasmonic nanoantenna structures that the resonant laser has illuminated. Moving the laser along the plasmonic nanoantenna structure can clearly visualize the trapping of polystyrene beads along the laser path on plasmonic nanoantenna structures. It was possible to create different shapes of printed polystyrene beads on top of the substrate, such as lines and hexagonally closed pack arrays. To demonstrate that trapping occurs due to the near-field enhancement, the trapping of polystyrene

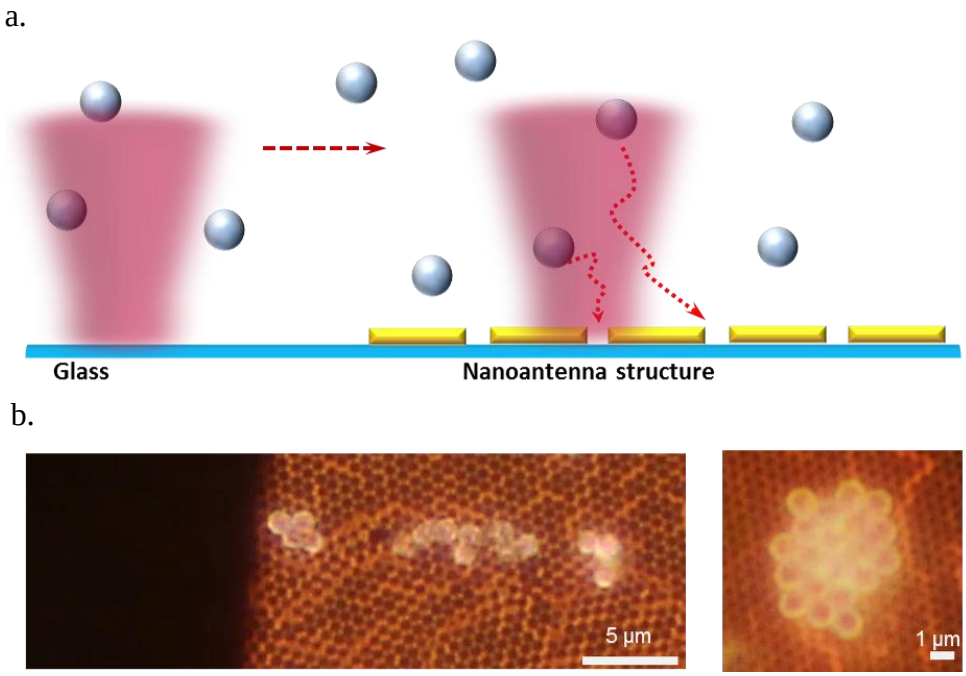

Figure 5.5. Near-field trapping of polystyrene 1.1 µm beads . A schematic illustration of near-field trapping on plasmonic nanoantennas under NIR laser irradiation (a). Polystyrene beads were trapped on a plasmonic nanoantenna structure. No stable trapping was observed on pure glass (b).

beads on the plasmonic nanoantenna and on the glass area was performed. At the same laser power densities, near-field trapping was possible only on the plasmonic nanoantenna array.

Figure 5.5b shows dark-field images of adherent polystyrene beads on top of a plasmonic bow-tie nanoantennas. Polystyrene beads mimic the pattern of plasmonic nanoantennas and form a hexagonal array. The control experiments on the glass surface concluded that the trapping of polystyrene spheres under low laser power densities is possible only on plasmonic nanoantenna structures.

Silica beads in the same size range as viruses.

Next, silica beads with diameters of 150 nm, 350 nm, and 580 nm were subject to the near-field trapping. Y. Tanaka *et al.* showed that it is possible to trap 100-nm polystyrene particles between diagonally alighted gold nanoblocks [139]. The authors used a geometry that M. Juan *et al.* reported earlier [153]. B. Roxworthy *et al.* reported the stable trapping of 500-nm polystyrene beads on a plasmonic nanoantenna scaffold consisting of nanotriangles with tips directed toward each other [53].

The dependence of the laser power density required for the stable trapping of silica beads on plasmonic nanoantenna structures with different gap sizes was studied systematically. Silica beads are too small to be resolved with a dark-field microscope, but the trapped particles appeared as a blurred spot. Figure 5.6 shows how the substrate looks before switching on the laser and then during and after laser illumination. After switching on the laser, a blurred spot on the surface was observed. When the laser was switched off, the trapped silica beads diffused away. The contrast of the images is improved by subtracting the background (Figure 5.6b). The sizes of the bright spots, where the silica beads were trapped, are presented in Figure 5.6c. Forty seconds after switching on the laser, the size of the spot was around 3.8 μm. However, after 60 seconds, the spot enlarged up to 4.7 μm. After a longer exposure time, the accumulation of silica beads was observed.

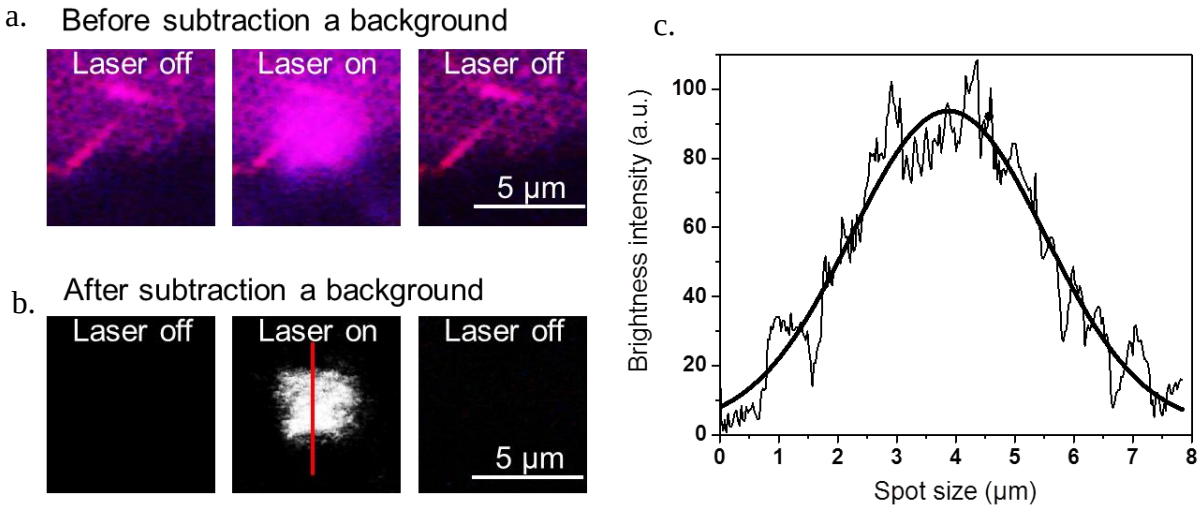

Figure 5.6. Near-field trapping of silica beads on plasmonic nanoantenna structures. The dark-field images of substrate before switching on the laser, when the laser is switched on, and after switching the laser off (a).The long-pass filter with cutoff wavelength of 690 nm was applied during measurements. After subtracting the background, the same images are given (b). The measured size of the spot of trapped silica beads after 40 s is shown (c).

In Figure 5.7a, the laser power density dependence for trapping silica beads with different sizes on gap sizes is presented. For silica beads 150 nm in diameter, trapping laser power density decreases with the decreasing tip distance of plasmonic nanoantenna structures. Due to decreasing gap sizes, stronger electromagnetic field enhancement between the tips of the nanoantennas takes place. However, for silica beads with diameters of 350 and 580 nm, the dependence of trapping laser power density is not straightforward. With an increase in the tip distance, the laser power density required for stable trapping decreases, contrary to our expectation. The tendency can be explained considering geometrical parameters (Figure 5.8). Silica beads 150 nm in diameter are the smallest beads and more easily fit in the gap between the tips of the plasmonic nanoantennas. However, the drawback of using small low-refractive index objects is that stable trapping is harder to achieve. On the other hand, silica beads with diameters of 350 and 580 nm have larger sizes, which facilitates trapping with reasonable laser power density. Furthermore, silica beads with the mentioned sizes can still enter the gaps between the plasmonic nanoantenna tips. Considering these two competing factors, one can conclude that in the case of 350-nm and 580-nm silica beads, both factors are balanced to achieve the best trapping efficiency. For a tip distance of 20 nm, the required laser power densities for achieving stable trapping for silica beads of all sizes are noticeably higher than the laser power densities for

a 47-nm tip distance. This phenomenon should be explained by taking into account the fact that more than half of the nanoantennas for an etching time of 150 seconds (20-nm tip distance) are interconnected. Therefore, near-field trapping cannot take place between the tips of plasmonic nanoantennas, and it happens between nanoantenna sides. Additionally, control experiments and optically trapped silica beads of all sizes on the glass surfaces and in a solution (3D) were performed. Laser power densities measured in control experiments were two orders of magnitude higher than the laser power densities required for near-field trapping on plasmonic nanoantennas. With plasmonic nanoantenna structures, it was possible to reduce the laser power density up to 100 times to achieve the stable trapping of silica beads.

Figure 5.7b presents SEM images for 150-nm, 350-nm, and 580-nm silica beads trapped between tips of plasmonic nanoantennas. According to these measurements, silica beads are mainly trapped between the tips of plasmonic nanoantennas, where one can expect the strongest electromagnetic field enhancement. However, a ratio of silica beads trapped on nanoantenna sides was observed. For 150-nm silica beads, it is possible that two particles sit in the gap. For silica beads with diameters of 350 nm and 580 nm, however, such a case was not observed.

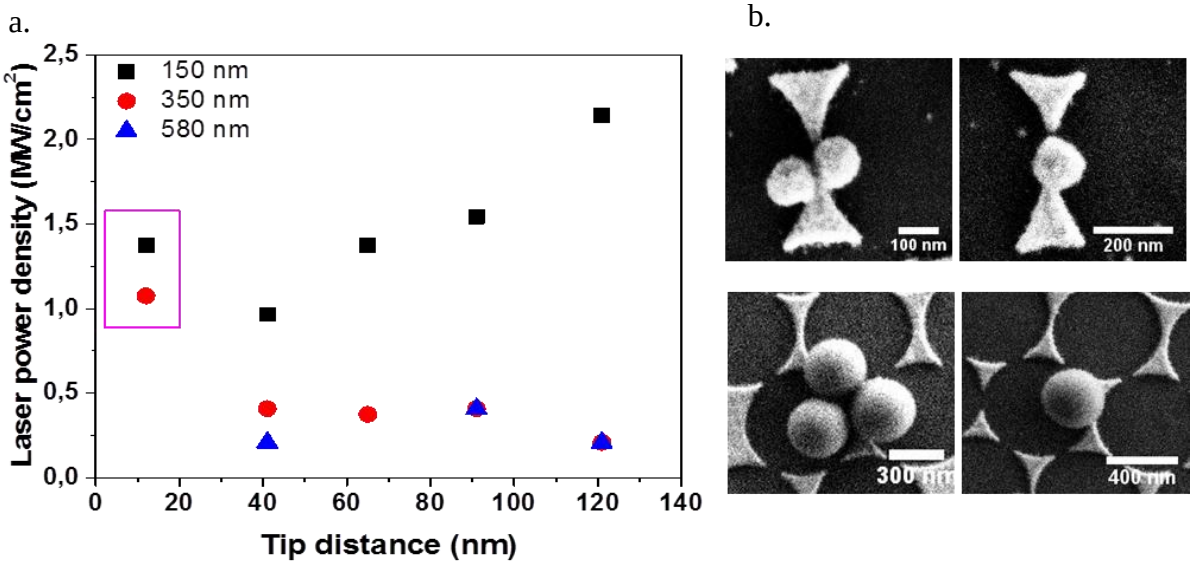

Figure 5.7. Near-field trapping of silica beads. The laser power dependence on the silica beads size and the tip-to-tip distance is shown. With increasing gap size, the electromagnetic field enhancement decreases. Therefore, a higher laser power density is needed to achieve the stable trapping of silica beads (a). SEM images of trapped 150-nm, 350-nm, and 870-nm silica beads are presented (b). SEM measurements reveal that the main part of the silica beads have been trapped between the nanoantennas' tips; however, trapped beads on the side of the nanoantennas were observed as well.

Figure 5.8 demonstrates YZ projections of the electromagnetic field enhancement between plasmonic nanoantennas with different gap sizes (130 nm, 93 nm, and 46 nm). The white circles represent the silica beads with diameters of 150 nm and 350 nm. The silica beads and nanoantennas are depicted in accordance with their proportions relatively to each other. As mentioned above, silica beads 150 nm in diameter fit in the gap between the plasmonic nanoantennas, but a smaller volume of the beads is exposed to the enhanced electromagnetic field. Furthermore, thermal fluctuations are stronger, which is affecting smaller objects. Silica beads with diameters of 350 nm less fit in the gaps between plasmonic nanoantennas. However, an increase in size leads to less thermal fluctuations and more stable trapping. Therefore, in the case of 150-nm silica beads, electromagnetic field enhancement plays a significant role in trapping. Although for silica beads with diameters of 350 nm and 580 nm the electromagnetic field enhancement facilitates the near-field trapping and reduces laser power densities by a few orders of magnitude, it does not show strong dependence on gap sizes. Overall, the electromagnetic field enhancement, the sizes of the objects, and the gap size affect near-field trapping along with thermal fluctuations.

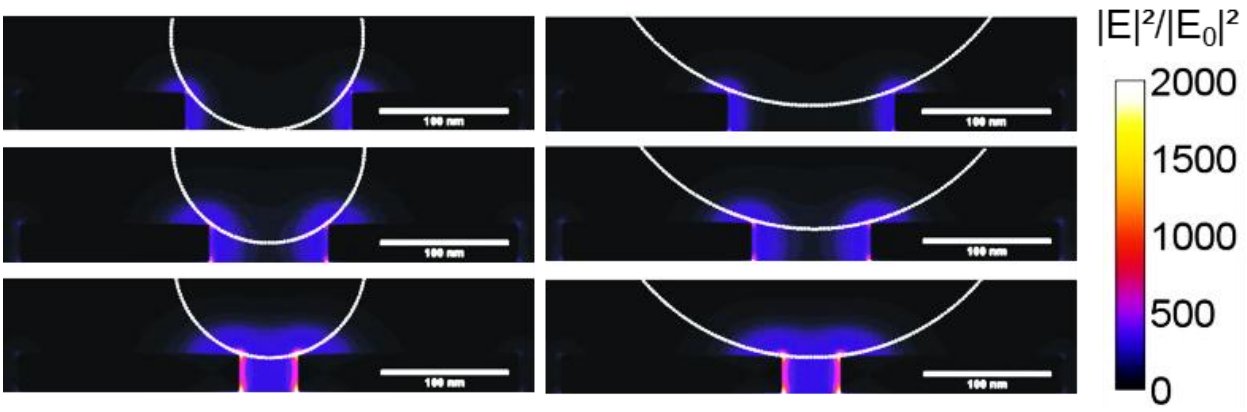

Figure 5.8. Geometry of silica beads with respect to the gap size. YZ projections of electromagnetic field enhancement calculated with FDTD and the silica beads with 150-nm and 350-nm diameters. Silica beads with 150-nm diameters can more easily enter the gap between plasmonic nanoantennas, but a smaller surface area is exposed to electromagnetic field enhancement compared with silica beads 350 nm in diameter.

5.3. Direct delivery of nano-objects onto plasmonic "hot spots."

The optical manipulation of metallic nanoparticles by using optical tweezers is a well-established technique. However, the precise positioning of nano-objects on a substrate with optical tweezers for the fabrication of hybrid nanostructures remains a challenge. Hybrid nanostructures are nanomaterials, which consist of several individual nano-objects [154]. Hybrid nanostructures exhibit the functional properties of individual nano-objects, but also, new synergetic properties can be observed [155]. Different ways of delivering nano-objects and composing plasmonic hybrid nanostructures have been reported [39,43,156]. Plasmonic nanoantennas provide the unique opportunity to trap and locate nano-objects in their vicinity [156]. Here, it is demonstrated how a combination of far-field and near-field optical forces can be used to create hybrid nanostructures by the direct delivery of single nano-objects to the "hot spot" region.

Optical tweezers allow for the relocation and positioning of nano-objects in the vicinity of "hot spots" (Figure 5.9a). When nano-objects are located sufficiently close to the "hot spots" of plasmonic nanoantennas. Near-field forces overcome the far-field optical forces, which leads to the escape of nano-objects from the optical trap into the "hot spot" on plasmonic nanoantenna structures. Here, the feasibility of this approach with gold nanoparticles 80 nm in diameter and nanodiamonds 100 nm in diameter is shown.

Figure 5.9a shows the dark-field images of gold nanoparticles in an optical trap of a tightly focused NIR laser. When the gold nanoparticle is located close enough to the plasmonic nanoantenna structures, it escapes from the laser beam and jumps into the gap between the tips of the nanoantenna. The SEM image next to the dark-field images confirms that the gold nanoparticle was trapped between the tips of gold nanoantennas. This approach was extended to nanodiamonds as shown in Figure 5.9b. It confirms the same behavior for nanodiamonds and gold nanoparticles. The laser power densities required for the stable optical trapping of gold nanoparticles or nanodiamonds could be high enough to overheat the plasmonic nanoantenna structure, which leads to bubble formation and disturbs the experiments. Hence, it was feasible to only deliver particles into "hot spots" on the boundary between the glass surface and the plasmonic nanoantenna array.

a.

b.

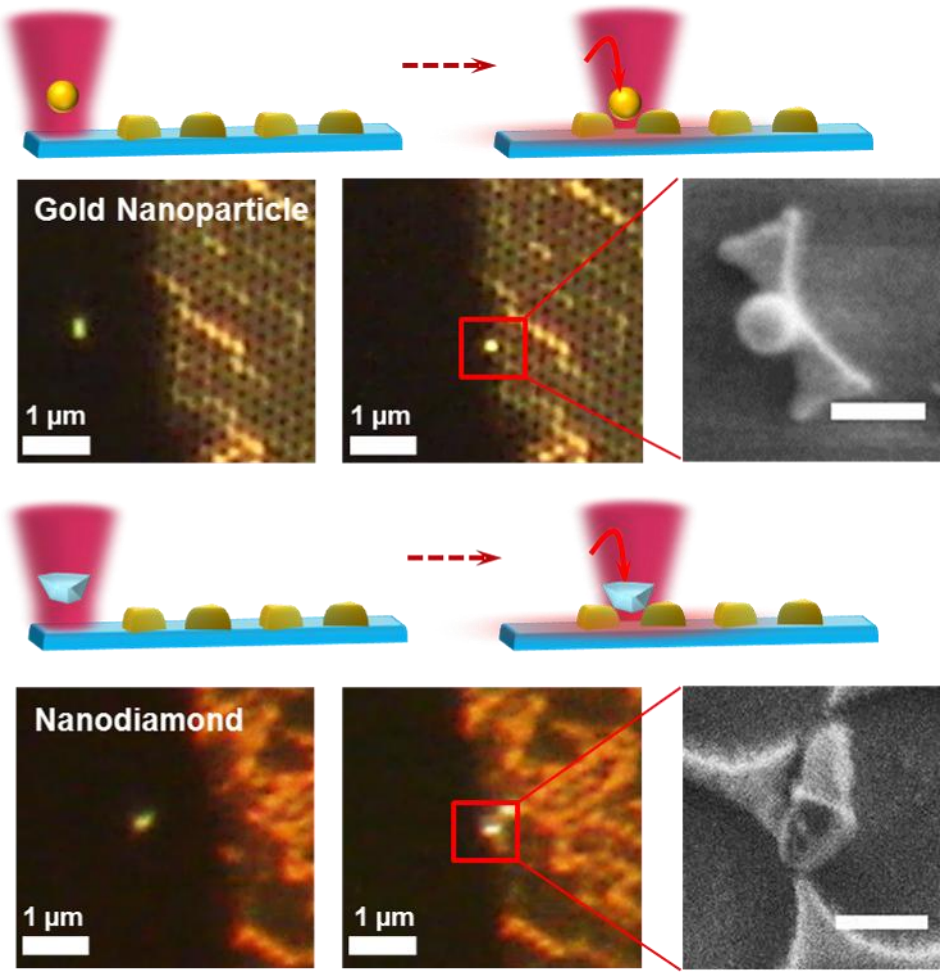

Figure 5.9. Direct delivery of nano-objects to plasmonic "hot spots." Schematic illustration of the single-particle-delivery experiment. The 80nm gold nanoparticle has been trapped with a tightly focused NIR laser beam (λ = 1064 nm) and delivered directly into the hot spot of a plasmonic nanoantenna array. Dark-field images and the SEM image of the gold nanoparticle trapped between the tips of the plasmonic nanoantennas are given (a). This approach was extended to nanodiamonds with sizes of 100 nm. Dark-field images and the SEM image are shown (b).

5.4. Overheating.

Plasmonic nanostructures experience strong heating under resonant laser illumination [65]. Various studies have been devoted to the plasmonic heating of nanoparticle arrays [157,158]. Baffou *et al.* showed that an array of gold nanoparticles trigger an overheating process that leads to bubble formation under *cw* laser irradiation. Authors studied in detail the dependence of the temperatures around gold nanoparticles on the applied laser power density [158]. In this work, overheating is an essential issue, which may affect the trapping process. To prevent bubble formation and perturbation, which can occur during near-field trapping, the dependence of the laser power density required to observe bubble formation on the nanoantenna arrays was investigated.

In Figure 5.10 the dark-field microscopy images of a plasmonic nanoantenna array under *cw* laser irradiation are shown. The initial bubble forms on a pair of gold nanoantennas and has a diameter of around 1 μm. For a constant laser power, the bubble has the same size and does not increase or decrease. However, an increase or a decrease in the laser power density is followed by an increase or decrease in the bubble size.

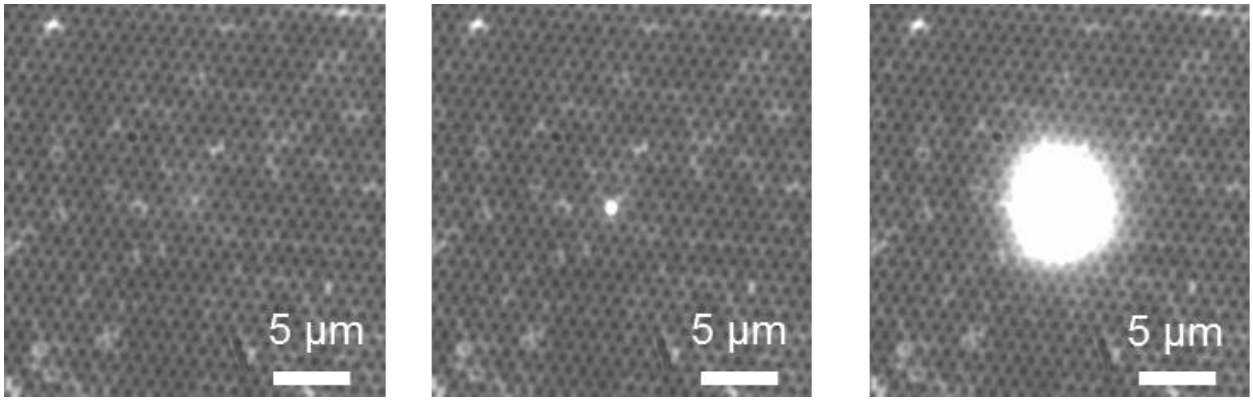

Figure 5.10. Bubble formation on plasmonic nanoantennas under *cw* laser irradiation. The dark-field microscopy images of bubble formation on the array of plasmonic nanoantennas are shown. A vapour bubble forms when the laser power density reaches a certain value sufficient for overheating the surrounding medium (water).

Figure 5.11. shows the dependence of the laser power density threshold for bubble formation on plasmonic nanoantenna arrays under *cw* laser irradiation for different gap sizes. To initiate bubble formation on a plasmonic nanoantenna array with a gap size of 12 nm, higher laser power densities are required compared to plasmonic nanoantennas with larger gaps. With increasing gap size, the required laser power density decreases.

The laser power density dependence does not show a monotonic character and depends on many factors, such as the side length of the plasmonic nanoantennas, the gap size, and the external additional heating from the xenon lamp in the dark-field microscope. However, the laser power, which is required to initiate bubble formation on plasmonic nanoantenna arrays, is higher than the laser power required to achieve stable near-field trapping of silica beads. Therefore, one can conclude that the near-field trapping of silica particles on plasmonic nanoantenna substrates is not disturbed by bubble formation.

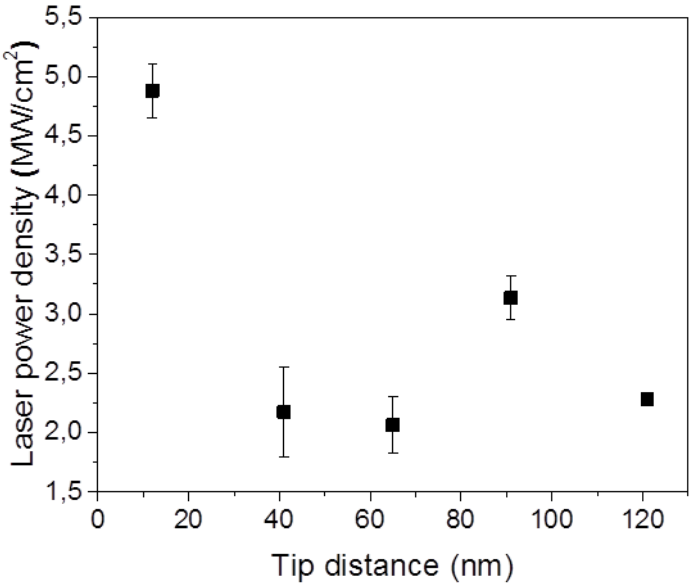

Figure 5.11. **Dependence of laser power densities required for micro-bubble formation on gap size of plasmonic nanoantennas.** A higher laser power density is needed to create bubbles on plasmonic nanoantenna arrays in contrast to the laser power density required to achieve the stable near-field trapping of silica particles.

5.5. Summary.

In this chapter, it was shown how large arrays of plasmonic nanoantennas on a glass surface can be synthesized by colloidal lithography. The possibility of tuning the optical properties and geometry over a large range by applying air and plasma treatment was discussed in detail. A decrease in gap sizes leads to an increase in electromagnetic field enhancement. The near-field trapping of low-refractive nano-objects was performed. The dependence of laser power density on the gap sizes clearly demonstrates that a decrease in the gap sizes and a corresponding increase in electromagnetic field enhancement lead to a decrease in the laser power densities required to complete the near-field trapping of silica beads with diameters of 150 nm.

The principal possibility of directly delivering nano-objects trapped by an optical tweezer into “hot spots” of plasmonic nanoantennas was demonstrated. This new approach renders it possible to create hybrid nanostructures with a nanometer accuracy. Gold nanoparticles and nanodiamonds were successfully loaded in gaps between plasmonic nanoantennas. The creation of hybrid structures with nanometer precision holds promising possibilities to study the optical properties of plasmonically coupled systems and for the fabrication of hybrid structures with a desired optical response and geometry.

Vapor bubble formation was observed on plasmonic nanoantenna arrays for high laser powers. The threshold of laser power densities required to overheat the solvent on plasmonic nanoantennas and to create a vapor bubble was higher compared with the near-field trapping experiments in an ensemble. Steady-state bubbles formed around gold structures can be used in solvothermal chemistry, where superheated liquids (e.g., water) are used as solvents. Therefore, plasmonic nanoantenna arrays are promising candidates for studying liquid overheating by laser irradiation.

6. Summary and outlook.

The interaction of plasmonic nanostructures with an external electric field is responsible for various effects, such as near-field enhancement, plasmonic heating, and optical forces. All mentioned phenomena were applied in this work to manipulate nano-objects. In this work, a *cw* resonant laser was used for both reshaping gold nanorods and optically printing them on a glass surface, as well as for positioning nanoparticles into "hot spots" of plasmonic nanoantennas. The temperature effects on a nanoscale level were discussed.

In the first part, it was shown that it is possible to create V-shaped antennas with the desired bending angles and to pattern them on the substrate with the preferred orientation. This is a new approach, which in the future can be used for creating metasurfaces with single-unit elements less than 100 nm in size, and which could operate in the visible range of the spectrum. Compared with e-beam lithography, optical printing allows for the fabrication of V-shaped nanorods with a high degree of monocrystallinity and the possibility of controlling the bending angle. Furthermore, the printing of V-shaped antennas is possible on almost any surface. All in all, the technique elaborated in this thesis to bend and print V-shaped antennas on a surface becomes an alternative technique for e-beam lithography and focused ion-beam milling, and it enables the fabrication of sub-100 nm V-shaped nanoparticles. The bending angle and the orientation of the V-shaped antennas were controllable to a reasonable degree. To improve control over the positioning of V-shaped antennas, one can think about using two-color laser printing [102] or tilting a substrate to get a predominant orientation. Besides, by splitting a laser beam into multiple beams and simultaneously printing several lines of V-shaped antennas, this could increase the speed of the process.

In the second part of this thesis, large arrays of plasmonic nanoantennas were fabricated with colloidal lithography and were used as a platform for near-field trapping of low-refractive index objects, such as silica beads. It was demonstrated that plasmonic nanoantennas indeed assist the trapping of dielectric particles. It was possible to trap silica beads with sizes down to 150 nm in an ensemble between the tips of plasmonic nanoantennas, where the strongest electromagnetic field enhancement was expected. Such a system of combined plasmonic nanoantennas and trapped silica beads can be used in the future as a new platform for SERS experiments on single particles. Silica beads can be coated with a desired passivating agent and then trapped in the "hot spots" of plasmonic nanoantennas allowing for SERS measurements.

Additionally, the possibility of using plasmonic nanoantennas for the direct delivery of nano-objects into a “hot spot” was shown. Conventional optical tweezers was used initially to relocate a trapped object close to a “hot spot”. When near-field enhancement overcomes far-field optical forces, the nano-object, such as a gold nanoparticle or nanodiamond, escapes from the far-field optical trap into the “hot spot”. The feasibility of this approach was tested with gold nanoparticles and nanodiamonds. This technique is a promising approach for fabricating hybrid nanostructures with desired geometrical parameters and optical response.

Finally, vapor bubble formation on plasmonic nanoantennas under CW laser illumination was investigated. The dependence of threshold laser power density required for bubble formation on the gap size was shown, and it was concluded that the near-field trapping of silica beads takes place for lower laser power densities. By adjusting the laser power density, it is possible to create steady-state vapor bubbles. The microbubbles around plasmonic nanoantennas may serve as a local autoclave for conducting chemical reactions at the nanoscale with an overheated solvent.

7. Bibliography.

[1] M. Faraday, "The bakerian lecture: experimental relations of gold (and other metals) to light", Philosophical Transactions of the Royal Society of London, vol. 147,pp. 145–181, 1857.

[2] G. Mie, "Beiträge zur Optik trüber Medien, speziell kolloidaler Metallösungen," Annalen der Physik, Vol. 330, No. 3, pp. 377–445, 1908.

[3] The official Web Site of the Nobel Prize, https://www.nobelprize.org/nobel_prizes/chemistry/laureates/1925/zsigmondy-facts.html

[4] M. Grzelczak, J. Pérez-Juste, P. Mulvaney and L. M. Liz-Marzán, "Shape control in gold nanoparticle synthesis", Chemical Society Reviews, Vol. 37, pp. 1783–1791, 2008.

[5] X. Huang, M. A. El-Sayed, "Gold nanoparticles: Optical properties and implementations in cancer diagnosis and photothermal therapy", Journal of Advanced Research, Vol. 1, Is. 1, pp. 13–28, 2010.

[6] N. R. Jana, L. Gearheart, C. J. Murphy, "Seeding Growth for Size Control of 5-40 nm Diameter Gold Nanoparticles", Langmuir, Vol. 17, pp. 6782-6786, 2001.

[7] E. Ringe, J. M. McMahon, K. Sohn, C. Cobley, Y. Xia, J. Huang, G. C. Schatz, L. D. Marks, R. P. Van Duyne, "Unraveling the Effects of Size, Composition, and Substrate on the Localized Surface Plasmon Resonance Frequencies of Gold and Silver Nanocubes: A Systematic Single-Particle Approach", Journal of Physical Chemistry C, Vol. 114, pp. 12511–12516, 2010.

[8] J. Pérez-Juste, I. Pastoriza-Santosa, L. M. Liz-Marzána, P. Mulvaney, "Gold nanorods: Synthesis, characterization and applications", Coordination Chemistry Reviews, Vol. 249, Is. 17–18, pp. 1870–1901, 2005.

[9] M. and Ph. Guyot-Sionnest, "Mechanism of Silver(I)-Assisted Growth of Gold Nanorods and Bipyramids", The Journal of Physical Chemistry B, Vol. 109, Is. 47, pp. 22192–22200, 2005.

[10] J. Ye, P. Van Dorpe, W.Van Roy, G. Borghs and G. Maes, "Fabrication, Characterization, and Optical Properties of Gold NanobowlSubmonolayer Structures", Langmuir, Vol. 25, Is.3, pp. 1822–1827, 2009.

[11] C. Li, K. L. Shuford, M. Chen, E. Je Lee and S. Oh Cho, "A Facile Polyol Route to Uniform Gold Octahedra with Tailorable Size and Their Optical Properties", ACS Nano, Vol. 2, No. 9, pp. 1760–1769, 2008.

[12] J. Chen, J. M. McLellan, A. Siekkinen, Y. Xiong, Z.-Y. Li, and Y. Xia, "Facile Synthesis of Gold−Silver Nanocages with Controllable Pores on the Surface", Journal of American Chemical Society, Vol. 128, No.46, pp. 14776–14777, 2006.

[13] T. Shoji, Y. Tsuboi, "Plasmonic Optical Tweezers toward Molecular Manipulation: Tailoring Plasmonic Nanostructure, Light Source, and Resonant Trapping", Journal of Physical Chemistry Letters, Vol. 5, pp. 2957−2967, 2014.

[14] G. K. Joshi, K. N. Blodgett, B. B. Muhoberac, M. A. Johnson, K. A. Smith, and R. Sardar, "Ultrasensitive Photoreversible Molecular Sensors of Azobenzene-Functionalized PlasmonicNanoantennas", Nano Letters, Vol. 14, No. 2, pp. 532–540, 2014.

[15] S. Enoch, R. Quidant, G. Badenes, "Optical sensing based on plasmon coupling in nanoparticle arrays", Optics Express, Vol. 12, No. 15, pp. 3422-3427, 2004.

[16] P. Ghosh, G. Han, M. De, C. K. Kim, V. M. Rotello, "Gold nanoparticles in delivery applications", Advanced Drug Delivery Reviews, Vol. 60, Is.11, pp. 1307–1315, 2008.

[17] G. Baffou and R. Quidant, "Thermo-plasmonics: using metallic nanostructures as nano-sources of heat", Laser & Photonics Reviews, Vol. 7, Is. 2, pp. 171–187, 2013.

[18] S. A. Maier, "Plasmonics: fundamentals and applications", Springer Science+ Business Media, 2007.

[19] U. Kreibig and M. Vollmer, "Optical properties of metal clusters", Springer-Verlag, 1995.

[20] J. D. Jackson, "Classical electrodynamics, 3rd ed.," American Journal of Physics, Vol. 67, p. 841, Sept. 1999.

[21] C. Zensen, N. Villadsen, F. Winterer, S. R. Keiding, T. Lohmüller, "Pushing nanoparticles with light - A femtonewton resolved measurement of optical scattering forces", APL Photonics, Vol. 1, 026102, 2016.

[22] P. B. Johnson and R. W. Christy, "Optical Constants of the Noble Metals", Physical Review B, Vol. 6, No.12, pp. 4370-4379, 1972.

[23] H. Kuwata, H. Tamaru, K. Esumi, and K. Miyano, "Resonant light scattering from metal nanoparticles: Practical analysis beyond Rayleigh approximation," Applied Physics Letters, Vol. 83, No. 22, pp. 4625–4627, 2003.

[24] Y. Song, P.D. Nallathamby, T. Huang, H. E. Elsayed-Ali, and X.-H. N. Xu, "Correlation and characterization of three-dimensional morphologically dependent localized surface plasmon resonance spectra of single silver nanoparticles using dark-field optical microscopy and spectroscopy and atomic force microscopy", Journal of Physical Chemistry C, Vol. 114, pp. 74-81, 2010.

[25] G. H. Chan, J. Zhao, E. M. Hicks, G. C. Schatz, R. P. Van Duyne, „Plasmonic properties of copper nanoparticles fabricated by nanosphere lithography", Nano Letters, Vol. 7, No.7, pp. 1947-1952, 2007.

[26] J.-Y. Bigot, J.-C. Merle, O. Cregut, and A. Daunois, "Electron Dynamics in Copper Metallic Nanoparticles Probed with Femtosecond Optical Pulses", Physical Review Letters, Vol. 75, No. 25, pp. 4702-4706, 1995.

[27] A. Wokaun, J.P. Gordon, P.F. Liao. "Radiation damping in surface-enhanced Raman scattering", Physical Review Letters,Vol. 48, No. 14, pp. 957-960, 1982.

[28] J. Kittel, "Introduction to Solid State Physics", Wiley, New York, 1996.

[29] C.F. Bohren, D.R. Huffman, "Absorption and Scattering by Small Particles", Wiley, New York, 1983.

[30] P. Anger, P. Bharadwaj, L. Novotny, "Enhancement and Quenching of Single-Molecule Fluorescence", Physical Review Letters, Vol. 96, 113002, 2006.

[31] S. Lal, S. Link, N. J. Halas, "Nano-optics from sensing to waveguiding", Nature Photonics, Vol. 1, pp. 641-648, 2007.

[32] D. Courjon, C. Bainier, "Near field microscopy and near field optics", Reports on Progress in Physics, Vol. 57, pp. 989-1028, 1994.

[33] K. Kneipp, Y. Wang, H. Kneipp, L. T. Perelman, I.Itzkan, R. R. Dasari, M. S. Feld, "Single Molecule Detection Using Surface-Enhanced Raman Scattering (SERS)", Physical Review Letters, Vol. 78, No. 9, pp. 1667- 1670, 1997.

[34] M. E. W. Born, "Principles of Optics", Cambridge University Press, 1997.

[35] S. Enoch, N. Bonod, "Plasmonics. From Basics to Advanced Topics", Springer Series in Optical Sciences, 2012.

[36] A. Grubisic, E. Ringe, C. M. Cobley, Y. Xia, L. D. Marks, R. P. Van Duyne, D. J. Nesbitt, "Plasmonic Near-Electric Field Enhancement Effects in Ultrafast Photoelectron Emission: Correlated Spatial and Laser Polarization Microscopy Studies of Individual Ag Nanocubes", Nano Letters, Vol. 12, No. 9, pp. 4823−4829, 2012.

[37] C. Deeb, X. Zhou, R. Miller, St. K. Gray, S. Marguet, J. Plain, G. P. Wiederrecht, and R. Bachelot, "Mapping the Electromagnetic Near-Field Enhancements of Gold Nanocubes", Journal of Physical Chemistry C, Vol. 116, No. 46, pp. 24734-24740, 2012.

[38] F. Hao, C. L. Nehl, J. H. Hafner, P. Nordlander, "Plasmon Resonances of a Gold Nanostar", Nano Letters, Vol.7, No.3, pp. 729-732, 2007.

[39] P. Kühler, M. Weber, and T. Lohmüller, "Plasmonic Nanoantenna Arrays for Surface-Enhanced Raman Spectroscopy of Lipid Molecules Embedded in a Bilayer Membrane", ACS Applied Materials and. Interfaces, Vol. 6, No. 12, pp. 8947-8952, 2014.

[40] V. Myroshnychenko, J. Rodríguez-Fernández, I. Pastoriza-Santos, A.M. Funston, C. Novo, P. Mulvaney, L. M. Liz-Marzán and F. J. García de Abajo, "Modelling the optical response of gold nanoparticles", Chemical Society Review, Vol.37, pp. 1792-1805, 2008.

[41] V.V. Thacker, L. O. Herrmann, D. O. Sigle, T. Zhang, T. Liedl, J. J. Baumberg and U. F. Keyser, "DNA origami based assembly of gold nanoparticledimers for surface-enhanced Raman scattering", Nature Communications, Vol.5, No. 3448, 2014.

[42] Y. Huang, L. Ma, M. Hou, J. Li, Z. Xie and Z. Zhang, "Hybridized plasmon modes and near-field enhancement of metallic nanoparticle-dimer on a mirror", Scientific Reports, Vol. 6, Article 30011, 2016.

[43] P. Kühler, E.-M. Roller, R. Schreiber, T. Liedl, T. Lohmüller, and J. Feldmann, "Plasmonic DNA-Origami Nanoantennas for Surface-Enhanced Raman Spectroscopy ", Nano Letters, Vol. 14, No. 5, pp. 2914-2919, 2014.

[44] P. Nordlander, C. Oubre, E. Prodan, K. Li and M. I. Stockman, "Plasmon Hybridization in Nanoparticle Dimers", Nano Letters, Vol. 4, No. 5, pp. 899-903, 2004.

[45] M. Kasha, "Energy Transfer Mechanisms and the Molecular Exciton Model for Molecular Aggregates", Radiation Research, Vol. 20, pp. 55-71, 1963.

[46] P. K. Jain, W. Huang, and M. A. El-Sayed, "On the Universal Scaling Behavior of the Distance Decay of Plasmon Coupling in Metal Nanoparticle Pairs: A Plasmon Ruler Equation", Nano Letters, Vol. 7, No. 7, pp. 2080-2088, 2007.

[47] B. Z. Packard, D. D. Toptygin, A. Komoriya, L. Brand, "Intramolecular Resonance Dipole-Dipole Interactions in a Profluorescent Protease Substrate", Journal of Physical Chemistry B, Vol. 102, No. 4, pp.752-758, 1998.

[48] K. Schraml, M. Spiegl, M. Kammerlocher, G. Bracher, J. Bartl, T. Campbell, J. J. Finley, and M. Kaniber, "Optical properties and interparticle coupling of plasmonic bowtie nanoantennas on a semiconducting substrate", Physical Review B, Vol. 90, 035435, 2014.

[49] L. Novotny and N. van Hulst, "Antennas for light", Nature Photonics, Vol. 5, pp. 83-90, 2011.

[50] J. N. Farahani, D.W. Pohl, H.-J. Eisler, B. Hecht, "Single Quantum Dot Coupled to a Scanning Optical Antenna: A Tunable Superemitter", Physical Review Letters, Vol. 95, 017402, 2005.

[51] D. P. Fromm, A. Sundaramurthy, A. Kinkhabwala and P. J. Schuck, G. S. Kino, W. E. Moerner, "Exploring the chemical enhancement for surface-enhanced Raman scattering with Au bowtie nanoantennas", Journal of Chemical Physics, Vol. 124, No. 6, 61101, 2006.

[52] N. Yu, E. Cubukcu, L. Diehl, D. Bour, S. Corzine, J. Zhu, G. Höfler, K. B. Crozier, F.Capasso, "Bowtie plasmonic quantum cascade laser antenna", Optics Express, Vol. 15, No. 20, pp. 13272- 13281, 2007.

[53] B. J. Roxworthy, K. D. Ko, A. Kumar, K. Hung Fung, E. K. C. Chow, G. Logan Liu, N. X. Fang, K. C. Toussaint Jr., "Application of Plasmonic Bowtie Nanoantenna Arrays for Optical Trapping, Stacking, and Sorting", Nano Letters, Vol. 12, No. 2, pp. 796-801, 2012.

[54] H. Fischer and O. J. F. Martin, "Engineering the optical response of plasmonic nanoantennas", Optics Express, Vol. 16, Is. 12, pp. 9144-9154, 2008.

[55] A. Sundaramurthy, K. B. Crozier, and G. S. Kino, D. P. Fromm, P. J. Schuck, and W. E. Moerner, "Field enhancement and gap-dependent resonance in a system of two opposing tip-to-tip Au nanotriangles", Physical Review B, Vol. 72, 165409, 2005.

[56] L. Lin and Y. Zheng, "Optimizing plasmonic nanoantennas via coordinated multiple coupling", Scientific Reports, Vol. 5, 14788, 2015.

[57] K. L. Shuford, M. A. Ratner, G. C. Schatz, "Multipolar excitation in triangular nanoprisms", The Journal of Chemical Physics, Vol. 123, 114713, 2005.

[58] J. Nelayah, M. Kociak, O. Stephan, N. Geuquet, L. Henrard, F. J. García de Abajo, I. Pastoriza-Santos, L. M. Liz-Marzán, C. Colliex, "Two-Dimensional Quasistatic Stationary Short Range Surface Plasmons in Flat Nanoprisms", Nano Letters, Vol. 10, pp. 902–907, 2010.

[59] E. Hao, G. C. Schatz, J. T. Hupp, "Synthesis and Optical Properties of Anisotropic Metal Nanoparticles", Journal of Fluorescence, Vol. 14, No. 4, pp. 331- 341, 2004.

[60] J. B. Herzog, M. W. Knight, and D. Natelson, "Thermoplasmonics: Quantifying Plasmonic Heating in Single Nanowires", Nano Letters, Vol. 14, No. 2, pp. 499–503, 2014.

[61] G. Baffou, R. Quidant, C. Girard. "Heat generation in plasmonic nanostructures: Influence of morphology", Applied Physics Letters, Vol. 94, No. 15, 153109, 2009.

[62] J. P. Wilcoxon, J. E. Martin, F. Parsapour, B. Wiedenman, and D. F. Kelley, "Photoluminescence from nanosize gold clusters," The Journal of Chemical Physics, Vol. 108, No. 21, p. 9137-9143, 1998.

[63] Young, D. Hugh, "University Physics", 7th Ed., Addison Wesley, 1992.

[64] D.D.L. Chung, "Materials for thermal conduction", Applied Thermal Engineering, Vol. 21, pp. 1593-1605, 2001.

[65] A. O. Govorov and H. H. Richardson, "Generating heat with metal nanoparticles", Nano Today, Vol. 2, No. 1, pp. 30–38, 2007.

[66] A. Ashkin, "Acceleration and trapping of particles by radiation pressure", Physical Review Letters, Vol. 24, No. 4, pp. 156-159, 1970.

[67] A. Ashkin, J. M. Dziedzic, J. E. Bjorkholm, and S. Chu, "Observation of a single-beam gradient force optical trap for dielectric particles", Optics Letters, Vol. 11, No. 5, pp. 288-290, 1986.

[68] R. Loudon and S. M. Barnett, "Theory of the radiation pressure on dielectric slabs, prisms and single surfaces," Optics Express, Vol. 14, No. 24, p. 11855, 2006.

[69] D. R. H. Craig, F. Bohren, "Absorption and Scattering of Light by Small Particles", John Wiley & Sons, INC., 1998.

[70] A. Rohrbach, E. H. Stelzer, "Optical trapping of dielectric particles in arbitrary fields", Journal of Optical Society of America A, Vol. 18, Is. 4, pp. 839-853, 2001.

[71] M. Dienerowitz, M. Mazilu, P. J. Reece, T. F. Krauss, K. Dholakia, "Optical vortex trap for resonant confinement of metal nanoparticles," Optics Express, Vol. 16, No. 7, pp. 4991–4999, 2008.

[72] M. Dienerowitz, M. Mazilu, K. Dholakia, "Optical manipulation of nanoparticles: a review", Journal of Nanophotonics, Vol. 2, 021875, 2008.

[73] R. R. Agayan, F. Gittes, R. Kopelman, C. F. Schmidt, "Optical trapping near resonance absorption", Applied Optics, Vol. 41, No. 12, pp. 2318-2327, 2002.

[74] R. Erni, M.D. Rossell, C.Kisielowski, U. Dahmen, "Atomic-Resolution Imaging with a Sub-50-pm Electron Probe", Physical Review Letters, Vol. 102, No. 9, 096101, 2009.

[75] D.G. Rickerby, G. Valdre`, U. Valdre`,"Impact of Electron and Scanning Probe Microscopy on materials Reseacrh", Springer-Science+Business Media, B.V., Italy.

[76] A. I. Kirkland, S. J. Haigh, "Nanocharacterisation: 2nd Edition", RSC Nanoscience & Nanotechnology, No. 37, The Royal Society of Chemistry, 2015.

[77] L.J. Clarke, "Surface Crystallography", John Wiley&Sons, New York, 1985.

[78] M. De Graef, M. E. McHenry, "Structure of Materials: An Introduction to Crystallography, Diffraction, and Symmetry", Cambridge University Press, 2007.

[79] A. Kelly, G.W. Groves, "Crystallography and Crystal Defects", Longman, London, 1970.

[80] D. Schwarzenbach, "Crystallography", John Wiley&Sons, 1996.

[81] H. S. Park, K. Gall, J.A. Zimmerman, "Deformation of FCC nanowires by twinning and slip", Journal of the Mechanics and Physics of Solids, Vol. 54, pp. 1862-1881, 2006.

[82] M. Jo, Y. M. Koo, B.-J. Lee, B. Johansson, L.Vitos, and S. K. Kwon, "Theory for plasticity of face-centered cubic metals", Proceedings of the National Academy of Sciences, Vol. 111, No. 18, pp. 6560-6565, 2014.

[83] J. A. Venables, "The electron microscopy of deformation twinning", Journal of Physics and Chemistry of Solids, Vol. 25, pp. 685-692, 1964.

[84] J. N. Reddy and D. K. Gartling, "The Finite Element Method in Heat Transfer and Fluid Dynamics", CRC Press, 2010.

[85] E. Palik, "Handbook of optical constants of solids", Academic Press, Orlando, 1985.

[86] D.R. Smith, W.J. Padilla, D.C. Vier, S.C. Nemat-Nasser, S. Schultz, "Composite medium with simultaneously negative permeability and permittivity", Physical Reviews Letters, Vol. 84, pp. 4184–4187, 2000.

[87] J.B. Pendry, "Negative refraction makes a perfect lens", Physical Review Letters, Vol. 85, pp. 3966–3969, 2000.

[88] D. Schurig, J. J. Mock, B. J. Justice, S. A. Cummer, J. B. Pendry, A. F. Starr, D. R. Smith, "Metamaterial Electromagnetic Cloak at Microwave Frequencies", Science, Vol. 314, pp. 977-980, 2006.

[89] B. Ng, S. M. Hanham, V. Giannini, Z. C. Chen, M. Tang, Y. F. Liew, N. Klein, M. H. Hong, and S. A. Maier, "Lattice resonances in antennas arrays for liquid sensing in the terahertz regime", Optics Express, Vol. 19, pp. 14653-14661, 2011.

[90] V. M. Shalaev, "Optical negative-index metamaterials", Nature Photonics, Vol. 1, pp. 41-48, 2007.

[91] O. M. Ramahi, T. S. Almoneef, M. AlShareef, and M. S. Boybay, "Metamaterial particles for electromagnetic energy harvesting", Applied Physics Letters, Vol. 101, 173903, 2012.

[92] V.M. Shalaev, W.S. Cai, U.K. Chettiar, H.K. Yuan, A.K. Sarychev, V.P. Drachev, A.V. Kildishev, "Negative index of refraction in optical metamaterials", Optics Letters, Vol. 30, pp. 3356–3358, 2005.

[93] W.S. Cai, U.K. Chettiar, H.K. Yuan, V.C. de Silva, A.V. Kildishev, V.P. Drachev, V.M. Shalaev, "Metamagnetics with rainbow colors", Optics Express, Vol. 15, pp. 3333–3341, 2007.

[94] W. Wu, E. Kim, E. Ponizovskaya, Y. Liu, Z. Yu, N. Fang, Y.R. Shen, A.M. Bratkovsky, W. Tong, C. Sun, X. Zhang, S.Y. Wang, R.S. Williams, "Optical metamaterials at near and mid-IR range fabricated by nanoimprint lithography", Applied Physics A, Vol. 87, pp. 143–150, 2007.

[95] C. Enkrich, R. Perez-Willard, D. Gerthsen, J.F. Zhou, T. Koschny, C.M. Soukoulis, M. Wegener, S. Linden, "Focused-ion-beam nanofabrication of near-infrared magnetic metamaterials", Advanced Materials, Vol. 17, pp.2547–2549, 2005.

[96] W. Cai, V. Shalaev, "Optical Metamaterials. Fundamentals and Applications", Springer, New York, 2010.

[97] N. Yu, P. Genevet, M. A. Kats, F. Aieta, J.-P.Tetienne, F. Capasso, Z. Gaburro, "Light Propagation with Phase Discontinuities: Generalized Laws of Reflection and Refraction", Science, Vol 334. pp. 333-337, 2011.

[98] M. Khorasaninejad, A. Y. Zhu, C. Roques-Carmes, W. T. Chen, J. Oh, I. Mishra, R. C. Devlin, F. Capasso, "Polarization-Insensitive Metalenses at Visible Wavelengths", Nano Letters, Vol. 16, pp. 7229−7234, 2016.

[99] M.J. Guffey, N.F. Scherer, "All-Optical Patterning of Au Nanoparticles on Surfaces Using Optical Traps", Nano Letters, Vol.10, pp.4302-4308, 2010.

[100] J. Gargiulo, S. Cerrota, E. Cortes, I.L. Violi, F.D. Stefani, "Connecting Metallic Nanoparticles by Optical Printing", Nano Letters, Vol. 16, pp. 1224-1229, 2016.

[101] L. Ling, H.L. Guo, X.L. Zhong, L. Huang, J.F. Li, L. Gan, Z.Y. Li, "Manipulation of gold nanorods with dual-optical tweezers for surface plasmon resonance control", Nanotechnology, Vol. 23, 215302, 2012.

[102] J. Do, M. Fedoruk, F. Jackel, J. Feldmann," Two-Color Laser Printing of Individual Gold Nanorods", Nano Letters, Vol. 13, pp. 4164-4168, 2013.

[103] M.A. Huergo, C.M. Maier, M. F. Castez, C. Vericat, S. Nedev, R. C. Salvarezza, A.S. Urban, J. Feldmann, "Optical Nanoparticle Sorting Elucidates Synthesis of PlasmonicNanotriangles", ACS Nano, Vol.10, Is. 3, pp. 3614–3621, 2016.

[104] J. Zhang, C. Xi, C. Feng, H. Xia, D. Wang, X. Tao, "High Yield Seedless Synthesis of High-Quality Gold Nanocrystals with Various Shapes", Langmuir, Vol. 30, pp. 2480−2489, 2014.

[105] S. Karim, M.E. Toimil-Molares, F. Maurer, G. Miehe, W. Ensinger, J. Liu, T.W. Cornelius, R. Neumann, "Synthesis of gold nanowires with controlled crystallographic characteristics", Applied Physics A, Vol. 84, Is. 4, pp. 403–407, 2006.

[106] L. Osinkina, T. Lohmüller, F. Jäckel, J. Feldmann, "Synthesis of Gold Nanostar Arrays as Reliable, Large-Scale, Homogeneous Substrates for Surface-Enhanced Raman Scattering Imaging and Spectroscopy", Journal of Physical Chemistry C, Vol. 117, Is. 43, pp. 22198–22202, 2013.

[107] T. Guo, P. Nikolav, A. Thess, D.T. Colbert, R.E. Smalley, "Catalytic growth of single-walled nanotubes by laser vaporization", Chemical Physics Letters, Vol. 243, pp. 49-54, 1995.

[108] A. Morales, C.M. Lieber, "A Laser Ablation Method for the Synthesis of Crystalline Semiconductor Nanowires", Science, Volume 279, pp. 208-211, 1998.

[109] H. Petrova, J. P. Juste, I. Pastoriza-Santos, G. V. Hartland, L. M. Liz-Marzán, P. Mulvaney, "On the temperature stability of gold nanorods: comparison between thermal and ultrafast laser-induced heating", Physical Chemistry Chemical Physics, Vol. 8, pp. 814–821, 2006.

[110] O Ekici, R K Harrison, N J Durr, D S Eversole, M Lee, A Ben-Yakar, "Thermal analysis of gold nanorods heated with femtosecond laser pulses", Journal of Physics D: Applied Physics, Vol. 41, 185501, 2008.

[111] A. B. Taylor, A. M. Siddiquee, J. W. M. Chon, "Below Melting Point Photothermal Reshaping of Single Gold Nanorods Driven by Surface Diffusion", ACS Nano, Vol. 8, No.12, pp. 12071-12079, 2014.

[112] N. Sumimoto, K. Nakao, T. Yamamoto, K. Yasuda, S. Matsumura, Y. Niidome, "In situ observation of structural transformation of gold nanorods under pulsed laser irradiation in an HVEM", Microscopy, Vol. 63, No.4, pp. 261-268, 2014.

[113] S. Link, ZL.Wang, M.A. El-Sayed, "How does a gold nanorod melt?", Journal of Physical Chemistry B, Vol. 104, No. 33, pp. 7867-7870, 2000.

[114] Y. Horiguchi, K. Honda, Y. Kato, N. Nakashima, Y. Niidome, "Photothermal Reshaping of Gold Nanorods Depends on the Passivating Layers of the Nanorod Surfaces", Langmuir, Vol. 24, Is. 20, pp. 12026-12031, 2008.

[115] C.J. DeSantis, D. Huang, H. Zhang, N.J. Hogan, H. Zhao, Y.Zhang, A. Manjavacas, Y. Zhang, W.-S. Chang, P.Nordlander, S.Link, N. J. Halas, "Laser-Induced Spectral Hole-Burning through a Broadband Distribution of Au Nanorods", Journal of Physical Chemistry C, Vol. 120, Is. 37, pp. 20518–20524, 2016.

[116] M. Gordel, J. Olesiak-Banska, K. Matczyszyn, C. Nogues, M. Buckle, M. Samoca, "Post-synthesis reshaping of gold nanorods using a femtosecond laser", Physical Chemistry Chemical Physics, Vol. 16, pp.71-78, 2014.

[117] Y.T. Wang, S. Teitel, C. Dellago, "Effect of surface structure on shape transformations of gold nanorods", Journal of Computational and Theoretical Nanoscience, Vol. 4, No.2, pp. 282-290, 2007.

[118] A. Babynina, M. Fedoruk, P. Kühler, A. Meledin, M. Döblinger, T. Lohmüller, "Bending Gold Nanorods with Light", Nano Letters., Vol. 16, No. 10, pp. 6485–6490, 2016.

[119] R. Bukasov, J. S. Shumaker-Parry, "Highly Tunable Infrared Extinction Properties of Gold Nanocrescents", Nano Letters, Vol.7, No.5, pp. 1113-1118, 2007.

[120] H. Husu, J. Mäkitalo, J. Laukkanen, M. Kuittinen, M. Kauranen, "Particle plasmon resonances in L-shaped gold nanoparticles", Optics Express, Vol. 18, No. 16, pp. 16601-16606, 2010.

[121] M. A. Kats, P. Genevet, G. Aousta, N. Yu, R. Blanchard, F. Aieta, Z. Gaburro, F. Capasso, "Giant birefringence in optical antenna arrays with widely tailorable optical anisotropy", Proceedings of the National Academy of Sciences, Vol. 109, No. 31, pp. 12364-12368, 2012.

[122] S. Link, C. Burda, B. Nikoobakht, M.A. El-Sayed, "How long does it take to melt a gold nanorod? A femtosecond pump-probe absorption spectroscopic study", Chemical Physics Letters, Vol. 315, Is. 1-2, pp. 12-18. 1999.

[123] S. Link, C. Burda, B. Nikoobakht, M.A. El-Sayed, "Laser-induced shape changes of colloidal gold nanorods using femtosecond and nanosecond laser pulses", The Journal of Physical Chemistry B, Vol. 104, No. 26, pp. 6152-6163, 2000.

[124] Y.T. Wang , S. Teitel, C. Dellago, "Surface-driven bulk reorganization of gold nanorods", Nano Letters, Vol. 5, No. 11, pp. 2174-2178, 2005.

[125] J. R. Sambles, "An Electron Microscope Study of Evaporating Gold Particles: The Kelvin Equation for Liquid Gold and the Lowering of the Melting Point of Solid Gold Particles", Proceedings of the Royal Society A, Vol. 324, No.1558, 1971.

[126] Ph. Buffat and J-P.Borel, "Size effect on the melting temperature of gold particles", Physical Review A, Vol.13, No. 6, pp. 2287-2294, 1976.

[127] M. Manghi, X. Schlagberger, Y.-W. Kim, R. R. Netz, "Hydrodynamic effects in driven soft matter", Soft Matter, Vol. 2, pp. 653-668, 2006.

[128] S. Mazur and S. A. Allison, "Brownian Dynamics Simulation of DNA Fragments in Strong Electric Fields", Journal of Physical Chemistry B, Vol. 101, pp. 2244-2250, 1997.

[129] C. Elvingson, "Computer simulation of the structure of DNA molecules in an electric field", Biophysical Chemistry, Vol. 43, pp. 9-19, 1992.

[130] M.K. Gwinner, E. Koroknay, L. Fu, P. Patoka, W. Kandulski, M. Giersig, H. Giessen, "Periodic Large-Area Metallic Split-Ring Resonator Metamaterial Fabrication Based on Shadow Nanosphere Lithography", Small, Vol. 5, No. 3, pp. 400-406, 2009.

[131] M. Decker, M. W. Klein, M. Wegener, "Circular dichroism of planar chiral magnetic Metamaterials", Optics Letters, Vol. 32, No. 7, pp. 856- 858, 2007.

[132] A. E. Nikolaenko, F. De Angelis, S. A. Boden, N. Papasimakis, P. Ashburn, E. Di Fabrizio, N. I. Zheludev, "Carbon Nanotubes in a Photonic Metamaterial", Physical Review Letters, Vol. 104, 153902, 2010.

[133] O. M. Maragò, P. H. Jones , P. G. Gucciardi, G. Volpe, A. C. Ferrari, "Optical trapping and manipulation of nanostructures", Nature Nanotechnology, Vol. 8, pp. 807–819, 2013.

[134] K. C. Toussaint Jr., B. Roxworthy, H. Chen, A. M. Bhuiya, Q.Ding, "Plasmonic Nanoantennas: From Nanotweezers to Plasmonic Photography", Optics & Photonics News, pp. 26-31, June 2015.

[135] A.N. Grigorenko, N.W. Roberts, M.R. Dickinson, Y. Zhang, "Nanometric Optical Tweezers Based on Nanostructured Substrates", Nature Photonics, Vol. 2, pp. 365−370, 2008.

[136] K.-Y. Chen, A.-T.Lee, C.-C.Hung, J.-S.Huang, Y.-T.Yang, "Transport and Trapping in Two-Dimensional Nanoscale Plasmonic Optical Lattice", Nano Letters, Vol. 13, pp. 4118−4122, 2013.

[137] K. Wang, E. Schonbrun, P. Steinvurzel, K. B.Crozier, "Trapping and Rotating Nanoparticles Using a Plasmonic Nano-Tweezer with an Integrated Heat Sink", Nature Communications, Vol. 2, Article 469, 2011.

[138] M. Toshimitsu, Y. Matsumura, T. Shoji, N. Kitamura, M. Takase, K. Murakoshi, H. Yamauchi, S. Ito, H. Miyasaka, A. Nobuhiro, Y. Mizumoto, H. Ishihara, and Y. Tsuboi, "Metallic-Nanostructure-Enhanced Optical Trapping of Flexible Polymer Chains in Aqueous Solution as Revealed by Confocal Fluorescence Microspectroscopy", Journal of Physical Chemistry C, Vol. 116, pp. 14610-14618, 2012.

[139] Y. Tanaka, S. Kaneda, K. Sasaki, "Nanostructured Potential of Optical Trapping Using a PlasmonicNanoblock Pair", Nano Letters, Vol. 13, pp. 2146−2150, 2013.

[140] Y. Pang, R. Gordon, "Optical Trapping of 12 Nm Dielectric Spheres Using Double-Nanoholes in a Gold Film", Nano Letters, Vol. 11, pp. 3763-3767, 2011.

[141] Y. Pang, R. Gordon, "Optical Trapping of a Single Protein", Nano Letters, Vol. 12, pp. 402−406, 2012.

[142] T. Shoji, J. Saitoh, N. Kitamura, F. Nagasawa, K. Murakoshi, H. Yamauchi, S. Ito, H. Miyasaka, H. Ishihara, Y. Tsuboi, "Permanent Fixing or Reversible Trapping and Release of DNA Micropatterns on a Gold Nanostructure Using Continuous-Wave or Femtosecond-Pulsed Near-Infrared Laser Light", Journal of American Chemical Society, Vol. 135, No. 17, pp. 6643-6648, 2013.

[143] F. Burmeister, C. Schäfle, T. Matthes, M. Böhmisch, J. Boneberg, P. Leiderer, "Colloid Monolayers as Versatile Lithographic Masks", Langmuir, Vol. 13, pp. 2983-298, 1997.

[144] R. D. Grober, R. J. Schoelkopf, D. E. Prober, "Optical antenna: Towards a unity efficiency near-field optical probe", Applied Physical Letters, Vol. 70, No. 11, pp. 1354-1356, 1997.

[145] P. Fromm, A. Sundaramurthy, P. J. Schuck, G. Kino, W. E. Moerner, "Gap-Dependent Optical Coupling of Single "Bowtie" Nanoantennas Resonant in the Visible", Nano Letters, Vol. 4, No. 5, pp. 957-961, 2004.

[146] P. J. Schuck, D. P. Fromm, A. Sundaramurthy, G. S. Kino, W. E. Moerner, "Improving the Mismatch between Light and Nanoscale Objects with Gold Bowtie Nanoantennas", Physical Review Letters, Vol. 94, 017402, 2005.

[147] U. Ch. Fischer and H. P. Zingsheim, "Submicroscopic pattern replication with visible light", Journal of Vacuum Science & Technology, Vol. 19, No.4, pp. 881-885, 1981.

[148] T. Lohmüller, L. Iversen, M. Schmidt, C. Rhodes, H.-L.Tu, W.-C.Lin, and J. T. Groves, "Single Molecule Tracking on Supported Membranes with Arrays of Optical Nanoantennas", Nano Letters, Vol. 12, No.3, pp. 1717-1721, 2012.

[149] J. C. Hulteen, R. P. Van Duyne, "Nanosphere lithography: A materials general fabrication process for periodic particle array surfaces", Journal of Vacuum Science and Technology A, Vol. 13, No. 3, pp. 1553-1558, 1995.

[150] W.-D. Ruan, Z.C. Lü, N. Ji, C.-X.Wang, B. Zhao, J-H. Zhang, "Facile Fabrication of Large Area Polystyrene Colloidal Crystal Monolayer via Surfactant-free Langmuir-Blodgett Technique", Chemical Research in Chinese Universities, Vol. 23, No. 6, pp. 712-714, 2007.

[151] A. V. Whitney, B. D. Myers, R. P. Van Duyne, "Sub-100 nm Triangular Nanopores Fabricated with the Reactive Ion Etching Variant of Nanosphere Lithography and Angle-Resolved Nanosphere Lithography", Nano Letters, Vol. 4, No. 8, pp. 1507-1511, 2004.

[152] B. K. Lee, K. S. Kim, J. H. Lee, N. H. Kim, Y. Roh, "Nanometer-scaled triangular platinum islands fabricated using the bridge phenomenon of polystyrene beads", Journal of Vacuum Science & Technology A, Vol. 26, No. 4, pp. 819-823, 2008.

[153] M. L. Juan, R. Gordon, Y. Pang, F. Eftekhari and R. Quidant, "Self-induced back-action optical trapping of dielectric nanoparticles", Nature Physics, Vol. 5, pp. 915-919, 2009.

[154] X. Huang, C. Tan, Z. Yin, H. Zhang, "25th Anniversary Article: Hybrid Nanostructures Based on Two-Dimensional Nanomaterials", Advanced Materials, Vol. 26, pp. 2185–2204, 2014.

[155] R. Costi, A. E. Saunders, U. Banin, "Colloidal Hybrid Nanostructures: A New Type of Functional Materials", Angewandte Chemie International Edition, Vol. 49, pp. 4878–4897, 2010.

[156] C. M. Galloway, M. P. Kreuzer, S. S. Aćimović, G. Volpe, M. Correia, S. B. Petersen, M. T. Neves-Petersen, R. Quidant, "Plasmon-Assisted Delivery of Single Nano-Objects in an Optical Hot Spot", Nano Letters, Vol. 13, No. 9, pp. 4299-4304, 2013.

[157] G. Baffou, P. Berto, E. B. Urena, R. Quidant, S. Monneret, J. Polleux, H. Rigneault, "Photoinduced Heating of Nanoparticle Arrays", ACS Nano, Vol. 7, No. 8, pp. 6478–6488, 2013.

[158] G. Baffou, J. Polleux, H. Rigneault, S. Monneret, "Super-Heating and Micro-Bubble Generation around Plasmonic Nanoparticles under CW Illumination", The Journal of Physical Chemistry C, Vol. 118, No. 9, pp. 4890–4898, 2014.

Acknowledgments.

Here I would like to say grateful words to the people who made this thesis possible.

I want to thank *Professor Dr. Jochen Feldmann*, my doctoral father who gave me the chance to be a part of his great group. I appreciate all scientific discussions, challenges, high requirements and standards of Professor Feldmann, which indeed helped me to grow as an independent researcher and to perform at the highest level. I am grateful for experience and knowledge in which I was able to collect and obtain in PhOG.

I am grateful to *Dr. Theobald Lohmüller* for all time we invested together in this thesis. I benefitted a lot from all discussions of the results and current status of my research. His optimism and energy helped me a lot during my PhD. I appreciate his support and the tips, which I will remember by heart.

I want to thank *Dr. Jessica Rodríguez-Fernández* for the interest in my research and discussions about crystallography and plasmonics of bent gold nanorods.

I appreciate the contribution of *Dr. Alexander Urban*, who was open for any discussions at all times and was ready to provide useful information, to share his knowledge. It was really great to do teaching of Advanced Solid States Physics together.

I am grateful to the SFB1032 project, which funded my work during my PhD studies.

Gerlinde Adam, Stefan Niedermaier, Katja Lyons, Martin Vogel Anna Helfrich, thank you for the great administrative and technical support. I want to thank my office mates Dr. Michael Fedoruk, Dr.Haojin Ba, Dr. Felix Deschler, Dr. Wei Li, Dr. Miao Li, Jasmina Sichert, Christoph Maier, Yu Tong for discussions about science and life, for great jokes and support. I want to thank Dr. Michael Fedoruk, Dr. Jaekwon Do, Dr. Paul Kühler, Dr. Silke Kirchner, Dr. Lydia Osinkina, Dr. Spas Nedev, and Verena Baumann for accepting me in the group and for making my arrival as easy as possible! Dr. Nicolas Bouchonville, Dr. Michael Carlson, Dr. Sol Carretero Palacios, Dr. Aliaksei Dubavik, are thanked for various activities together, which made this group entirely different compared to the others.

I want to thank Christoph Maier, Carla Pernpeintner, Patrick Urban and Dr. Theobald Lohmüller for investing their time in order to correct and proof reading this thesis.

Besides, I want to thank my friends Dr. Maria Lukatskaya (USA), Dr. Andrew Akbashev (USA), Dr. Olga Maslova (France), Dr. Elizabeth Pustovgar (Swiss), Dr. Eugene Smirnov (Swiss), Alexey Kurlov (Swiss), Artyom Chizhov (Russia), Anastasia Irkhina (Berlin), Ksenia Bittner (Munich) for their amazing and deep scientific discussions as well as their support. Many thanks go to my german teacher Dr. Katja El-Bouz, I can barely imagine

that I could survive without our german lessons. My friends: Olga Kachalova, Kateryna Stadnychenko, Denis Chirkov, Eugene Dulko, Eugeniya Dudko and Mikhail Voroniouk for all great time we had together and all discoveries. Mikhail Voroniouk especially is thanked for proof reading this thesis and for constructive comments. I want to thank Nicolas Hemmerle and Sebastian Fischer for their philosophic conversation and cherishing me during hard times. I can't believe that I met many great friends in Munich!

The last, but not the least, I am grateful to my family. My mom is the person who believes in me every second and never has any doubts about my success. One day I wish to become a person, like she is. I want to say thank you to my grandmother for her wisdom and math lessons during my high school time. My aunt Olga, my uncle Oleg, my god mother Galina, my cousins Daria, Anna and Dmitry, I am happy to grow up in such supportive family. I want to thank my grandfather, who unfortunately can't witness my defense, for all love he gave me.